2011-06-28

Devices and Methods for Electro-Physical Transport of DNA Across Cell Membranes

Quentin Theodore Aten
Brigham Young University - Provo

Devices and Methods for Electro-Physical Transport of DNA Across Cell Membranes

Quentin T. Aten

A dissertation submitted to the faculty of
Brigham Young University
in partial fulfillment of the requirements for the degree of

Doctor of Philosophy

Larry L. Howell, Chair
Brian D. Jensen
Sandra H. Burnett
Anton E. Bowden
David Kooyman

Department of Mechanical Engineering

Brigham Young University

August 2011

ABSTRACT

Devices and Methods for Electro-Physical Transport
of DNA Across Cell Membranes

Quentin T. Aten
Department of Mechanical Engineering, BYU
Doctor of Philosophy

A novel method for charged macromolecule delivery, called nanoinjection, has been developed at Brigham Young University. Nanoinjection combines micro-fabrication technology, mechanism design, and nano-scale electrical phenomenon to transport exogenous DNA across cell membranes on a nano-featured lance. DNA is electrically accumulated on the lance, precision movements of microelectromechanical systems (MEMS) physically insert the lance into cell, and DNA is electrically released from the lance into the cell. Penetration into the cell is achieved through a two-phase, self-reconfiguring metamorphic mechanism. The surface-micromachined, metamorphic nanoinjector mechanism elevates the lance above the fabrication substrate, then translates in-plane at a constant height as the lance penetrates the cell membranes. In-vitro studies indicate no statistical difference in viability between nanoinjected and untreated mouse zygotes. Pronuclear nanoinjection experiments on mouse zygotes, using microinjection as a control, demonstrate integration and expression of a nanoinjected transgene, and higher rates of zygote survival and pup births than the microinjection control.

A new compliant mechanism analysis method, the minimization of potential energy method (MinPE method) is presented to model the equilibrium position of compliant mechanisms with more degrees of freedom (DOF) than inputs, such as a fully-compliant nanoinjector. The MinPE method position and force predictions agree with the method of virtual work and non-linear finite element analyses of under-actuated and underconstrained compliant mechanisms. Additionally, a performance-based comparison is made between quadratic shell finite elements elements and 3-D quadratic solid elements for modeling geometrically non-linear spacial deflection of thin-film compliant mechanisms. The comparison's results suggest the more computationally efficient quadratic shell elements can be used to model spatially deforming thin-film compliant mechanisms.

Finally, this dissertation presents preliminary results for a proposed method of DNA transfer called cytoplasm-to-pronucleus nanoinjection. By placing a DNA coated lance into the cytoplasm of a mouse zygote and applying a voltage pulse of sufficient magnitude and duration, pores may open in the pronuclear membranes and DNA may be electrophoretically repelled from the lance. If effective, this process could result in transgenes without having to visualize and physically penetrate into the pronucleus. While embryo survival has been demonstrated under a variety of injection conditions, further study is needed to increase the process' consistency, and to determine if cytoplasm-to-pronucleus nanoinjection can generate transgenic animals.

Keywords: nanoinjection, MEMS, DNA, mice, transgenic, lance

ACKNOWLEDGMENTS

I would like to thank my wife, Kimberlee, for supporting me throughout my long educational journey. I would also like to thank Dr. Larry Howell, Dr. Brian Jensen, and Dr. Sandra Burnett for working with me over the course of many years to develop nanoinjection into a working protocol, and thank Dr. Anton Bowden and Dr. David Kooyman for their participation on my doctoral committee. I would also like to recognize Dr. Steven Benzley of the Brigham Young University Department of Civil Engineering for reviewing the finite element analyses presented in Chapter 5.

This work would not have been possible without the consistent assistance of undergraduate and graduate students in the Brigham Young University Department of Mechanical Engineering Compliant Mechanisms Research Laboratory and the Brigham Young University Department of Molecular & Microbiology MAFIA Research Laboratory. The generation of transgenic mice via nanoinjection was made possible by collaboration with Susan Tamowski and the technicians of the University of Utah Transgenic and Gene Targeting Mouse Core.

This work has been made possible through funding support provided by the Ira A. Fulton College of Engineering and Technology, the College of Life Sciences, Crocker Ventures, LLC and Nanoinjection Technologies, LLC. This material is based upon work supported in part by the National Science Foundation under Grants No. CMS-0428532 and No. CMMI-0800606. Any opinions, findings, and conclusions or recommendations expressed in this material are those of the author(s) and do not necessarily reflect the views of the National Science Foundation.

TABLE OF CONTENTS

LIST OF TABLES

LIST OF FIGURES

CHAPTER 1. INTRODUCTION

1.1 Hypothesis / Problem Statement

A novel method for charged macromolecule delivery, called nanoinjection, has been developed at Brigham Young University. Nanoinjection combines micro-fabrication technology, mechanism design, and nano-scale electrical phenomenon to transport exogenous DNA across cell membranes. In preliminary studies, prototype nanoinjectors cytoplasmically delivered reporter transgenes to mouse zygotes with high rates of survival and transgene expression [1]. These preliminary results suggested nanoinjection has the potential to transfer genetic material to the pronucleus of a mouse zygote, resulting in integration and expression of the injected gene. Formally stated, the hypothesis of this research is:

> *The localized electrical accumulation and release of DNA molecules by microelectromechanical systems (MEMS), coupled with precise mechanical penetration of cellular membranes by MEMS devices, can result in genomic integration of exogenous DNA.*

The research presented here aimed to develop nanoinjection devices and protocols to enable transgenic animal production. The goals of this research can be summarized by the following two aims:

1. Investigate the feasibility of transgenesis via pronuclear nanoinjection.
2. Explore the feasibility of transgenesis via pulsed, high-voltage, cytoplasmic nanoinjection.

This chapter provides background detailing the current state of the art in transgenic animal production and preliminary results from prototype nanoinjectors which motivated this research. The results of the research encompassed by the aims above are then summarized.

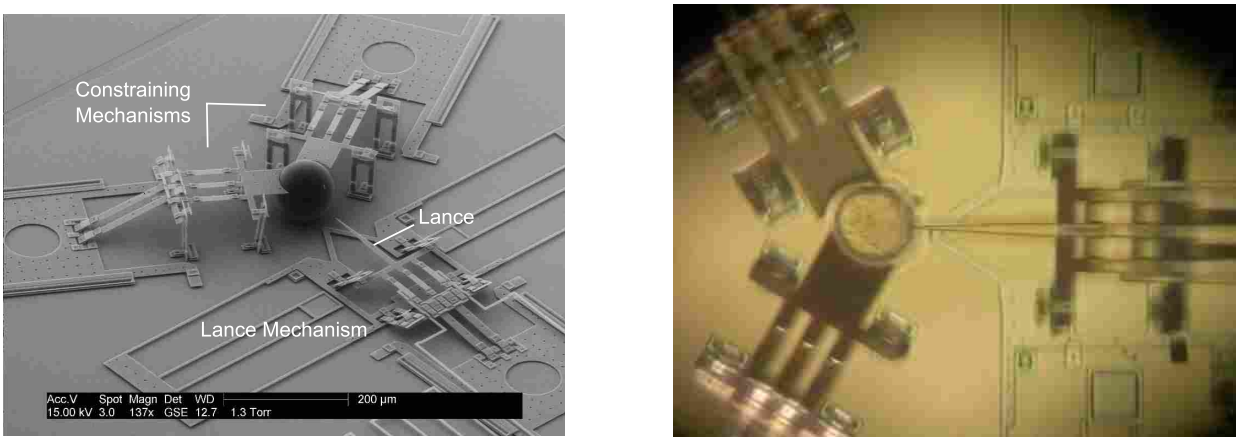

(a) (b)

Figure 1.1: (a) A labeled scanning electron microscope (SEM) image of the nanoinjector grasping a 100 μm diameter latex sphere. (b) An optical microscopy image of the nanoinjector injecting a mouse zygote.

1.2 Background

The nanoinjector is a MEMS device for transporting exogenous DNA across cell membranes by exploiting electrical accumulation and release of DNA by a nano-featured lance. In its current embodiment, the nanoinjector is designed to inject transgenes into mouse zygotes. Figure 1.1(a) shows a prototype nanoinjector performing a mock-nanoinjection on a 100 μm diameter latex sphere, and Figure 1.1(b) shows the nanoinjector during injection of a mouse zygote.

The nanoinjector is a partially compliant [2], metamorphic mechanism [3] fabricated using a standardized two-layer polycrystalline silicon process [4]. The lance mechanisms' principal components are shown in Figure 1.2. The nanoinjector lance mechanism consists of a parallel-guiding, change-point, six-bar mechanism attached to a compliant, parallel-guiding, folded-beam suspension. The six-bar mechanism's horizontal link, which includes the lance, is electrically connected to bond pads via highly folded compliant flexures. The restraint mechanisms, shown in Figures 1.1(a) and 1.2, are parallel-guiding, change-point, six-bar mechanisms kinematically grounded to the fabrication substrate, with cupped surfaces on their horizontal links for grasping zygotes. The restraint mechanisms included in these earlier prototypes are not developed further in this research.

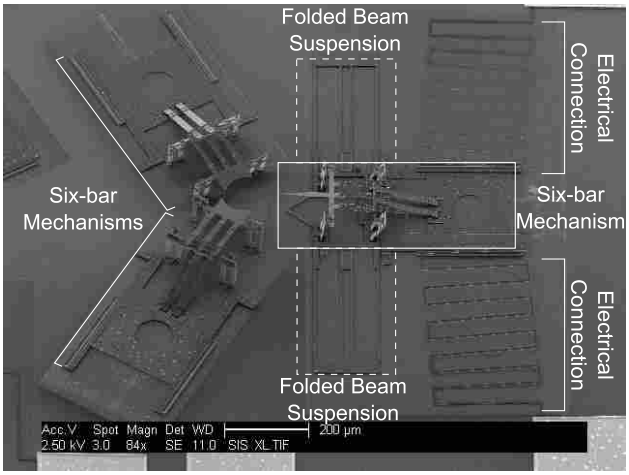

Figure 1.2: Labeled scanning electron micrograph of the nanoinjector lance mechanism and restraint mechanisms.

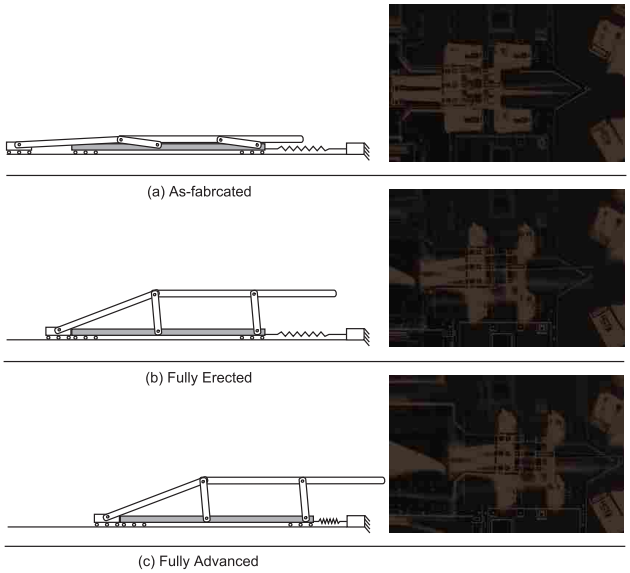

Figure 1.3: Metamorphic motion of the nanoinjector: (a) as-fabricated, (b) with the lance erected (c) linearly advanced toward the target cell.

The lance mechanism has a two-stage motion designed to minimize cell trauma during injection. The lance's six-bar mechanism is a rigid-link mechanism and has negligible stiffness relative to the compliant, folded-beam suspension. Beginning from the as-fabricated position (Figure 1.3a), advancing the lance's slider erects the six-bar mechanism to its full elevation, as shown in Figure 1.3b. Additional input displacement deflects the folded-beam suspension causing, the lance to translate toward the target cell at a constant elevation, as in Figure 1.3c. Through this mo-

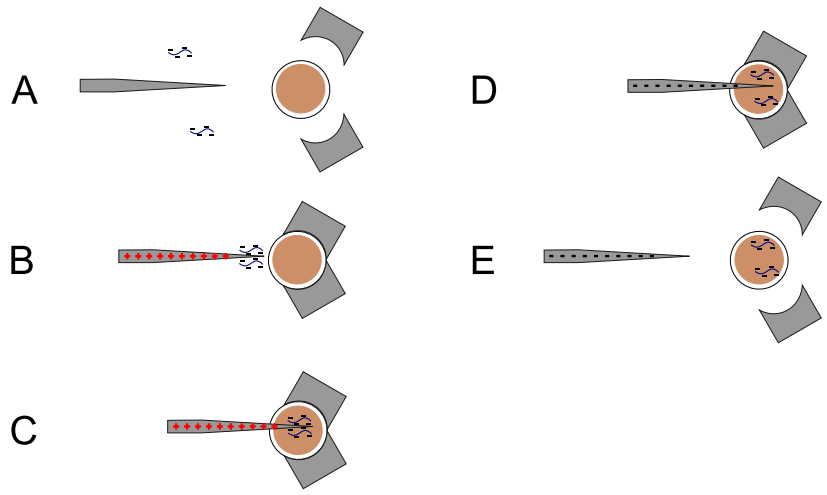

Figure 1.4: A process flow diagram for the nanoinjector: **(A)** embryo placement, **(B)** DNA attraction, **(C)** lance insertion, **(D)** DNA release, **(E)** embryo retrieval.

tion, the lance reaches its full elevation before contacting the cell, and pierces the cell membranes along a linear path.

The operation of the nanoinjector can be summarized by the five steps shown in Figure 1.4. **(A)** The nanoinjector is immersed in cell culture media, and a dilute DNA solution is placed over the nanoinjector. **(B)** The lance is connected to the positive terminal of a voltage source, which electrostatically accumulates DNA on the lance's surface. The target zygote is placed oriented in front of the nanoinjector. Though previous nanoinjector designs included MEMS cell restraint devices, a holding micropipette was used for all zygote positioning and restraint during the experiments reported in this dissertation. **(C)** The positively charged lance is actuated further, piercing the cellular membranes. **(D)** The polarity of the voltage source is reversed, negatively charging the lance, and releasing DNA from the lance's surface. **(E)** The lance mechanism is withdrawn, and the zygote is retrieved.

To give context for the nanoinjector, this section provides summaries of transgenic animals in science and medicine, biological applications of MEMS devices, molecular mechanisms of DNA integration and their engineering implications, current methods of transgene delivery, and preliminary results indicating the nanoinjector has the potential to generate transgenic animals.

1.2.1 Transgenic Animals in Science and Medicine

Transgenic animals, animals that carry foreign or modified genetic material, have greatly contributed to the understanding of the genetic underpinnings of development, normal biological processes, and disease processes. Transgenic animals were first generated thirty years ago [5]–[7] and have since played critical roles in studying such diverse topics as cancer [8]–[13], reproduction [14], [15], immunology [16]–[19], neurological functions [20], and Alzheimer's disease [21]. To give a perspective on the scope and impact of transgenic animal research, a current search of the National Institutes of Health PubMed database for "transgenic" animals returns over 79,000 articles written within the last 30 years, with nearly 5,000 in the last year alone.

1.2.2 Biological Applications of MEMS Devices

At nearly the same time that transgenic animals were first developed, advances in semiconductor fabrication processes enabled the production of micro-scale devices with both electrical and mechanical elements [22]. These microelectromechanical systems (MEMS) have been developed into switches [23], sensors [24], actuators [23], complex micro-mechanisms [25], and are now common place in consumer electronics. More recently, researchers have begun to develop MEMS devices for performing biological experiments and even directly manipulating cells (bio-MEMS). For example, chip-level systems have been developed to perform DNA manipulation protocols typically carried out using macro-scale equipment [26], such as electrophoresis [27], polymerase chain reaction (PCR) replication of DNA samples [28], and DNA purification [29]. Various MEMS devices have been developed for grasping cells [30]–[36], dissecting cells [37], injecting DNA into cells [38]–[43], providing force measurement [36] or force-feedback [44] during DNA injection into cells. A combined DNA manipulation, cell restraint and DNA injection bio-MEMS technology would enable low-cost, chip-level transgenic animal production.

1.2.3 Molecular Mechanisms of DNA Integration and their Engineering Implications

Any system, bio-MEMS or otherwise, designed to generate transgenic organisms relies on cellular processes to integrate foreign DNA into the target cell's genome. This dependence on

natural cellular processes has engineering design and device protocol implications for the proposed nanoinjector system.

Studies of the junctions between genomic mouse DNA and a blunt-ended transgene have revealed short homologies[1] (1-3 nucleotides), and that the transgene inserted near Topoisomerase I consensus sites. Topoisomerases are DNA unwinding proteins active during DNA replication. Coupled with studies on Topoisomease II, these suggest that Topoisomerase I and Topoisomerase II may play a critical role in inserting blunt ended transgenes into mammalian chromosomes. [45], [46]

In similar studies of insertions of a transgene with protruding single strands (PSS) at both the 5' and 3' ends, the transgene was observed to integrate with the 3' PSS intact at chromosome-transgene junctions, and both the 5' and 3' PSS intact at transgene-transgene concatemer[2] junctions. These results are not consistent with the activity of Topoisomerase, which ligates blunt-ended strands, and suggest other DNA repair mechanisms are involved in the integration of transgenes with PSS ends. Specifically, the 3' -OH terminus of a PSS transgene may serve as a priming location for a repair mechanism. [46], [47]

When taken together, these results propose an insertion model based on single and double stranded chromosomal breaks and repair mechanisms. Topoisomerase I and II induced breaks, as well as breaks induced by UV damage, endonucleases, and other sources of DNA damage may serve as locations for transgene integration. In summary, exogenous DNA in the vicinity of a break (or recruited to the break by repair proteins) is integrated into the chromosome by the cellular repair mechanisms [46], [48].

The developmental stage at which the transgene is present in the target cell also plays a critical role in successful transgene integration. A study on microinjection of a transgene into developmentally synchronized animal cells in culture demonstrated that the optimal period in cell cycle for integration of the transgene is between the Gap-1 / Synthesis phase boundary through early Synthesis phase [49]. This result agrees well with the theory that naturally occurring Topoisomerase I and II induced breaks (which are generated during DNA synthesis) are sites for transgene integration. Though the repair mechanism theory of transgene integration would allow integra-

[1] Short sequences of identical base pairs in the transgene insert, and the genomic DNA.

[2] Concatemers are head-to-tail repeats of transgenes

tion of the transgene at any point in the cell cycle, to generate a fully transgenic organism from a zygote, the integration must occur before the first DNA replication is complete [50]. In mouse transgenesis, this optimal window for integration occurs some time between 22-24 hours post hCG injection[3] [51].

All of these proposed transgene integration mechanisms require the intimate proximity of the transgene and the chromosomal DNA. To generate a transgenic animal, the transgene must then be present in at least one of the target zygote's two pronuclei prior to the first round of DNA replication being complete [50], [52]. Also, since all of these processes are essentially random in their frequency, a large number of transgene copies (several hundred) increases the likelihood of integration [52], though too many copies can result in cell death [52] or transgene silencing [53].

From an engineering standpoint, the molecular mechanisms of transgene integration have three major design implications for proposed transgene delivery systems. First, the delivery system must be capable of delivering the transgene to the nucleus (or pronucleus) of the target cell. Second, the system must deliver an adequate, but not excessive number of transgene copies. Third, the transgene delivery system must complete an adequate number of transgene deliveries within the optimal time window for transgene integration ($\approx$4 hours for mouse zygotes); meaning the system must have high throughput, high delivery success rates, or preferably both.

1.2.4 Current Methods of Transgene Delivery: Operating Principles, Advantages, and Limitations

Given the three broad requirements listed above, multiple methods have been developed for transgene delivery. Some of these methods are well suited to transgenic animal production, while others are more applicable to transfection of culture cells. This summary focuses on those methods which are most frequently used in animal transgenesis: pronuclear microinjection, electroporation and blastocyst fusion of ES cells, and intracytoplasmic sperm injection. Several other gene transfer methods are also mentioned which are infrequently or never applied to transgenic animal production.

[3] hCG: Human Chorionic Gonadotropin, a hormone used to stimulate mouse ovulation

Microinjection

Microinjection, in the broadest of terms, is a process by which a substance suspended in a liquid, DNA in this case, is introduced into living cells by mechanically puncturing the cell's membrane(s) and then depositing the substance within the cell. Since the first microinjector was described in the literature sixty years ago [54]–[56], the prevailing microinjector design has consisted of a movable, fluid-filled, hollow needle whose contents are expelled by an accurate, macro-scale pump [57], [58]. Refinements to this general concept have included the production of smaller more consistent needles [38], [59], robotic manipulators [35], force-feedback controls [44], and fully automated injection systems [39].

To generate a transgenic animal using microinjection, a precisely measured volume of solution containing the transgene is microinjected into a zygote's pronucleus [57]. Pronuclear microinjection of mouse zygotes was first performed 30 years ago [5], [6], [60] and developed into a repeatable process within a few years [52]. Pronuclear microinjection has also been applied to other species including zebra fish [11], [61], pigs [62] and goats [63] to name a few. By injecting a known volume of transgene solution into the pronucleus, microinjection has the advantage of guaranteeing the transgene copies will be in close proximity to the target cell's chromosomes. Attempts to cytoplasmically inject transgenes into mouse zygotes result in low integration rates [52].

Microinjection has some intrinsic limitations arising from the need to target the pronucleus and from the injection of liquids into the pronucleus. The three-dimensional physical manipulations required to perform pronuclear microinjection necessitate that either a highly skilled, highly trained technician perform the microinjection [57], or that the manipulations be performed by automated systems [38], [39]. Even when microinjection is performed by adequately trained technicians, the process significantly reduces the viability of delicate cell types. For example, pronuclear microinjection of mouse zygotes typically results in a 20–30% reduction in the number of embryos which complete the first mitotic division [52], [57], [64]. With optimized protocols, the transgene expression rates among the surviving embryos is approximately 40% [64], [65] , and overall rate of transgenesis (defined as the percent of injected embryos developing into transgenic pups) is between 1–6% [5], [52], [57]. Research has recently indicated that the physical process of injecting extracellular fluid into mouse embryos causes chromosomal breakages which in turn cause decreased embryo viability [66].

More advanced microinjection systems increase the throughput of microinjection [35], [38], [44] but give essentially the same outcomes as microinjections performed 30 years ago. The relatively constant rate of transgenesis suggest the impact of any improvements to injection systems based on the needle-and-pump design paradigm will be limited to further increases in the speed and ease of microinjection.

Intracytoplasmic Sperm Injection

Intracytoplasmic sperm injection ICSI is performed in two main steps. First spermatozoa harvested from donor males are incubated in a solution containing the transgene. Second, the sperm and the DNA solution are co-injected (simultaneously microinjected) into oocytes harvested from donor females. With the transgene intimately associated with the sperm head, the transgene will likely be present in the male pronucleus during DNA replication, resulting in integration of the transgene. [67]

The transgene can become associated with the sperm either by incubating the sperm in a solution containing the DNA at room temperature [68], or by augmenting the uptake of exogenous DNA by chemical treatments [69], or through ultrasonic degradation of the sperm membranes [70]. Though high success rates have been reported ([68] for example), a direct comparison of ICSI with pronuclear microinjection resulted in nearly the same overall success rates for both methods ($\approx$1-3%) [71].

Because the physical manipulations involved in ICSI are essentially the same as those required in pronuclear microinjection, ICSI shares many of the advantages and challenges with pronuclear microinjection. ICSI does pose the additional challenge of associating the transgene with the spermatozoa prior to injection.

Electroporation of Embryonic Stem Cells

The process of electroporation exploits two nano-scale phenomenon: first, the motion of charged particles in an electric field, and second, the formation of cellular and nuclear membrane pores in cells exposed to high electric fields [72], [73]. The electrophoretic motion of DNA through the micropores in the target cells' cellular and nuclear membranes bring the transgene into prox-

imity of the genomic DNA. In addition to electroporation of culture cells, whole embryos can be electroporated, though this results in integration in only a portion of the embryo [74]. Post electroporation survival of zygotes [75] and ooctyes [76] has been demonstrated, and successful cytoplasmic delivery of dsRNA [76] and other molecules [77] has been reported. However, integration of a transgene in an electroporated zygote has not been reported.

To generate a transgenic animal via electroporation, an indirect approach is applied. First, embryonic stem cells (ES cells) are transfected by electroporation. Second, the ES cells expressing the transgene are selectively isolated. Third, the transfected ES cells are cultured. Fourth, the transfected ES cells are fused with a non-transgenic blastocyst, typically through microinjection of the ES cells into the blastopore. The transgenic ES cells then make up only a portion of the cells within the blastocyst, resulting in chimeric offspring. Fifth, a breeding program is instituted to produce fully transgenic individuals from chimeric founders. [51], [78]–[81]

The principal advantage of this indirect approach to transgenic animal production is the assurance that blastocysts fused with transgenic ES cells have a portion of their cells carrying the transgene. Also, because only a portion of the blastocysts' cells carry the transgene, this method is well suited to the study of embryo lethal genetic modifications [78]. This indirect approach, however, has some limitations and difficulties. Electroporation and transfer of ES cells is limited to generating chimeras; meaning the process of electroporation in general is currently limited to full transgenesis via breeding chimeras. This indirect method is also labor intensive when compared to microinjection. ES cell electroporation, selection, and culture, are non-trivial and the generation of transgenic animals from ES cells relies on microinjection to fuse ES cells with a blastocyst.

Other Methods of Gene Transfer

Scientists have developed many more gene transfer methods in addition to the three principal methods discussed above. [69] and especially [78] provide excellent summaries of other methods applied to transgenic animal production, including viral mediated transfection, chemical transfection of ES cells, and nuclear transfer. These methods, though feasible, are not often employed in current transgenic animal production.

Of particular interest to the development of the nanoinjector is a class of DNA transport systems or devices which can be classified as nano-featured, non-fluidic, mechanical DNA deliv-

ery systems. One approach has been to fire DNA coated nano-scale projectiles into a cell using a "gun" [82] or magnetic fields [83]. Others have developed nano-scale, solid needle DNA injection systems for somatic cells which either puncture the cell's membranes allowing DNA to enter by diffusion [84], or incubate a nano-needle in the target cell for several minutes to allow release of chemically bound DNA [40], [85]. Multiple somatic cells can be injected by arrays of nano-scale needles in "impalefection;" however, this requires the impaled cells to grow around the needles [42], [43]. Though each of these systems were demonstrated in somatic culture cells, none of these systems are currently applicable to zygotes, or have been demonstrated in ES cell lines.

1.2.5 Preliminary Results from Nanoinjector Testing

For the nanoinjector to generate transgenic animals, it must accomplish the same basic tasks as the other DNA delivery methods described above. Namely, the nanoinjector must deliver an appropriate number of transgene copies to the interior of one of the zygote's pronuclei without causing lethal trauma to the zygote. Nanoinjections were performed according to the process outlined in Figure 1.4, with a holding pipette restraining the zygotes. Preliminary experimental results demonstrate that the nanoinjector lance can electrostatically accumulate and release DNA, nanoinjection does not significantly decrease zygote viability, and DNA released from the nanoinjector is expressed in developing embryos. However, the expression of the transgene in blastocysts does not conclusively demonstrate transgene integration. These preliminary results provide strong evidence that nanoinjection can be an efficient means of transgenic animal production.

The Nanoinjector Lance can Electrostatically Accumulate and Release DNA

The accumulation and release of DNA by the nanoinjector lance has been visualized using fluorescence microscopy of DAPI[4] stained DNA. A positive voltage (1.5 V) was applied to the lance, and DNA was observed to accumulate on the lance's surface. When the lance's polarity was reversed, DNA was observed to be released from the lance's surface.

Raw images of the DAPI stained DNA were post-processed using a custom algorithm as described in [1] to generate concentration maps, as shown in Figure 1.5, and to generate estimates

[4] 4',6-diamidino-2-phenylidole dihydrochloride

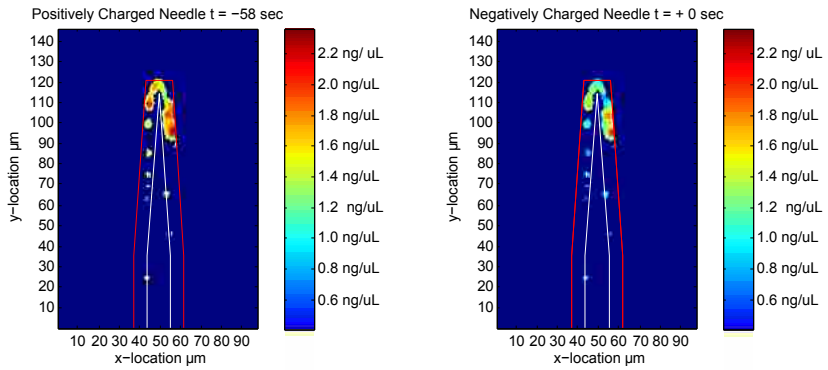

Figure 1.5: Fluorescence microscopy concentration maps of a nanoinjector lance showing only the DAPI stained DNA closely associated with the lance after DNA accumulation, and during DNA release. A comparison of the images graphically shows where the DNA was repelled from the surface of the lance. NOTE: Images best viewed in color.

of the number of DNA particles accumulated then released from the lance. The first concentration map in Figure 1.5 shows the regions of concentrated DNA surrounding the lance after accumulation (and 58 seconds prior to DNA release). An estimated 35,000 DNA molecules (4.7KB plasmid) are associated with the lance in this image. The second concentration map shows a measurable drop in DNA concentration surrounding the lance during DNA release. In this image, approximately 6000 DNA molecules were released from the lance in six seconds. More thorough descriptions of the DNA accumulation and release experiments can be found in [1], [41].

Initially, the DNA was assumed to move simply as a charged particle in the electric field generated by the lance [41], [86]. This assumption suggested that DNA could be attracted from relatively large distances (tens of microns), then quickly dispersed over equally large distances, even with relatively low applied voltages. However, the effect of electrolytic current flow within ionic solutions has been shown to be the dominant effect through model refinements and macro-scale electrophoresis experiments [87]. Taking electrolytic flow into account, large scale DNA motion will not occur at the lance at the current operating voltage (1.5 V), though motion within a sub-micron boundary around the lance is still possible [88], [89]. Thus, DNA coming into contact with a positively charged lance at 1.5 V will accumulate on the lance, and DNA accumulated on the lance will be released by -1.5 V but not vigorously repelled. Electrophoretic motion of DNA

to and from the lance is possible only if the voltages applied to the lance exceed a threshold known as the decomposition voltage [89].

Nanoinjection Does not Significantly Decrease Zygote Viability

Nanoinjected cells survive and develop to the 2-cell and blastocyst stages at rates comparable to untreated cells. Table 1.1 gives a comparison of survival rates of untreated and nanoinjected zygotes. The 2-cell survival rates were calculated from 7 experimental replicates totaling 229 untreated zygotes and 244 nanoinjected zygotes. The blastocyst survival was computed from 6 experimental replicates, totaling 99 untreated embryos and 168 nanoinjected embryos. There is no statistical difference between the survival to the 2-cell stage (p-value = 0.89) or to the blastocyst stage (p-value = 0.85). The large error bound on the blastocyst development rates in the untreated group in Table 1.1 suggest inconsistent culture technique, and further data is required to accurately establish the blastocyst development rates of untreated and nanoinjected zygotes.

DNA released from the nanoinjector is expressed in developing embryos

In-vitro culture of cytoplasmicly nanoinjected mouse embryos demonstrate DNA can be moved across cell membranes using the nanoinjector. Expression of reporter transgenes (dsRed-1, dsRed-monomer) encoding red fluorescent protein (RFP) has been observed in 2-cell through blastocyst stage embryos. Table 1.2 gives the transgene expression rate for 111 nanoinjected zygotes (7 experimental replicates) expressing RFP at any stage in development. A fluorescent microscopy image of nanoinjected blastocysts expressing dsRed-monomer is shown in Figure 1.6. These preliminary studies confirm that nanoinjection successfully moves DNA across membranes and may

Table 1.1: 2-cell and blastocyst development rates for untreated and nanoinjected mouse zygotes. There is no statistical difference between the survival to the 2-cell stage (p-value = 0.89) or to the blastocyst stage (p-value = 0.85).

	2-Cell (%)	**Blastocyst (%)**
Untreated	60.3 ± 34.2	14.4 ± 23.35
Nanoinjected	58.3 ± 16.71	12.3 ± 11.92

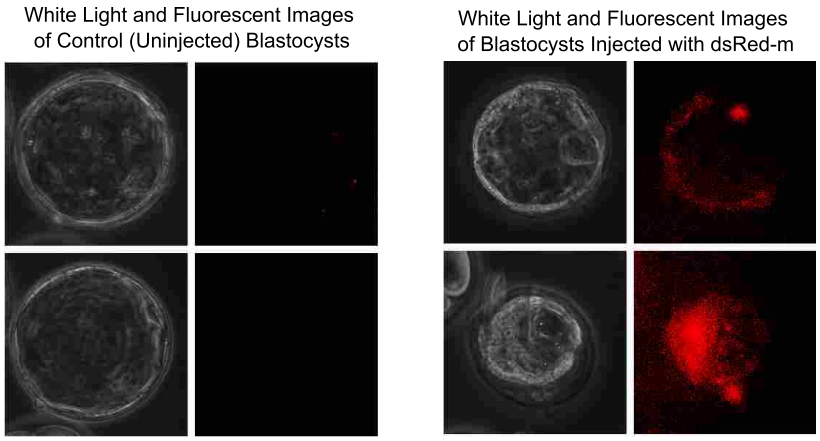

Figure 1.6: Nanoinjected blastocysts expressing RFP either fully (lower right) or chimerically (upper right); compare to the lack of expression in control blastocysts (left).

not interrupt embryonic development. However, it is quite possible that the expression observed in these embryonic cells is only cytoplasmic.

1.3 Research Summary

In light of molecular mechanisms of DNA integration and the physics governing electrophoretic motion of DNA, this research took two approaches to achieving transgenesis via nanoinjection given in the aims:

1. Investigate the feasibility of transgenesis via pronuclear nanoinjection.

2. Explore the feasibility of transgenesis via pulsed, high-voltage, cytoplasmic nanoinjection.

The results of the research and the contents of this dissertation are succinctly described by decomposing these aims into research tasks.

Table 1.2: Expression rates for embryos developing from nanoinjected embryos.

Developmental Stage	**Expression Rate**
All Stages	62.4% +/- 15.3%

1.3.1 Aim 1: Investigate the Feasibility of Transgenesis via Pronuclear Nanoinjection

Task 1: Refine the Nanoinjector Mechanism's Design

Chapter 2 describes the mechanical design and testing of the partially compliant nanoinjector mechanism. Included in this testing are 24-hour (two-cell stage) viability results for nearly 3,000 nanoinjected mouse zygotes. The rate of development to the two-cell stage was similar for nanoinjected and un-manipulated mouse zygotes.

Task 2: Investigate Production of Transgenic Mice via Pronuclear Nanoinjection

The nanoinjector mechanisms described in Chapter 2 were used to perform pronuclear nanoinjection of fluorescent reporter genes into mouse zygotes. Chapter 3 describes the protocols for pronuclear nanoinjection which resulted in successful integration and expression of a fluorescent reporter gene in mouse pups. The nanoinjected embryos were observed to have higher in-vitro and gestational viability when compared to microinjected embryos. The the rate of transgene integration and expression was very similar for pups born from nanoinjected embryos and pups born from microinjected embryos. Detailed materials and methods, and expanded results tables and figures from these experiments are given in Appendix A.

Task3: Develop Analytical Tools for the Design of a Fully Compliant Nanoinjector

During nanoinjection experiments, it was observed that the quality of the nanoinjector's motion has a strong influence on the rate of embryo survival. A fully-compliant nanoinjector could further improve the precision of the nanoinjector's motion. To this end, compliant mechanism modeling methodologies were developed to facilitate the design of future fully-compliant nanoinjector prototypes.

Chapter 4 describes an energy-based method (the minimization of potential energy method) for the analysis of underconstrained and underactuated compliant mechanisms. This chapter has been accepted for publication in the ASME *Journal of Mechanical Design*.

Chapter 5 gives a performance-based comparison of finite element models of solid and shell elements for the modeling of thin-film, compliant MEMS devices. Chapter 5 concludes

with a finite element analysis of a prototype fully-compliant nanoinjector. This chapter has been accepted for publication as in the *Journal of Finite Elements in Analysis and Design*. Appendix B gives example ANSYS scripts from the analyses described in Chapter 5.

1.3.2 Aim 2: Explore the Feasibility of Transgenesis via Pulsed, High-voltage, Cytoplasmic Nanoinjection

Explore Voltage Pulse Magnitudes and Durations which Allow for Embryo Development

Models of eletrophoretic motion and the phenomenon of electroporation suggest cytoplasmic nanoinjection may be possible using a high-voltage electrical pulse to cause localized electroporation of the pronucleus and repel DNA into the pronucleus. Chapter 6 describes the theory and literature which motivate this approach. Two-cell stage and gestational viability results are presented for the preliminary cytoplasmic nanoinjection protocols tested thus far. Though no transgene expression has been observed in embryos following high-voltage, cytoplasmic nanoinjection, the viability results suggest that process parameters may be found which allow for acceptable rates of embryonic development. Chapter 6 also gives recommendations to improve high-voltage, cytoplasmic nanoinjection. This chapter was submitted as a status report to Nanoinjection Technologies LLC.

CHAPTER 2. A SELF-RECONFIGURING METAMORPHIC NANOINJECTOR FOR INJECTION INTO MOUSE ZYGOTES

This chapter discusses the design and mechanical testing of a surface-micromachined microelectromechanical system (MEMS) nanoinjector designed to inject DNA into mouse zygotes which are ≈ 90 μm in diameter. The proposed injection method requires that an electrically charged, DNA coated lance be inserted into the mouse zygote. Penetration into the mouse zygote without tearing the cell membranes is achieved through a two-phase, self-reconfiguring metamorphic mechanism. In the first motion subphase a change-point six-bar mechanism elevates the lance to ≈ 45 μm above the substrate. In the second motion subphase, a compliant folded-beam suspension allows the lance to translate in-plane at a constant height as it penetrates the cell membranes. Viability studies of nearly 3000 nanoinjections resulted in 71.9% of nanoinjected zygotes progressing to the two-cell stage.[1]

2.1 Introduction

The nanoinjector, shown in Figure 2.1, is a surface-micromachined microelectromechanical system (MEMS) for electro-physical injection of DNA into mouse zygotes. Insertion of foreign genetic material into the genome of mice and other mammals is a critical step in understanding and utilizing genes' functions. Genetically modified (transgenic) animals are currently used in research into such varied topics as cancer [90], [91], Alzheimer's disease [21], [92], and diabetes [93]. To genetically modify every cell within an animal, the genetic construct of interest (transgene) must be present within at least one pronucleus (the membrane surrounding each set of parental chromosomes) before the zygote's first division [49], [50]. In a mechanical sense, direct transgene delivery to a zygote requires precise motion across tens of micrometers as the means of gene delivery penetrates into the pronucleus.

[1]This chapter was originally prepared as a journal article with Sandra Burnett, Brian Jensen, and Larry Howell contributing as co-authors.

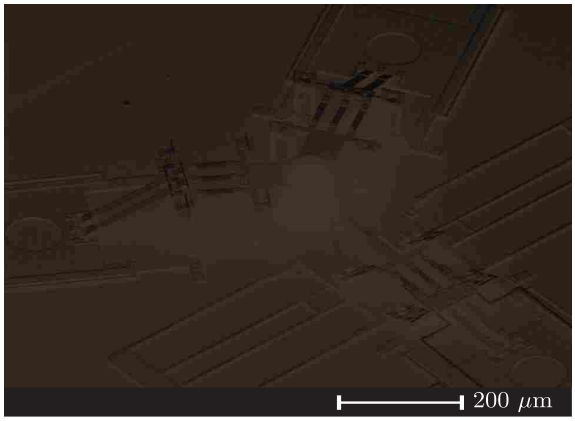

(a) SEM of a nanoinjector

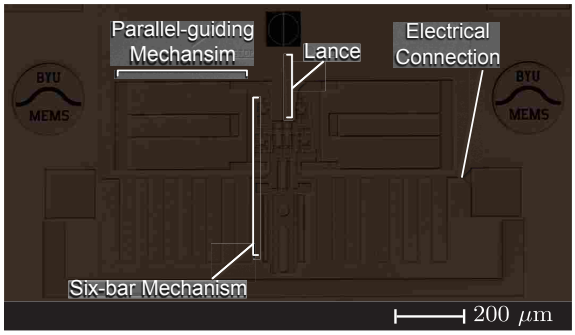

(b) SEM of a nanoinjector

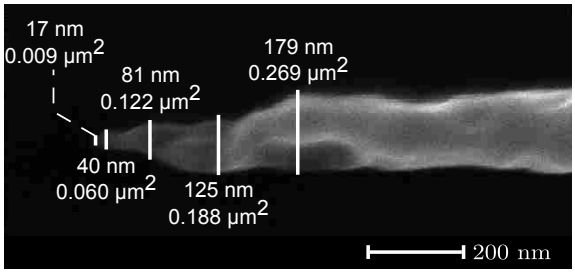

(c) SEM of the lance tip

Figure 2.1: Labeled scanning electron microscope (SEM) images of (a) the metamorphic nanoinjector posed as if it were injecting a 100 μm latex sphere, (b) the metamorphic nanoinjector in its as-fabricated position, and (c) the tip of the nanoinjector lance. The two six-bar mechanisms restraining the latex sphere in (a) are not described in this paper.

MEMS devices, such as the nanoinjector, are potentially well suited to introduce genetic material into developing embryos because of their relatively small scale, potential for complex motion, and their ability to mechanically and electrically interact with individual cells [94]–[96]. Additionally, MEMS fabrication techniques allow for features within a single device be as small as tens of nanometers, or as large as hundreds of micrometers. For example, the tip of the nanoinjector

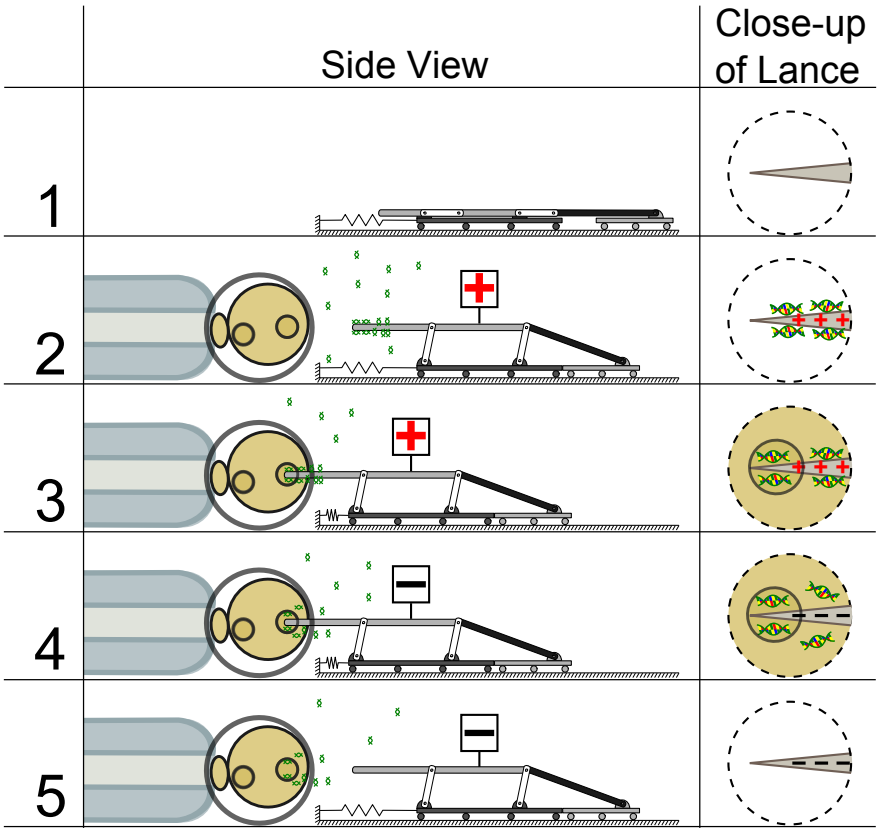

Figure 2.2: Schematic representation of nanoinjection of DNA into a mouse zygote. All nanoinjections occur with the nanoinjector submerged in a pH buffered saline solution. Step 1 nanoinjector is in its as-fabricated position. Step 2 the lance is elevated and a positive charge is applied, accumulating DNA on the lance's tip. Step 3, the lance moves at a constant height, penetrating into the target zygote. Step 4, the charge on the lance is reversed, releasing DNA into the zygote. Step 5, the lance moves at a constant elevation out of the zygote.

lance in Figure 2.1(c) has a minimum in-plane width of only 17 nm, while the mechanism's overall dimensions are four orders of magnitude larger, as seen in Figure 2.1(b).

The nanoinjector applies nanometer-scale features, precise mechanical motion over tens of microns, and electrical manipulation of DNA in an electro-physical method of gene transfer called nanoinjection. Figure 2.2 graphically outlines the nanoinjection process. The nanoinjector mechanism is operated while submerged in a pH buffered solution (such as phosphate buffered saline, PBS). A positive electrical charge is applied to the lance, which accumulates negatively charged DNA [97] on its surface [41], [98]. The nanoinjector mechanism then penetrates the zygotic membranes, and a negative charge is applied to the lance, releasing the accumulated DNA within the cell.

As a means of delivering transgenes into the zygote's pronucleus, the nanoinjector mechanism has three main functions: first, elevate the lance from its as-fabricated position on the die surface; second, move the lance horizontally at a constant height, penetrating the elevated lance into the cell; and third, maintain electrical conductivity between the lance and an external voltage source. Constructing the nanoinjector as a self-reconfiguring metamorphic mechanism [3], [99]–[101] enables the first function (lance elevation) to be sequentially decoupled from the second function (horizontal lance motion). Decoupling the vertical and horizontal motion phases ensures that the lance penetrates the zygote's membranes and pronucleus along a linear, horizontal axis, and prevents tearing of the zygotic membranes.

This paper describes the design, testing, and refinement of the metamorphic nanoinjector mechanism. Viability of zygotes following penetration by the nanoinjector lance is also presented.

2.1.1 Current Methods of Direct Gene Delivery

Currently, direct microinjection of genetic material into mammalian zygotes uses a hollow needle (a micron-scale tapered glass micropipette) driven by a micromanipulator to penetrate the zygotic membranes and a pump to expel minute volumes of a nucleic acid solution into the zygote [52], [57]. Though significant improvements to microinjection equipment have been made [38], [44], the core elements of the needle-and-pump design paradigm have remained essentially unchanged since microinjection hardware first appeared in the literature over 50 years ago [54], [56].

Breaking from the needle-and-pump concept, MEMS DNA injection systems have been developed for adherent culture cells. These methods deliver DNA via fixed vertical nano-needles on a chip [102], [103], or modified atomic-force microscopy (AFM) probes [85], [104]. The fixed nano-needles require that the target cells grow with the needle's penetrating their surface, making fixed vertical needles impractical for transgenesis [102], [103]. The AFM probe based needles require several minutes of incubation in each cell, and do not have sufficient penetration into the target cell to reach the zygote's pronucleus [85], [104].

2.1.2 Metamorphic Mechanisms

Metamorphic mechanisms have multiple possible subphase mechanisms, where each subphase represents a unique configuration with distinct degrees of freedom [3]. In the case of the nanoinjector, the two subphases are out-of-plane elevation of the lance, and the horizontal motion of the lance. The metamorphic configuration with all of its degrees of freedom active is called a metamorphic source generator. As the metamorphic source generator is degenerated, its degrees of freedom are reduced, and it is reconfigured into one of its possible subphase mechanisms [100].

Reconfiguration can be achieved through altering the mechanism's links, joints, or geometry [101]. In joint-induced reconfiguration, the number of joints can be changed, as well as the joint type. For example, a universal joint could be degenerated to a revolute joint, reducing the joint's degrees of freedom from three to one [99]. The nanoinjector transitions between its two motion phases through joint-induced reconfiguration.

Many reconfigurable mechanisms require external intervention transition between subpahses. A user may lock a joint, remove a link, or alter the geometry. In [99], for example, universal joints are degenerated by placing them in a certain orientation, and locking one of their axes of rotation. In self-reconfiguration, as with the nanoinjector, no external intervention is required during metamorphosis; actuation of the mechanism causes the reconfiguration to occur.

2.1.3 Out-of-plane Surface Micromachined Mechanisms

Surface micromachined mechanisms can achieve out-of-plane displacements many times greater than their as-fabricated thickness through the use of specially designed joints [105], [106]. The out-of-plane revolute joints used in the nanoinjector can be categorized as "scissor joints" and "slider joints." Examples of each of these joint types are shown in Figure 2.3. The slider joints can undergo rotations of approximately 180 degrees, and the scissor joints can achieve rotations in excess of 90 degrees. These joints can be combined to create complex mechanisms, such as those in [25].

The limitations of multi-layer surface micromachining processes have a significant impact on the precision of scissor joint's motion. Parasitic motion is inherent in the joints because of the minimum gaps between features in the same layer, the minimum sizes of features, and between-

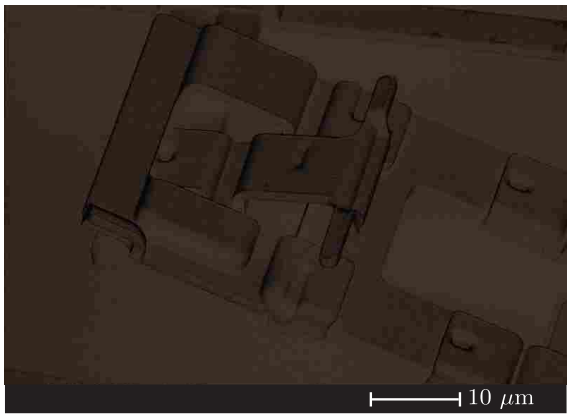

(a) SEM of a scissor joint

(b) SEM of a slider joint

Figure 2.3: Scanning electron microscope (SEM) images the two types of out-of-plane joints used in the nanoinjector: scissor joints and slider joints.

layer vias. Figure 2.4 shows two sources of parasitic motion in the scissor joint: one governed by minimum feature size, and the other governed by minimum gaps between features in the same layer. The kinematic models of the nanoinjector presented below account for these two types or parasitic motion.

2.1.4 Compliant Mechanisms and Pseudo-rigid Body Models

Compliant mechanisms achieve some or all of their motion through the deflection of flexible elements [2]. In many applications, compliant mechanisms are appealing because they can be designed to have very precise motion, to eliminate frictional wear, and to eliminate parasitic motion. Elimination of parasitic motion is particularly important for mechanisms fabricated on the micro-scale. As shown in Figure 2.4, micro-scale rigid link joints can have pronounced parasitic motion due to relatively large minimum gaps between features in the same layer. Typically, the clearances within a rigid-link micro-joint are roughly on the order of the dimensions of the joint itself. A fully compliant micro-mechanism, one which achieves its motion only through the deflection of compliant elements, can completely eliminate this source of parasitic motion.

Rigid-link kinematic modeling and synthesis techniques can be applied to a compliant mechanism by employing a pseudo-rigid body model (PRBM) of the mechanism's flexible elements [2]. The PRBM of a flexible element consists of a characteristic pivot and a pseudo-spring.

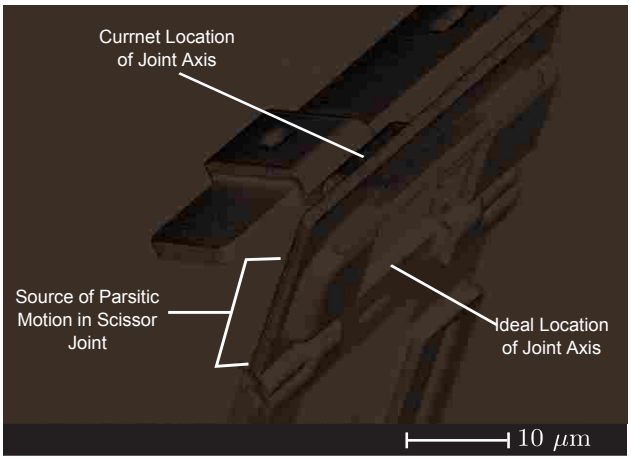

(a)

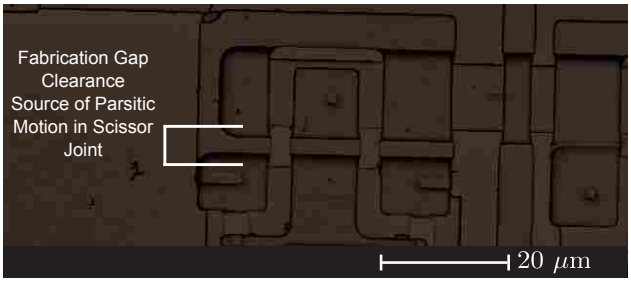

(b)

Figure 2.4: Scanning electron micrographs of the scissor joints in the nanoinjector mechanism showing (a) parasitic motion due to minimum feature size and (b) minimum gaps between features in the same layer.

The location of the characteristic pivot accounts for the deflection characteristics of the flexure, and the spring constant of the pseudo-spring accounts for the stiffness of the flexure. Additionally, the stresses in a flexure can be calculated from the displacement of the PRMB. Using the PRBM approach, models of a compliant mechanism's force-deflection and stress-deflection behavior can be developed.

2.2 Mechanism Description and Modeling

The nanoinjector mechanism consists of one rigid-body six-bar mechanism, one compliant parallel-guiding mechanism, and two compliant electrical connections, as shown in Figure 2.1(b). The rigid-body six-bar mechanism provides the out-of-plane displacement in the nanoinjector's first metamorphic subphase. The compliant parallel-guiding mechanism provides the in-plane

translation toward the target cell during the second subphase. The method of self-reconfiguration and models of each of the nanoinjector's components are described below.

Prototype nanoinjectors were fabricated using MEMSCAP Inc.'s polycrystalline silicon Multiuser MEMS Processes (polyMUMPs) [4]. The process provides one stationary polycrystalline silicon layer (POLY0), two structural layers of polycrystalline silicon (POLY1 and POLY2), and a gold layer for increasing electrical conductivity which may be added to the POLY2 layer. The POLY1 and POLY2 layers are 2.0 μm and 1.5 μm thick respectively.

2.2.1 Self-reconfiguration through Unequal Subphase Mechanism Stiffnesses and Link Contact

The nanoinjector's sequential "up-then-forward" motion is a key element of the mechanism's functionality. Self-reconfiguration in the nanoinjector is a consequence of the unequal force-displacement characteristics of the six-bar mechanism and the folded-beam suspension, and contact between links in the nanoinjector mechanism. The nanoinjector's motion and idealized force-displacement relationship are shown schematically in Figure 2.5, and a kinematic diagram of the six-bar mechanism is shown in Figure 2.6. At position 0, the nanoinjector is in its as-fabricated configuration, with the six-bar mechanism mounted on to the folded-beam suspension. In other words, it is as if the six-bar mechanism is kinematically grounded to the folded-beam suspension rather than the substrate.

Between positions 0 and 1, the nanoinjector is in its first subphase, with the lance moving out-of-plane. This motion raises the lance to the desired level, but occurs away from the zygote to prevent damage to the cell membrane. Assuming negligible friction in the six-bar's slider and scissor joints, actuation between positions 0 and 1 applies approximately zero force to the folded-beam suspension. With negligibly small force applied to the folded-beam suspension by the six-bar mechanism, there is no in-plane translation from the deflection of the folded-beam suspension's compliant flexures.

At position 1, contact is made between the input slider and the folded-beam suspension. This effectively locks the prismatic (slider) joint shown in Figure 2.6 and fixes the length R_6. With this degree of freedom removed, the six-bar mechanism becomes a structure with respect to the fold-beam suspension. Between positions 1 and 2, the six-bar mechanism remains at the

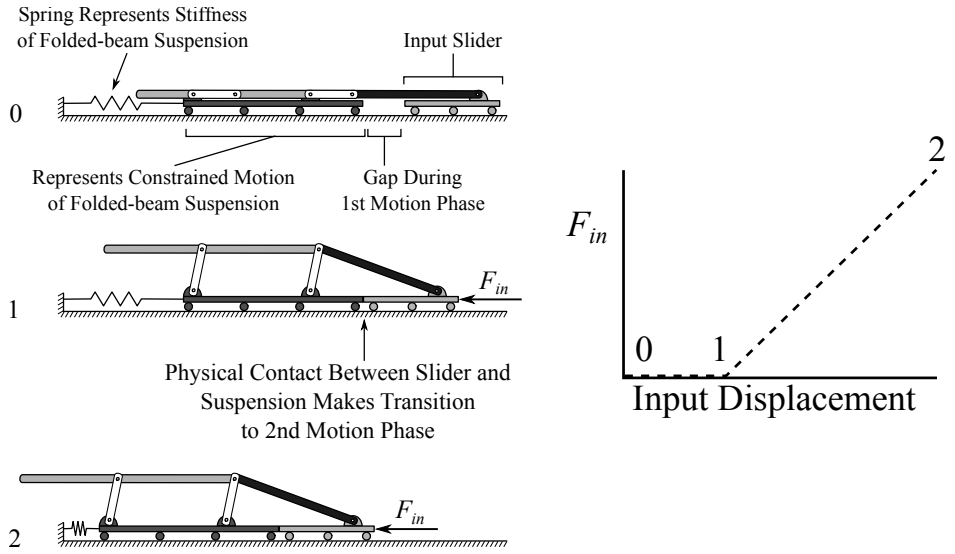

Figure 2.5: Schematic illustration of the nanoinjector's motion and idealized force displacement characteristics. The folded-beam suspension's suspension is approximated as the linear spring at left. At position 0, the nanoinjector is in its as-fabricated configuration. Between positions 0 and 1, the nanoinjector is in its first subphase, and between positions 1 and 2, the nanoinjector is in its second subphase.

same elevation as position 1 while the folded-beam suspension deflects, resulting in an in-plane translation of the lance. This in-plane translation allows a linear motion of the raised lance such that minimal damage to the cell membrane occurs during lance penetration. Pulling back on the input slider, the mechanism will proceed from position 2, to 1, back to 0.

2.2.2 Modeling the Six-bar Mechanism

If the scissor and slider joints in the nanoinjector six-bar mechanism are treated as idealized revolute joints, the mechanism can be modeled as shown in Figure 2.6. Due to the planar nature of surface micromachining, the mechanism is fabricated in a change-point configuration, with all of its links co-planar. However, the mechanism can achieve only the configuration pictured because the the other kinematic configurations are only possible if one or more links move in the negative z-direction (through the substrate).

In the nanoinjector, links R_1 and R_3 are the same length, as are links R_2 and R_4. Thus, the mechanism can be modeled as a parallel-guiding (parallelogram) four-bar mechanism (links R_1 through R_4) with a driver dyad (R_5 and the input slider). The parallel-guiding motion of the six-bar

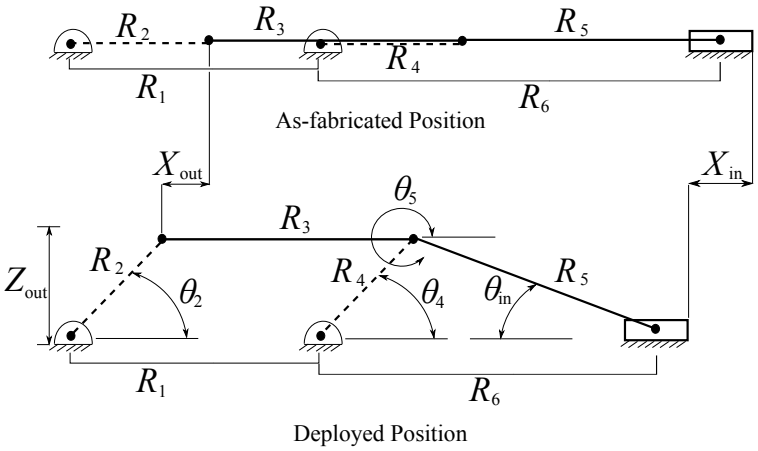

Figure 2.6: Kinematic diagram of the change-point six-bar mechanism.

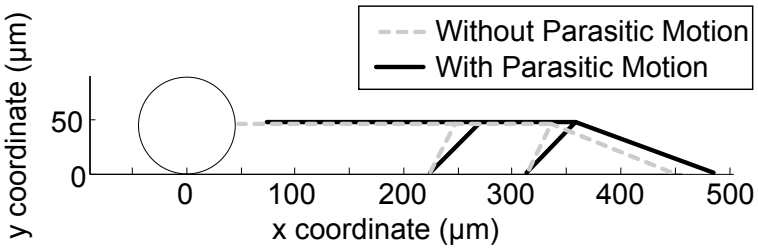

Figure 2.7: Kinematic diagram of the change-point six-bar mechanism showing the differences between the compensated and uncompensated kinematic models. Note that the kinematics parameters chosen make the final out-of-plane displacement (Z_{out}) relatively insensitive to the parasitic motion in the scissor joints.

mechanism ensures that the lance will be horizontal through out its motion. The position of the mechanism can be calculated by

$$\theta_4 = \cos^{-1}\frac{(R_4+R_5-X_{in})^2+R_4^2-R_5^2}{2R_4(R_4+R_5-X_{in})} \tag{2.1}$$

$$\theta_5 = 2\pi+\sin^{-1}(R_4\sin\theta_4/R_5) \tag{2.2}$$

$$\theta_{in} = \theta_5-\pi \tag{2.3}$$

$$Z_{out} = R_4\sin\theta_4 \tag{2.4}$$

$$X_{out} = R_4(1-\cos\theta_4) \tag{2.5}$$

where $\theta_2=\theta_4$ because of the parallelogram configuration.

Idealizing the scissor joints as pure revolute joints can be a poor assumption given the amount off parasitic motion that is possible (see Figure 2.4). The parasitic motion in the scissor joints on links R_2, R_4, and R_5 can approximately be modeled through adjusting the lengths of links, and the input displacement X_{in} by

$$R_2' = R_2 + P_l \tag{2.6}$$

$$R_4' = R_4 + P_l \tag{2.7}$$

$$R_5' = R_5 + P_l \tag{2.8}$$

$$X_{in}' = X_{in} + 3P_g \tag{2.9}$$

where P_l is the change in link length possible in the scissor joint (see Figure 2.4(a)), and P_g is the gap between the links connected by a scissor joint when the mechanism is in its as-fabricated position (see Figure 2.4(b)). The factor P_g is multiplied by 3 to account for each of the three unique scissor joints in the mechanism: R_2 to R_3, R_3 to R_5, and R_4 to R_5. The dimensions given in Table 2.1 were chosen to reduce the effects of parasitic motion on the lance's final out-of-plane displacement (Z_{out}). Figure 2.7 shows kinematic models of the nanoinjector both with and without accounting for the parasitic motion in the scissor joints.

Table 2.1: Dimensions of the lance six-bar mechanism shown in Figure 2.1(b) and 2.6. Link lengths and positions given in parenthesis take into account the parasitic motion given by Equations 2.6–2.9. All dimensions are in μm unless otherwise noted.

Link or Parameter	**Value**
$R_1 = R_3$	90.0
$R_2 = R_4$	50.0 (66.5)
R_5	120.0
X_{in}	37.0 (28.0)
Z_{out}	45.0 (47.1)
X_{out}	28.2 (19.6)
Lance Length	200.0
Lance Taper	3°
P_l	16.5
P_g	3.0

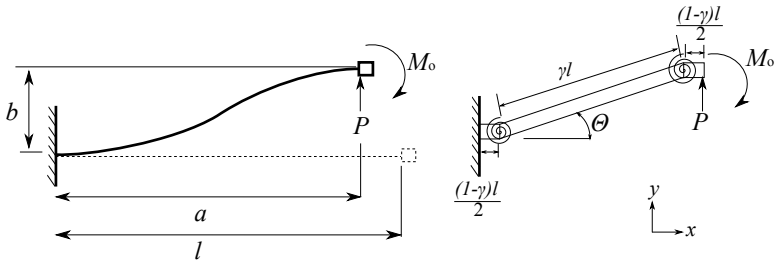

Figure 2.8: A schematic of a fixed-guided beam and its pseudo-rigid-body model.

2.2.3 Modeling the Folded-beam Suspension

The fully compliant folded-beam suspension was analyzed using a psuedo-rigid body model (PRBM) and non-linear finite element analysis. The eight fixed-guided compliant flexures are 300 μm long, 5 μm wide, and 2 μm thick (POLY1). As shown in Figure 2.8, the PRBM of a fixed guided beam consists of one pseudo-rigid link and two pseudo-springs. The input force, P, and maximum stress in the flexure, σ_{max}, can be found by

$$\Theta = \arcsin\frac{b}{\gamma l} \tag{2.10}$$

$$\alpha^2 = 2K_\Theta \tag{2.11}$$

$$P = 4\alpha^2 EI/l^2 \tag{2.12}$$

$$a = l(1-\gamma(1-\cos\Theta)) \tag{2.13}$$

$$\sigma_{max} = \frac{Pa(\frac{h}{2})}{2I} \tag{2.14}$$

where b and a are the y and x coordinates of the end of the beam, E is Young's modulus for polysilicon ($\approx$ 164 GPa), I is the second moment of area for a rectangular beam, $\gamma = 0.8517$, and $K_\Theta = 2.65$ [2].

The folded-beam suspension's eight compliant flexures are in a parallel and series arrangement. The right and left halves of the suspension are in parallel. Within each half, the pair of outer flexures is in series with the pair of inner flexures. Additionally, the two outer flexures are in parallel with each other, and the two inner flexures are a in parallel with each other. Summing the parallel and series stiffnesses and displacements, the full suspension has the net-stiffness of four parallel-guiding flexures which displace one-half the total displacement of the suspension. The

calculated input force and maximum stress predicted by the pseudo-rigid-body model for a total stage displacement of 70 μm (each flexure displacing 35 μm) are given in Table 2.2.

In addition to the pseudo-rigid body model, a non-linear (large deflection, small strain) finite element analysis (FEA) was performed on the folded-beam suspension using ANSYS 11.0. The suspension was meshed with quadratic 20-node tetrahedral elements. The model was fixed at two anchor areas, and displaced 70 μm in-plane at the point of contact between the folded-beam suspension and the input slider, as shown in Figure 2.9. The input force and the maximum stresses predicted by the FEA are compared with the PRBM results in Table 2.2. The FEA results and the PRBM results agree to within 11% for for the input force, and 5% for the maximum stress. The stresses predicted by both models are below the ultimate strength of polycrystalline silicon [107].

2.2.4 Modeling the Compliant Electrical Connections

The serpentine flexure [108] electrical connections between the nanoinjector and the stationary bond-pads are designed to provide electrical conductivity without interfering with the nanoinjector's motion. Only a finite element analysis of the electrical connections was performed because there is no closed-form or pseudo-rigid body model for the serpentine flexures' non-linear three-dimensional loading. An electrical connection was modeled using quadratic 20-node tetrahedral elements. One end of the electrical connection was fixed in all degrees of freedom, while the other was displaced 50 μm in the z-direction (out-of-plane) and 110 μm in the y-direction (in-plane), as indicated in Figure 2.10.

Initially, the finite element model only included the electrical connection. However, this initial model predicted significant displacements into the substrate (negative z-direction) by part of the electrical connection. To more accurately predict the electrical connection's final configuration and stress state, the interaction between the electrical connection and the substrate was modeled

Table 2.2: Comparison of pseudo-rigid-body model and finite element analyses of the folded-beam suspension.

	PRBM	**FEA**
Force Total	222 μN	198 μN
Maximum Stress	993 MPa	1033 MPa

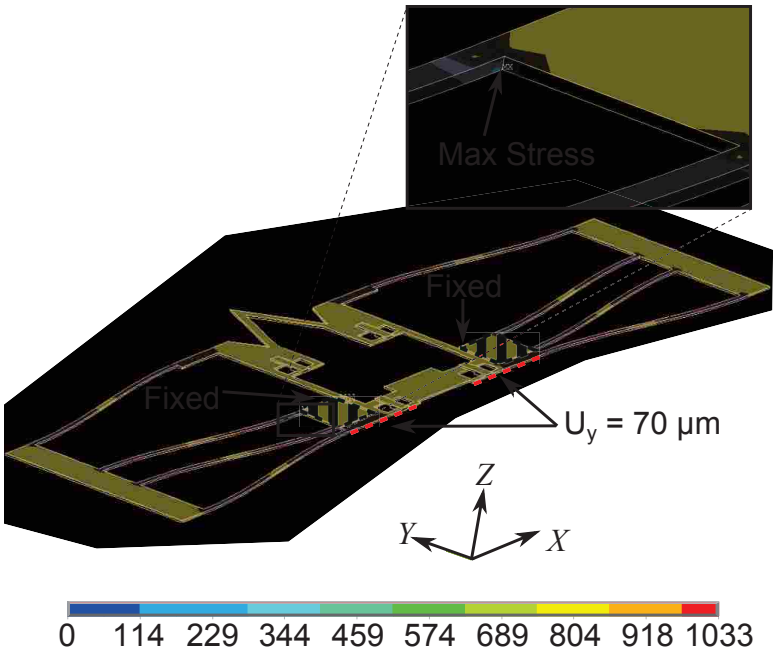

Figure 2.9: Finite element model Von Mises stress contours for the folded-beam suspension undergoing 70 μm of displacement in the y-direction. The two areas indicated in red cross-hatching were fixed in all degrees of freedom. The y-direction input displacement was applied to the surfaces indicated. Stresses are in MPa.

as an initially open contact pair, with the substrate being modeled as perfectly rigid. Figure 2.10 shows the deformed shape and Von Mises stress contours of the fully displaced electrical connection. Table 2.3 gives the reaction forces and moments for one and both electrical connections. The reaction forces are small in comparison to the total forces required to displace the compliant stage, and in testing have not interfered with the nanoinjector's motion.

Table 2.3: Reaction forces applied to the lance mechanism by one or both electrical connections for a displacement of 50 μm in the z-direction (out-of-plane) and 110 μm in the y-direction (in-plane). Note that the x-direction of force sums to zero because it is in opposite directions for each connection.

	One	**Both**
F_x **Total**	$\pm 3.51 \mu$N	0μN
F_y **Total**	1.70μN	3.40μN
F_z **Total**	-16.0 μN	-32.0 μN

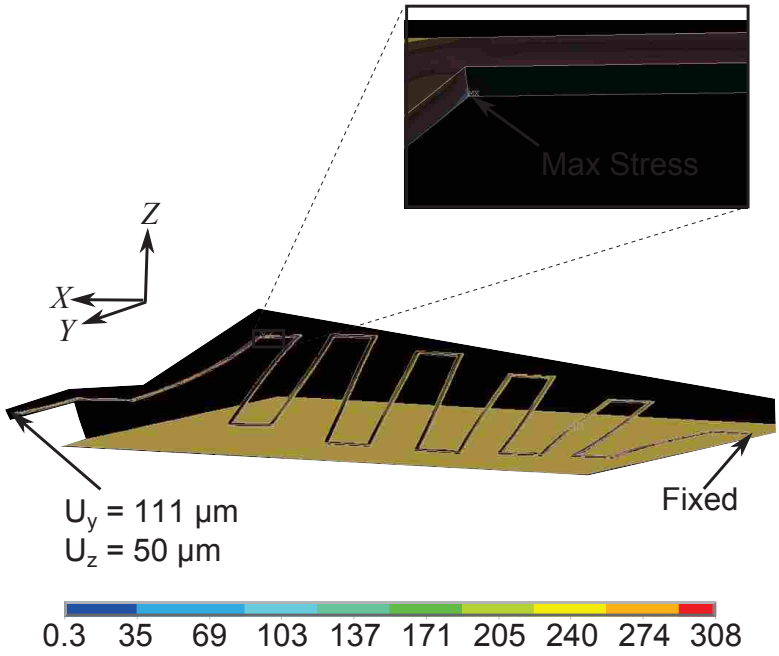

Figure 2.10: Finite element model Von Mises stress contours for the electrical connections undergoing 50 μm in the z-direction (out-of-plane) and 110 μm in the y-direction (in-plane). Stresses are in MPa.

2.3 Mechanical Testing of Prototype Nanoinjectors

This section provides verification of the nanoinjector's metamorphic motion through mechanical testing of the nanoinjector. The mechanism's metamorphic motion is demonstrated, and embryo survival results are presented for nanoinjections into mouse zygotes (single-cell fertilized egg cells). The embryo survival data is especially important because it demonstrates that the nanoinjector's metamorphic motion allows the lance to consistently penetrate the zygote's membranes without tearing or damaging the membranes. Full nanoinjection protocols and data on successful nanoinjection of DNA into mouse embryos will be presented in other literature where the biological experiments can be discussed in detail.

2.3.1 Verification of Metamorphic Motion

The nanoinjector mechanism is actuated by applying a linear input with a tungsten microprobe attached to a micromanipulator. Figure 2.11 shows optical microscopy images of the nanoinjector mechanism in its un-actuated position, its first metamorphic subphase (out-of-plane elevation

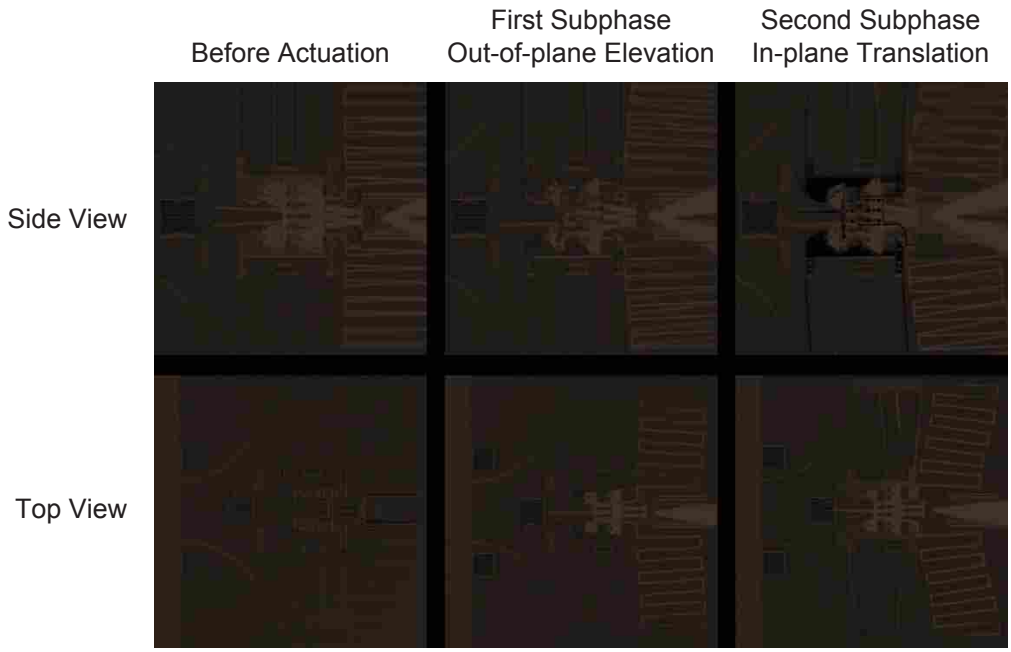

Figure 2.11: Top and side view optical microscopy images of the nanoinjector's motion.

of the lance), and its second subphase (in-plane translation). As described previously, the six-bar mechanism reaches its full out-of-plane elevation with negligible translation in the folded-beam suspension. Applying further actuation, the lance remains at a constant height above the substrate as the folded-beam suspension deforms.

Figure 2.11 also subtly illustrates the potential for parasitic out-of-plane motion inherent in thin film compliant mechanisms. At best, the polyMUMPs process can offer out-of-plane aspect ratios ≤ 1.167, leading to compliant flexures with out-of-plane stiffnesses which may be less than or equal to their in-plane stiffnesses. Any eccentricity in the applied in-plane loads may excite these out-of-plane displacements. A careful examination of the folded-beam suspension in the top view images in Figure 2.11 reveals changes in the suspension's brightness. The darker areas are coming out-of-plane, and are reflecting light away from the microscope. Parasitic out-of-plane motions in the folded-beam suspension can be minimized through the addition of POLY2 "staples" over POLY1 features or by maximizing the out-of-plane aspect ratio.

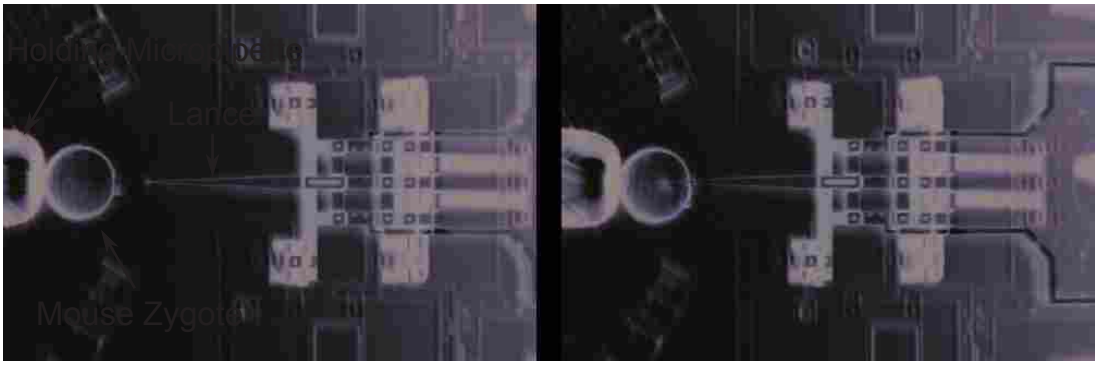

Figure 2.12: Optical microscopy images of before (left) and during (right) nanoinjection of a mouse zygote.

2.3.2 Mouse Zygote Survival Following Lance Penetration

The most meaningful measure of the quality and repeatability of the nanoinjector mechanism's motion is the survival of mouse zygotes following piercing of the zygotic membranes. Ideally, penetration into a zygote occurs along the membrane's surface-normal vector at the point of penetration. Deviation from this vector, such as in-plane or out-of-plane translation and/or rotation of the lance, will cause tearing of the zygote's membranes and death of the cell.

Zygotes for nanoinjection were harvested from superovulated CD-1 female mice. Details of the superovulation and harvesting protocols employed can be found in [51] and are not presented here for brevity. Zygotes were either untreated (placed directly into culture), or were nanoinjected following the protocol outlined in Figure 2.2. For all of the nanoinjections reported here the lance was charged to 1.5 V prior to penetration into the zygote, and charged to -1.5 V for 10 seconds during penetration. Nanoinjected and untreated zygotes were then cultured for 24 hours and the rate of progression from one-cell zygotes to two-cell embryos was recorded.

Figure 2.12 shows the nanoinjector and a zygote before and during lance penetration. Figure 2.13 presents the proportion of zygotes progressing to the two cell stage from untreated (1917/2407 = 79.6%) and nanoinjected (2134/2968 = 71.9%) groups. The error bars on the proportions were calculated using the logit interval presented in [109] with a 95% confidence level. The rates of survival for the untreated and nanoinjected embryos are quite similar, differing by 7.7%, and with the confidence intervals separated by 3.5%.

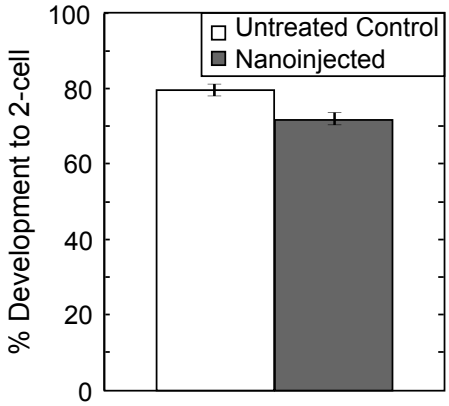

Figure 2.13: Rate of development from single cell embryos (zygotes) to two-cell embryos for untreated (1917/2407 = 79.6%) and nanoinjected (2134/2968 = 71.9%) embryos. Confidence intervals are 95% logit confidence intervals for binomial proportions.

2.4 Discussion of Results

The data presented above was gathered throughout the development of the nanoinjector by multiple users and with multiple nanoinjector prototype iterations. The images in Figure 2.11 and Figure 2.12 show that the nanoinjector has the intended self-reconfiguring metamorphic motion. The close similarity between the viability of untreated and nanoinjected embryos indicate that the nanoinjection process is well tolerated by mouse zygotes. More specifically, these results demonstrate that the nanoinjector's metamorphic motion accomplishes the design goal of penetrating the cell without causing significant cellular damage. Additionally, the small impact on zygote viability across thousands of nanoinjections shows that mechanically successful nanoinjection (lance penetration without cellular damage) is highly consistent.

Observing the nanoinjector's motion and impact on embryo viability has led to multiple improvements in the nanoinjector design. The data in Figure 6.7 includes data from successful experiments with higher embryo viability, and from experiments with lower embryo viability. The experiments with lower embryo viability provided several qualitative observations leading to improvements of the nanoinjector mechanism. Figure 2.14 shows four iterations on the nanoinjector design over the course of seven polyMUMPs production runs spanning from 2007 to 2011; other iterations not shown here were also developed and tested. Some of the design improvements have included:

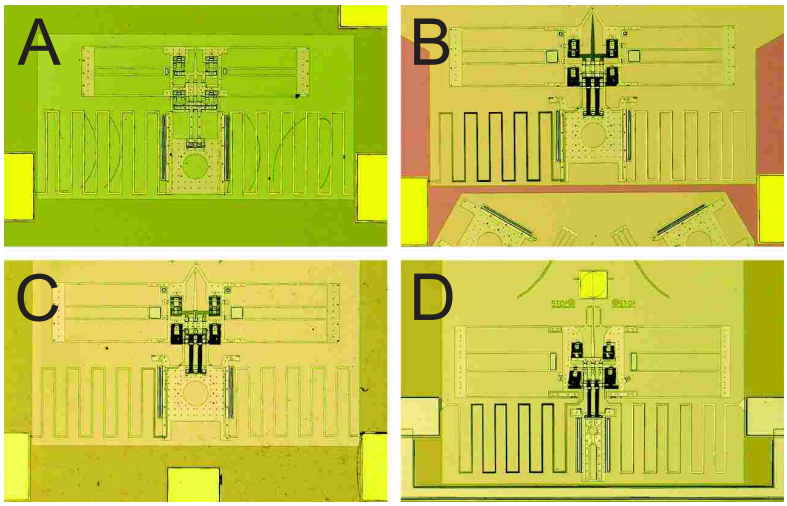

Figure 2.14: Four nanoinjector designs highlighting some of the refinements of the nanoinjector over the course of its testing. The designs proceed from earliest at top, to most recent at bottom. Some example differences between the mechanisms include: elongating the lance, reducing the angle at the tip of the lance, and using link lengths which are more robust to parasitic motion.

- Changing the lengths of the six-bar mechanism's links to be more robust to parasitic motion in the scissor joints.
- Increasing length of the lance from 75 μm (Figure 2.14 A) to 200 μm (Figure 2.14 D).
- Changing the lance from POLY1 (2 μm thick) (Figure 2.14 A,B) to POLY2 (1.5 μm thick) (Figure 2.14 C,D). Decreasing the thickness of the lance decreases the deformation of the cell during lance penetration.
- Reducing the in-plane taper on the lance from 10° (Figure 2.14 A), to 6° (Figure 2.14 B), to 5° (Figure 2.14 C), and finally to 3° (Figure 2.14 D). Decreasing the in-plane taper of the lance decreases the deformation of the cell during lance penetration. The lance tip shown in Figure 2.1(c) demonstrates the fine tip geometry achieved using the 3° taper for the mask layout.
- Rerouting the electrical connections in front of, rather than over, the input slider (compare Figure 2.14 A–C and Figure 2.14 D). This prevents the electrical connections from binding on the fixed portions of the slider.

- Reducing the width of the input slider to reduce binding (compare Figure 2.14 A–C and Figure 2.14 D).
- Adding markings to identify the limits of the first subphase's out-of-plane motion and the second subphase's in plane motion (Figure 2.14 D).

2.5 Conclusion

The metamorphic nanoinjector mechanism successfully meets its designed goal of penetrating the lance into mouse zygotes without causing significant damage to the cellular membranes. Metamorphic self-reconfiguration between the first subphase (the six-bar mechanism's out-of-plane motion) to the second subphase (the folded-beam suspension's in plane translation) occurs simply by advancing the mechanism's input slider. Through thousands of mechanism actuations and lance penetrations into mouse zygotes, the nanoinjector consistently followed its intended motion path into the target zygote. Nanoinjection of nearly 3000 zygotes has resulted in 71.9% progression to the two-cell stage.

Refinements to the nanoinjector have improved the mechanism's performance. Future work will further improve on the accuracy and repeatability of the nanoinjector's motion. Possible areas for improvement may include reducing parasitic motion in the scissor joints and reducing out-of-plane motion by the folded-beam suspension. A fully compliant nanoinjector, with no scissor joints or slider joints, could improve the precision of the lance's motion by eliminating the parasitic motion caused by the rigid joints.

CHAPTER 3. PRONUCLEAR DNA TRANSFER VIA NANO-FEATURED LANCE AND METAMORPHIC MICROELECTROMECHANICAL SYSTEM

3.1 Introduction

Transgenic animals were first produced in the early 1980s [5], [60], [110] and have been instrumental to research of the genetic underpinnings of cancer [90], [91], Alzheimer's disease [21], [92], immune response [16], [111], and many other diseases and biological processes. Genetically modified animals can be produced by microinjecting a DNA solution into a zygote's pronucleus through a hollow needle (a micron-scale glass micropipette) [52]. Pronuclear microinjection of DNA has been refined over the last 30 years, but the underlying concept has remained unchanged. Injection of liquid into the pronucleus is a challenging process because of the potential for cell lysis [57] and chromosomal damage [66].

In part, these challenges motivated the development of various indirect methods of transgenesis, such as embryonic stem cell injection [112], intracytoplasmic sperm injection [67], and viral transfection [113]. In these alternative methods, a transgene is inserted into cells or virus particles, which in turn act as carriers, delivering the genetic material to an oocyte or embryo. Other researchers have developed non-fluidic DNA injection methods based on bulk micromachined or carbon nanotube-formed microelectromechanical systems (MEMS) [85], [102]–[104]. These MEMS-based gene delivery systems have high rates of transgene delivery and post-injection cell viability. However, these MEMS are not well suited for transgenic animal production because they require cells to grow around stationary needles [102], [103] or require 1–15 minutes to release bound DNA into the cells [85], [104], making their use impractical for DNA introduction into zygotes. In addition, these devices do not have sufficient mechanical motion to penetrate into a zygote's pronucleus [85], [102]–[104].

We have developed a surface-micromachined device (Figure 3.1, Figure A.1) to perform what we call nanoinjection, a new method of electro-physical pronuclear injection of DNA into

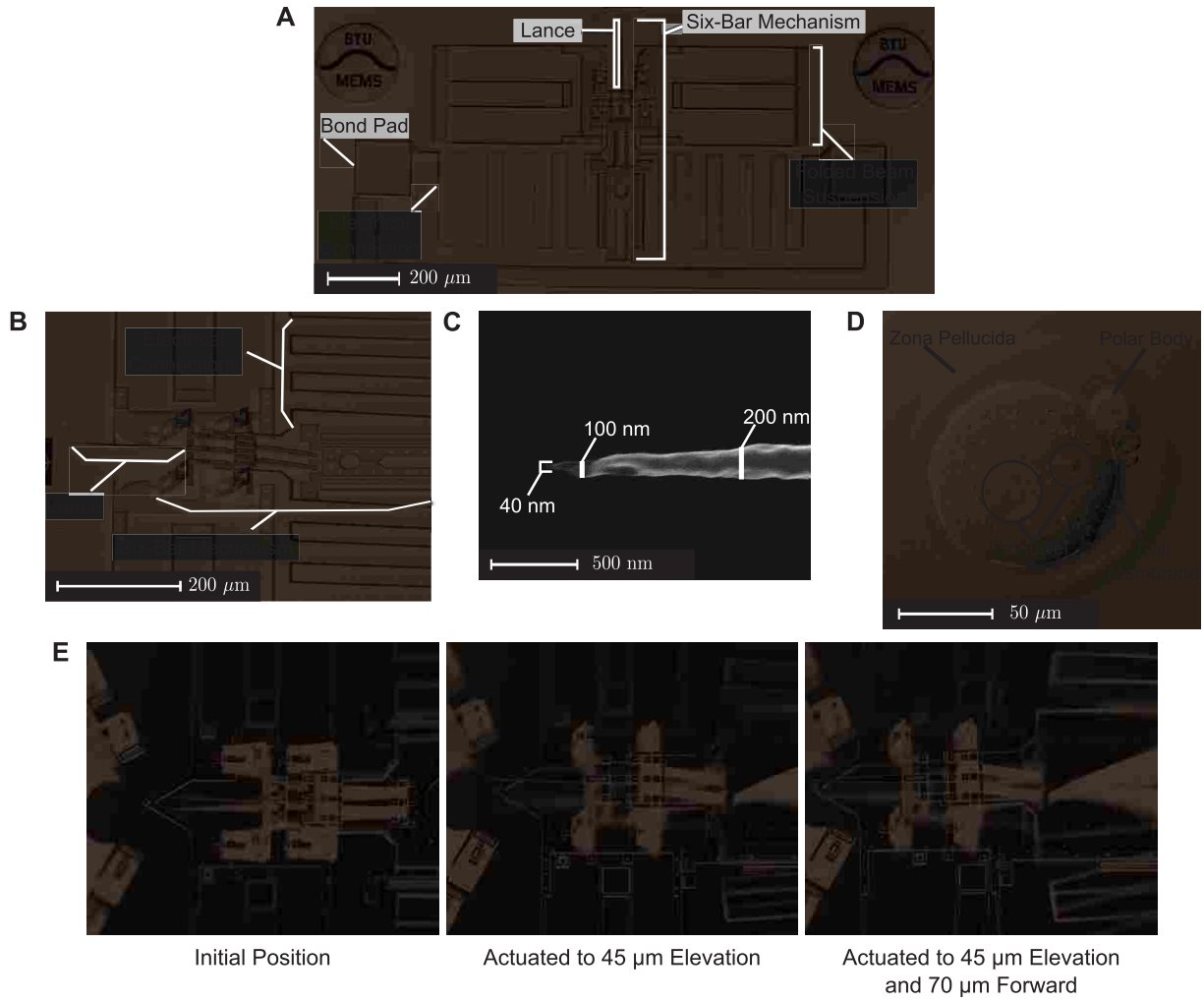

Figure 3.1: Images of the nanoinjector, nanoinjector lance and a typical mouse zygote. (A) Labeled scanning electron micrograph of the nanoinjector, (B) angled view of a partially actuated nanoinjector, (C) scanning electron micrograph of the tip of the nanoinjector lance, (D) labeled confocal microscopy image of a mouse zygote, and (E) optical microscopy of the two-stage, metamorphic motion of the nanoinjector lance.

zygotes. The nanoinjection process can be summarized in three broad steps (Figure 3.2). First, applying a positive charge to a nano-featured lance (Figure 3.1A, C) accumulates DNA from the surrounding solution onto the lance's surface. Second, mechanically actuating the nanoinjector mechanism (Figure 3.1B and E) pushes the DNA-coated lance into the zygote and pierces the pronucleus (Figure 3.1D). Third, applying a negative charge to the lance releases DNA inside the pronucleus. Once DNA is released, the lance is removed from the cell.

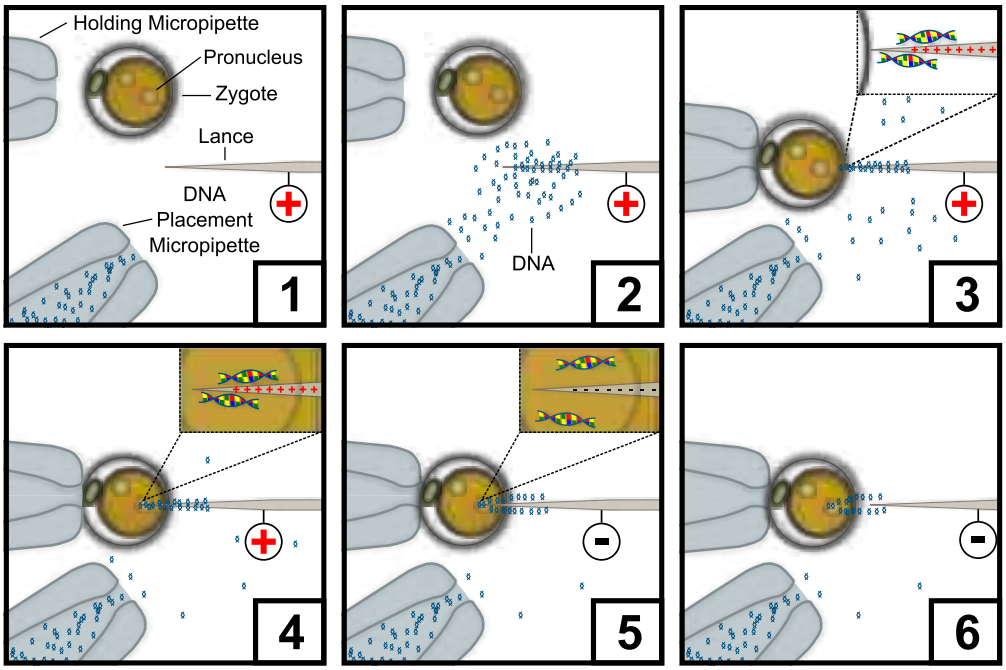

Figure 3.2: Illustration of the nanoinjection process showing the six steps in the process. (1) the lance is positively charged; (2) a DNA solution is placed near the lance; (3) DNA electrically accumulates while the zygote is oriented and placed in front of the nanoinjector using a holding pipette; (4) the nanoinjector inserts the lance into the pronucleus; (5) the lance is negatively charged, releasing DNA into the pronucleus; (6) the lance is withdrawn.

Electrical accumulation and release of DNA is possible because of the unequal charge distributions within DNA molecules. With an effective charge of two electrons per base pair [97], DNA in solution can be manipulated by electric fields and static electric charges generated by both macro-scale and micro-scale electrodes [29], [41]. If the voltage applied to the electrodes exceeds the decomposition voltage, DNA in the solution will move via electrophoresis [114], [115], and electrolysis of the surrounding water may also occur, potentially oxidizing and damaging MEMS devices [41]. Below the decomposition voltage, DNA physically contacting a positively charged electrode still accumulates on the electrode's surface, and electrolysis does not occur, but DNA does not experience sustained electrophoresis. Similarly, the accumulated DNA will be released, but not electrophoretically repelled, from the electrode's surface by reversing the electrode's polarity [41]. We performed all of the nanoinjection experiments reported in this work with the lance operating below the decomposition voltage to prevent electrolysis from damaging the device or the zygotes.

This work presents the nanoinjector system and the results of nanoinjections into mouse zygotes. The nanoinjector system provides the necessary electrical properties, nano-scale features, and precise motion to enable electro-physical injection of DNA into mouse zygotes. We studied the in-vitro viability of mouse zygotes following nanoinjection, and found that penetrating the electrically charged lance into the pronucleus does not have a significant impact on the zygotes' viability. We then performed side-by-side nanoinjection and microinjection of a transgene encoding green fluorescent protein into mouse zygotes. Using the microinjected zygotes as a positive control, and as a baseline for comparison, we found that nanoinjection produced transgenic mice with high rates of zygotic and gestational viability.

3.2 Materials and Methods

Complete descriptions of each of the protocols used in this study are presented in Appendix A.

3.2.1 Nanoinjector Devices

MEMSCAP Inc. fabricated all of the nanoinjector devices used in this work through their polysilicon Multi-User MEMS Processes (polyMUMPs). We removed the sacrificial phosphosilicate glass from the devices with hydrofluoric acid. We then adhesively bonded the nanoinjector chips to 35 mm in-vitro fertilization dish lids. Transgene Preparation We replicated the pCAG-EGFP or pCAG-RFPmonomer plasmids in DH-5α E. coli bacteria. We then isolated the CAG-EGFP or CAG-RFPmmonomer genes from the plasmids by endonuclease digestion, agarose gel electrophoresis separation of the digestion products, and column chromatography to separate transgene copies from the agarose.

3.2.2 Mouse Care and Embryo Culture

All animal use in this study followed protocols approved by the respective institutions' animal care and use review boards. For the in-vitro viability study, we harvested zygotes from superovulated, outbred CD-1 female mice crossed with CD-1 male mice 0.5 days post coitus. We separated the zygotes from the cumulus mass with hyaluronidase, and cultured the zygotes

in KSOM media under silicone oil at 37 C and 5% CO2 before and after nanoinjection. For the in-vivo studies, zygotes were similarly harvested from C7Bl/6J x CBA/J F1 mice and cultured in M16 media. At 1.5 days post coitus, experienced technicians counted and transferred the two-cell embryos into pseudo-pregnant C57Bl/6J x CBA/J F1 females.

3.2.3 Flow Cytometry

We diluted blood samples obtained from weaned pups in PBS containing heparin, and obtained peritoneal exudates by peritoneal lavage with Hanks balanced salt solution. We homogenized thigh muscle, brain, and gut tissue samples in Hanks, and then filtered each sample. All samples were stored on ice prior to flow cytometry.

3.2.4 Polymerase Chain Reaction

We extracted DNA from tail biopsies through overnight proteinase K digestion and isopropanol precipitation. To ensure DNA quality, we assayed each sample for the mouse β-actin gene using the forward primer 5'-GTGGGCCGCTCTAGGCACCA-3' and reverse primer 5'-CGGTTGGCCTTAGGGTTCAGGG-3' which yielded a 244 bp product (see Figure A.2). We assayed for the presence of the EGFP transgene using the forward primer 5'-TGCCCGAAGGCTACGTCC-3' and reverse primer 5'-GCACGCTGCCGTCCTCG-3' which yielded a 267 bp product (see Figure A.2).

3.2.5 Statistical Analysis

Confidence intervals for the proportions reported in Figure 3.4, 5, and 6 were calculated using Agresti-Coull binomial confidence interval midpoints and bounds with $\alpha = 0.05$ [109]. The true proportion of successes for a process (i.e. the true proportion of zygotes surviving to the two-cell stage following nanoinjection) is assumed to lie within the intervals with $(1-\alpha)\%$ certainty. For a given α, the width of the Agresti-Coull binomial confidence intervals decreases as the number of observations increases. In other words, the observed proportion of successes is more likely to be near the true proportion of successes as the number of observations increases.

Statistical differences between the groups were found using Fisher's exact test with two tails [116], [117], and quantitative comparisons were made using the odds ratio for 2×2 contingency tables [117]. The odds ratio is a descriptive statistic which estimates how many times higher the odds are of observing a result (i.e. two-cell development) in one treatment (i.e. nanoinjection) compared to another treatment (i.e. microinjection).

3.3 Results and Discussion

3.3.1 The Nanoinjector can Mechanically and Electrically Interact with Mouse Zygotes

Like pronuclear microinjection [49]–[52], nanoinjection aims to directly deliver transgene copies to the pronucleus to improve the probability of transgene integration into the mouse's genome. A mouse zygote's two pronuclei are ≈15–19 μm in diameter and are located within the ≈70 μm diameter cell. The cell is surrounded by a ≈90–95 μm diameter glycoprotein membrane (the zona pellucida). To successfully deliver transgene copies to the pronucleus, the nanoinjector must accomplish two tasks without damaging the target zygote. First, the nanoinjector mechanism must precisely penetrate the zona pellucida, cell membrane, and pronuclear membrane. Second, the nanoinjector must maintain an electrical charge on the lance to accumulate, retain, and release DNA.

Nanoinjections occur with the nanoinjector chip and the zygotes to be injected submerged in 1.5–2 ml of room temperature phosphate buffered saline (PBS). Each nanoinjection follows the process shown schematically in Figure 3.2. An off-chip voltage source applies a positive charge at +1.5 V to the nanoinjector (which is below the decomposition voltage of the system). A syringe pump expels a solution of DNA from a stationary micropipette toward the nanoinjector lance. As demonstrated in [41], DNA contacting the lance accumulates on the lance's surface and can remain accumulated on the lance for up to several minutes while the zygote is oriented and placed in front of the lance with a holding micropipette. A micromanipulator actuates the nanoinjector forward, and the lance pierces the zona pellucida, cell membrane, and pronuclear membrane. With the lance in the pronucleus, the off-chip voltage source applies a negative charge at -1.5V to the lance, releasing the accumulated DNA. After a brief incubation in the pronucleus (≈10 seconds), the

micromanipulator retracts the nanoinjector mechanism, withdrawing the nanoinjector lance from the zygote.

To achieve the required precise mechanical penetration into the pronucleus, the nanoinjector has a nano-featured lance (Figure 3.1C), and a unique two-stage, metamorphic [3] motion (Figure 3.1E). The nanoinjector is fabricated from two polycrystalline silicon layers (2.0 μm and 1.5 μm thick). The lance has a nominal thickness of 1.5 μm and a minimum tip width below 40 nm (Figure 3.1C). The cross-sectional area at the lance's tip (0.06 μm2) is significantly smaller than that of a 1 μm outer diameter microinjection needle (0.78 μm2). The lance's small size allows it to penetrate into the pronucleus while causing minimal damage to the zygote's membranes. For the lance to reach the pronucleus, it must have significant out-of-plane (vertical) and in-plane (horizontal) motion relative to its as-fabricated position.

Before actuation, the nanoinjector lies in a planar configuration with its two polycrystalline silicon layers parallel to the fabrication substrate. The nanoinjector's metamorphic motion consists of two distinct, decoupled motion phases: out-of-plane elevation of the lance, and pure horizontal translation of the lance. When actuated by a micromanipulator, the nanoinjector's parallel-guiding, change-point, six-bar mechanism [25] first rises from its as-fabricated position to a final height of 45 μm (approximately the radius of a mouse zygote), while moving 28 μm horizontally and maintaining the lance parallel to the chip substrate (Figure 3.1E). With continued micromanipulator actuation, the compliant [2] folded beam suspension (Figure 3.1A and B) deflects and the nanoinjector then translates 70 μm horizontally toward the zygote with the lance at a constant height parallel to the substrate (Figure 3.1E). The nanoinjector's metamorphic motion allows the lance to remain parallel to the substrate at a constant elevation as it enters the zygote, thereby preventing both membrane tearing and lysis.

The lance must maintain its charge to retain accumulated DNA while passing through the zona pellucida, the cell membrane, and the pronuclear membrane. A tungsten microprobe connects one of the nanoinjector's stationary bond pads (Figure 3.3A, B) to one terminal of an off-chip voltage source. A second tungsten microprobe connects one of the gold-coated counter electrodes on the chip substrate (Figure 3.3A) to the other terminal of the voltage source. Throughout the nanoinjector's 45 μm vertical displacement and 98 μm total horizontal displacement, flexible electrical connections (Figure 3.1A, B) provide a current path from the nanoinjector's stationary bond pads

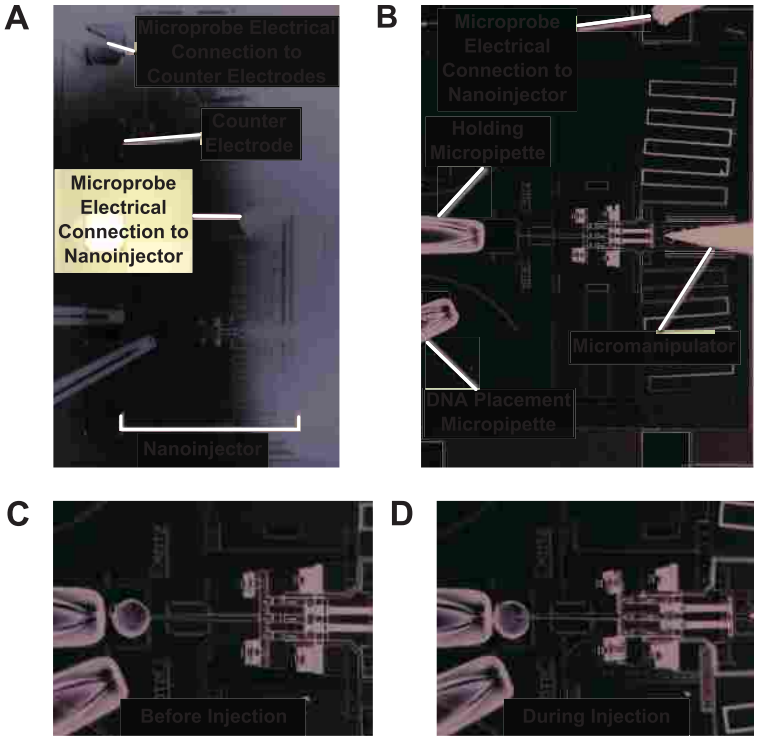

Figure 3.3: Microscopy images of the nanoinjection setup and process. (A) Optical microscopy image of the nanoinjector chip submerged in PBS. The image highlights the nanoinjectors electrical connection, and the electrical connections to the on-chip counter electrodes. The gold counter electrodes at left are electrically connected to each other through the chips monosilicon substrate. (B) A labeled image of the nanoinjector, holding micropipette, and DNA placement micropipette during injections. (C) Microscopy of a zygote placed in front of the nanoinjector before injection. (D) Microscopy of a zygot during injection. Note the small amount of deformation in the cell membrane.

to the lance. With the system operating below the decomposition voltage, very little current (2–10 μA) passes through the PBS between the nanoinjector and counter electrode.

3.3.2 Nanoinjection Does not Decrease Zygote Viability In-vitro

We conducted in-vitro experiments using zygotes harvested from CD-1 female mice and DNA coding for either an enhanced green fluorescent protein transgene driven by a ubiquitously expressing chicken β-actin promoter (CAG-EGFP, 3018bp) or a red fluorescent protein monomer transgene with the same promoter (CAG-RFPmonomer, 2976bp). These culture studies compared 24-hour survival of nanoinjected zygotes to survival of untreated zygotes which were not subjected

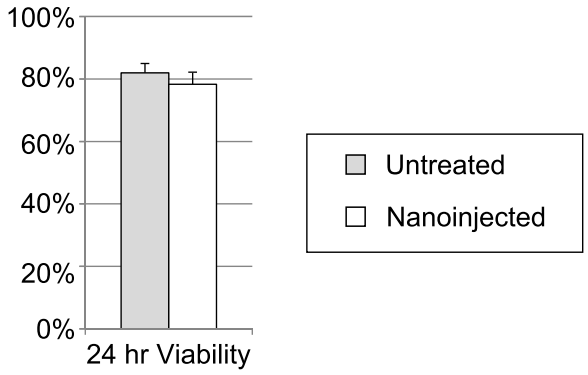

Figure 3.4: Bar graphs showing the proportion of untreated (299/363) and nanoinjected (559/713) zygotes developing to the two-cell stage. The difference in the viability of untreated and nanoinjected zygotes is not statistically significant. Plotted confidence intervals are Agresti-Coull 95% confidence intervals for binomial proportions [109].

to any type of injection or manipulation. We performed each nanoinjection as described previously, and additional detail on the protocol is provided in the Appendix A.

Figure 3.3 shows the arrangement of microprobes and micropipettes used during nanoinjection. Tungsten-tipped microprobes provided electrical connections to the nanoinjector and counter electrodes (Figure 3.3A). A glass micropipette attached to a syringe pump placed DNA into the media surrounding the lance (Figure 3.3B). The electrical connection microprobes and the DNA placement micropipette remained stationary throughout the injections. A glass micropipette on a 3-axis micromanipulator positioned the mouse zygotes for nanoinjection (Figure 3.3B, C, D) and a tungsten-tipped microprobe provided linear actuation of the nanoinjector (Figure 3.3B, D). The operator placed zygotes onto the chip in groups of 10–30 using a mouth-operated glass micropipette. The zygotes remained on the nanoinjector chip for up to 30 minutes.

There was no statistical difference between the two-cell development rates for untreated and nanoinjected mouse zygotes (Figure 3.4, and Table A.1). These in-vitro results demonstrate that the insertion of the electrically-charged, DNA-coated silicon lance into a zygote's pronucleus does not significantly damage the cellular membranes or otherwise decrease the zygote's viability. Additionally, these results suggest that the injection conditions (i.e. room temperature PBS) did not have a significant effect on zygotic viability.

3.3.3 Nanoinjection Generates Transgenic Mice with High In-vitro and Gestational Viability

To demonstrate live pup births and transgene integration following pronuclear nanoinjection, we performed side-by-side nanoinjection and pronuclear microinjection of CAG-EGFP into mouse zygotes. We performed four experimental replicates of side-by side nanoinjection and microinjection, and we collected data on zygotic viability, pup birth, gene integration, and gene expression rates (see Table A.3). Per experimental day, we harvested a minimum of 200 healthy zygotes from C57Bl/6J x CBA/J F1 females and divided them between one nanoinjection technician and two microinjection technicians at an experienced transgenic mouse facility (the University of Utah Transgenic and Gene Targeting Mouse Core). Nanoinjection followed the protocol outlined above, and pronuclear microinjection followed standard microinjection procedures (see Appendix A), with both methods using the same DNA source.

The microinjection technicians cultured all the injected zygotes overnight, counted the resulting two-cell embryos (Figure 3.5A), and then transferred them into pseudo-pregnant females. We also cultured a small number of untreated zygotes overnight on day three to estimate the in-vitro viability of the as-harvested zygotes (Figure 3.5A). After pups' birth (Figure 3.5B, C) and weaning, we collected genotypic data by polymerase chain reaction (PCR) of DNA from tail snips (Figure 3.6A, Figure A.2), and we verified that the resulting PCR product had the expected sequence (Figure A.3). We collected transgene expression data by flow cytometry of blood (Figure 3.6B), peritoneal exudates, homogenized thigh muscle, homogenized gut, and homogenized brain.

Nanoinjection and microinjection both produced pups with integrated transgenic DNA during each of the four experimental replicates. As expected in transgenic mouse production, pups with integrated DNA expressed the transgene at various levels of intensity (see, for example, Figure A.4) and some did not express at all.

Examining the viability data, we found no significant difference between the rate of zygote survival for untreated and nanoinjected embryos (Figure 3.5A). However, we found significant differences between microinjection's and nanoinjection's rates of zygote survival and between their rates of gestational success. Figure 3.5A demonstrates that more zygotes subjected to nanoinjection proceeded to the two-cell stage of development than did microinjected positive control

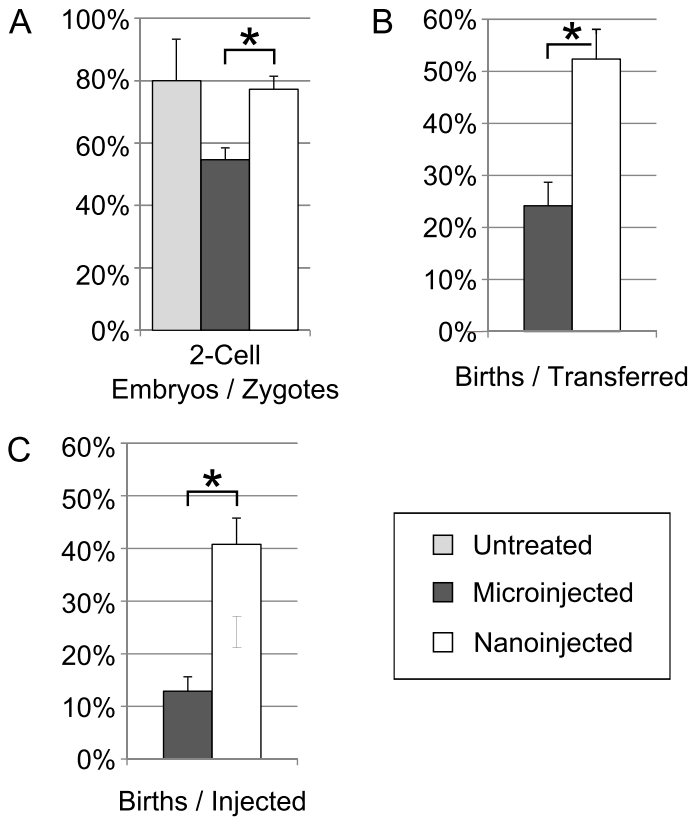

Figure 3.5: Bar charts showing in-vitro and gestational viability of microinjected and nanoinjected embryos. (A) The proportion of untreated (26/31), microinjected (351/642), and nanoinjected (288/371) zygotes developing to the two-cell stage. (B) The proportion of pups born out of two-cell embryos transferred to surrogate females for microinjected (81/339) and nanoinjected (151/288) embryos. (C) The proportion of pups born out of zygotes microinjected (81/713) and nanoinjected (151/371). Plotted confidence intervals are Agresti-Coull 95% confidence intervals for binomial proportions [109]. *The differences between indicated proportions are statistically significant ($p < 0.001$). Tabulated results are given in Table A.2.

zygotes. The odds that an injected zygote will develop to the two-cell stage are 2.8 times higher for nanoinjection than the microinjection control. When comparing the gestational success of two-cell embryos transferred into surrogate female mice, nanoinjected embryos again exhibit a higher proportion of live pups born (Figure 3.5B). The odds of gestational success for each embryo transferred are 3.5 times higher in nanoinjected embryos than in microinjected positive control embryos irrespective of the in-vitro viability rate observed between injection and the two-cell stage. Factoring in both the initial zygote survival and the gestational viability, the odds that an injected zygote will develop into a pup are 4.8 times higher with nanoinjection than with the microinjection positive control (Figure 3.5C).

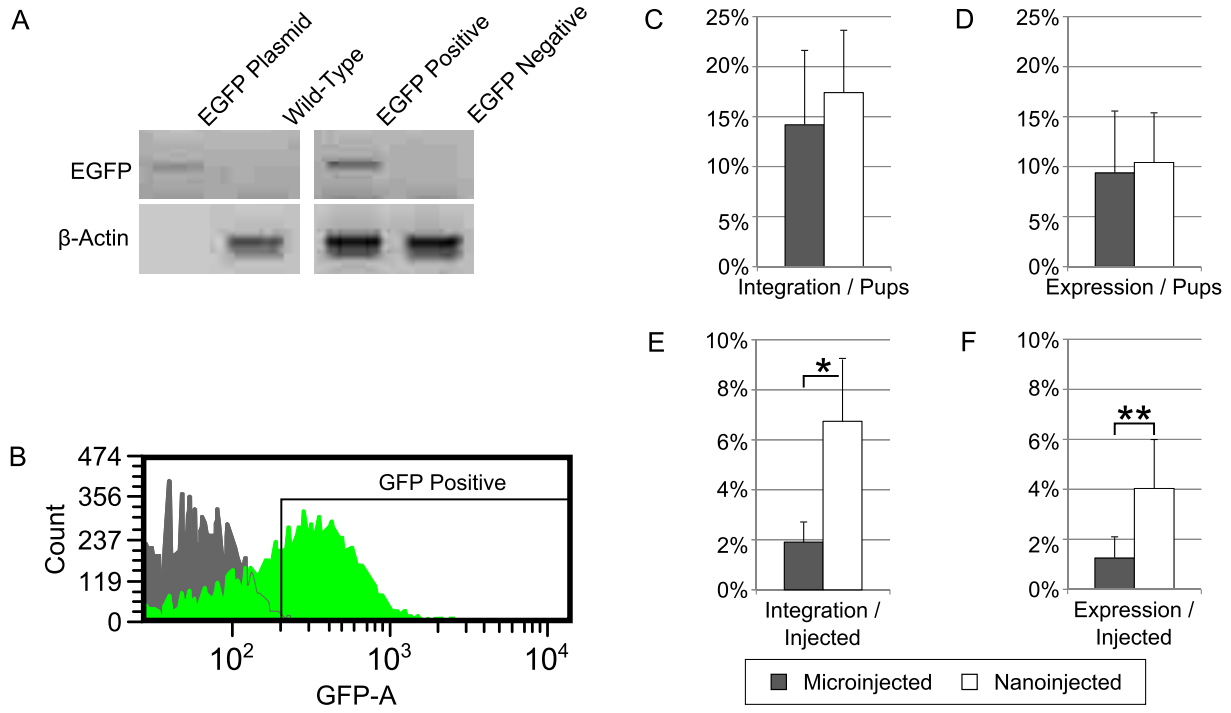

Figure 3.6: EGFP transgene integration and expression results for microinjected and nanoinjected zygotes. (A) PCR for EGFP was used to determine whether transgene integration occurred in pups, and PCR for β-actin served as a quality control for DNA extracted from tail snips. (B) Flow cytometry of blood samples was used to determine whether the integrated transgene could express EGFP. A GFP negative sample is shown in gray; a GFP positive sample is shown in green. (C) and (D) When comparing the percentage of pups with transgene integration or expression, the integration rate was not statistically different between microinjection and nanoinjection. (E) and (F) However, when compared to the total injections performed, nanoinjection resulted in a significantly higher percentage of integrated as well as expressing transgenic mice. Plotted confidence intervals are Agresti-Coull 95% confidence intervals for binomial proportions [109]. *The difference between the indicated proportions is statistically significant ($p < 0.001$). **The difference between the indicated proportions is statistically significant ($p < 0.01$). Tabulated results are given in Table A.2.

Comparing transgene integration in pups born in the nanoinjection group with pups in the microinjection positive control group, we found that the rate of transgene integration was not significantly different between the two processes (Figure 3.6C, D). Similarity between integration and expression rates among the pups born is not surprising because both processes rely on the same mechanisms of random gene integration once sufficient transgene copies are delivered to the zygote's pronucleus [46]. This similarity in rates also suggests that nanoinjection's non-fluidic,

electro-physical method of injection delivers the transgene copies to the pronucleus with similar efficiency as microinjection's fluidic delivery method.

The differences between the two processes are apparent when taking into account the influence of survival rates on the overall integration and expression success rates (Figure 3.6E, F). The higher viability of nanoinjected zygotes led to nanoinjection having statistically higher overall transgene integration rates (Figure 3.6D). The odds of an injected zygote developing into a pup carrying the transgene is 4.2 times higher for nanoinjection than the microinjection positive control. Thus, fewer egg donor females, zygotes, pseudo-pregnant females, and injection procedures were required to generate each transgenic mouse using nanoinjection.

3.4 Conclusions and Recommendations

Nanoinjection is a revolutionary method for direct transgene delivery into the pronucleus of mouse zygotes. We have demonstrated the use of a surface-micromachined MEMS as the functional unit for electro-physical delivery of DNA without injecting extracellular fluid or employing disruptive electric fields. In-vitro studies demonstrated that inserting the positively charged lance into the pronucleus and reversing the polarity does not have a statistically significant impact on the viability of nanoinjected embryos as compared to non-injected control embryos. Furthermore, the nanoinjector delivered sufficient transgene copies to the pronucleus to have similar proportions of integrated and expressing pups as microinjection, but with significantly higher zygote survival and gestational success. Hence, nanoinjection required fewer total laboratory animals and zygote manipulations per successful transgenic mouse than microinjection.

Having demonstrated the feasibility of nanoinjection, future work may aim to optimize and more fully characterize the process. For example, optimization of DNA concentrations, lance voltages, release times, and other operating parameters may allow for control over, or estimation of, the number of transgene copies delivered to the pronucleus. Additionally, the nanoinjection process may prove useful for the delivery of much smaller genetic constructs, such as siRNA, much larger genetic constructs, such as yeast artificial chromosomes, or other charged macromolecules. Nanoinjection presents a new approach to charged macro-molecule delivery with the potential to positively influence the production of transgenic animals in numerous fields.

CHAPTER 4. A NUMERICAL METHOD FOR POSITION ANALYSIS OF COMPLIANT MECHANISMS WITH MORE DEGREES OF FREEDOM THAN INPUTS

An under-actuated or underconstrained compliant mechanism may have a determined equilibrium position because its energy storage elements cause a position of local minimum potential energy. The minimization of potential energy (MinPE) method is a numerical approach to finding the equilibrium position of compliant mechanisms with more degrees of freedom (DOF) than inputs. Given the pseudo-rigid-body model of a compliant mechanism, the MinPE method finds the equilibrium position by solving a constrained optimization problem: minimize the potential energy stored in the mechanism, subject to the mechanism's vector loop equation(s) being equal to zero. The MinPE method agrees with the method of virtual work for position and force determination for under-actuated 1-DOF and 2-DOF pseudo-rigid-body models. Experimental force-deflection data is presented for a fully compliant constant-force mechanism. Because the mechanism's behavior is not adequately modeled using a 1-DOF pseudo-rigid-body model, a 13-DOF pseudo-rigid-body model is developed and solved using the MinPE method. The MinPE solution is shown to agree well with non-linear finite element analysis and experimental force-displacement data.[1]

4.1 Introduction

This paper presents a numerical method for analyzing pseudo-rigid-body models (PRBM) [2], [118], [119] of compliant mechanisms with more degrees of freedom (DOF) than inputs based on the minimization of potential energy stored in the PRBM's pseudo springs. Unlike a rigid-link mechanism, a compliant mechanism with more degrees of freedom (DOF) than inputs may have a local equilibrium position because the mechanism will tend to the position where the overall potential energy stored in its flexible elements is at a local minimum.

[1]This chapter has been accepted for publication in *ASME Journal of Mechanical Design* with Shannon Zirbel, Brian Jensen, and Larry Howell contributing as co-authors.

Mechanisms with more degrees of freedom than inputs can be referred to either as underactuated mechanisms or underconstrained mechanisms, depending on if the mechanism's degrees of freedom are intended or parasitic. Underactuated mechanisms are mechanisms with more intended (purposefully designed) DOFs than inputs [120], [121]. The simplest underactuated mechanism is a 1-DOF mechanism given zero inputs. More commonly underactuated mechanisms are multiple-degree-of-freedom (MDOF) mechanisms [122]–[124] intentionally given fewer inputs than DOF during operation.

Underconstrained mechanisms have undesired or parasitic [125] degrees of freedom which are neither constrained nor actuated [126]. Consider, for example, a hypothetical planar, partially compliant mechanism with one intended DOF. This hypothetical mechanism contains a single compliant revolute joint which may also extend or compress under certain loading conditions. The most accurate PRBM for such a joint would be a prismatic-revolute joint having two degrees of freedom, giving the mechanism two total DOF. Given a single input, the mechanism's 2-DOF PRBM is underconstrained, with the parasitic DOF unspecified. Underconstrained PRBMs are useful for analyzing 1-DOF compliant mechanisms, which are more accurately modeled with a MDOF PRBM [127]–[129]

Underactuated and underconstrained compliant mechanisms can be analyzed analytically using energy methods, such as the method of virtual work [2], [128], [130] or inverse static analysis [124], [127]. Finite element analysis (FEA) can also be used to find the equilibrium position of MDOF compliant mechanisms [122], [131].

Analytical methods such as virtual work, inverse static analysis and others may require significant mathematical manipulation prior to numerically calculating the solution. For example, the method of virtual work requires analytical computation of kinematic coefficients and nDOF simultaneous equations. For one, two, or three DOF, this mathematical effort is reasonable; however, with additional DOF, the method of virtual work becomes quite cumbersome.

In a broad sense, all of these methods obtain the equilibrium position of an underactuated or underconstrained compliant mechanism by finding the minimum potential energy state of the mechanism such that the mechanism remains assembled (e.g. the loop closure equations are satisfied). The concept of using constrained optimization techniques to find the minimum potential energy of a system is well reported in the literature. For example, various optimization algorithms

have been applied to minimizing potential energy in models of molecular [132], [133] and atomic interactions [134]. The literature does not report, however, optimization based methods for finding the equilibrium position of an underactuated or underconstrained mechanism's PRBM.

The minimization of potential energy (MinPE) method presented in this paper formulates underactuated or underconstrained mechanism analysis as a concise constrained optimization problem. The total potential energy stored in the pseudo-springs of the compliant mechanism's PRBM is minimized subject to the vector loop equations being satisfied. The analysis of the mechanism is reduced to one equation for potential energy and two equations per vector loop regardless of the number of degrees of freedom. These equations can be quickly stated from the PRBM itself without further manipulation. In the examples presented here, the MinPE problem is solved by a sequential quadratic programming algorithm. Other established algorithms which accommodate non-linear constraints could also be used.

In its current formulation, the MinPE method solves for the equilibrium position of displacement loaded mechanisms. Three examples of displacement loaded, underactuated mechanisms are presented. The first and second examples are comparisons of the MinPE method with the method of virtual work for underactuated 1-DOF and 2-DOF mechanisms. In the third example, a prototype fully compliant constant-force mechanism is shown to be inadequately modeled with a 1-DOF PRBM, but accurately modeled by an underconstrained 13-DOF PRBM solved using the MinPE method. The results of the 1-DOF and 13-DOF models are compared with non-linear FEA and experimental results.

4.2 Minimization of Potential Energy (MinPE) Method

The MinPE method for a PRBM of a compliant mechanism can be stated formally as

$$\text{minimize} \qquad PE(x_1, x_2 \ldots x_n) \tag{4.1}$$

$$\text{subject to} \qquad \vec{Z}(x_1, x_2 \ldots x_n) = 0 \tag{4.2}$$

where $PE(x_1, x_2 \ldots x_n)$ is the potential energy stored in the mechanism as a function of the position variables $x_1, x_2 \ldots x_n$, and $\vec{Z}(x_1, x_2 \ldots x_n)$ is the vector loop equation(s). The number of independent energy storage elements must be greater than or equal to the DOF for the MinPE method

to converge to an underactuated mechanism's local equilibrium position. Consider for example, a 2-DOF mechanism with one independent energy storage element. Fixing the position of that energy storage element leaves one unspecified degree of freedom that can vary without changing the mechanism's potential energy.

When applied to a single loop PRBM with linear pseudo-spring constants, the MinPE method can be stated as

$$\text{minimize} \qquad \frac{1}{2}\sum_{i=1}^{n} k_i \delta_i^2 \tag{4.3}$$

$$\text{subject to} \qquad \sum_{j=1}^{m} r_j \cos(\theta_j) = 0 \tag{4.4}$$

$$\sum_{j=1}^{m} r_j \sin(\theta_j) = 0 \tag{4.5}$$

where k_i is the PRBM spring constant for the i^{th} pseudo-spring, δ_i is the relative displacement of that energy storage element, r_j is the length of the j^{th} PRBM link, and θ_j is the angle of the j^{th} PRBM link measured from the horizontal. In the PRBM's presented in this paper, r_j may be variable, k_i will be either be a torsional or linear spring constant, and δ_i will be a relative angular or linear displacement.

Solution of the optimization problem stated in Eqs. (4.3)–(4.5) gives the unknown position variables. Given the mechanism's position, the input and reaction forces can be found through a static (free body diagram) analysis of links within the mechanism.

This MinPE optimization problem can be solved using established constrained optimization methods. The MinPE optimization problems presented in this paper were solved using a sequential quadratic programming (SQP) algorithm (MATLAB fmincon function). An SQP algorithm was chosen for its relative speed, and ease of implementation. However, the SQP algorithm was used with the understanding that the algorithm only finds local, not necessarily global, minima, and that the minimum found depends heavily on initial guess. The 13-DOF mechanism in Section 4.4 presents an example of how initial guesses can be selected to converge to avoid unrealistic local minima. Additionally, lower and upper bounds on the optimized variables can be used to restrict the MinPE solution to a particular configuration of the mechanism when multiple equivalent configurations exist; Section 4.3.2 presents such a mechanism.

Analyses may exist where the goal is to find a non-obvious global potential energy minimum. This could occur, for example, when a compliant mechanism with many DOF is assembled with its energy storage elements under a preload. In such a mechanism, many potential energy local minima may exist. To find the global potential energy minimum, multiple initial guesses could be employed in a gradient based algorithm, or global optimization methods such as those in [132]–[134].

4.3 Comparison with the Method of Virtual Work

The MinPE method is similar to the method of virtual work, in that both are energy analysis methods seeking the lowest potential energy of the mechanism. Virtual work's analytical steps result in a system of nDOF non-linear equations, which must be solved numerically to obtain the theoretically exact solution. The MinPE method, on the other hand, proceeds directly to a numerical solution. A comparison of the relative mathematical effort and results of the two methods are presented for two examples below.

4.3.1 1-DOF Underactuated Mechanism

A non-trivial case of an underactuated 1-DOF compliant mechanism occurs when (1) there is no position where all compliant elements in the mechanism are undeflected (i.e. some flexible elements are deformed to assemble the mechanism), and (2) the mechanism is given no input. When unactuated, such a mechanism has an equilibrium position which is not necessarily apparent from the link geometries alone.

Table 4.1: Pseudo-rigid-body model parameters for the crank slider shown in Figure 4.1. Link lengths (r) are in inches, spring constants (k) are in inch-pounds/radian, and angles θ are in radians.

Parameter	r_2	r_3	k_1	k_2	$\theta_{2\circ}$	$\theta_{3\circ}$
Value	16.6	8.3	16.46	49.39	$\pi/2$	0

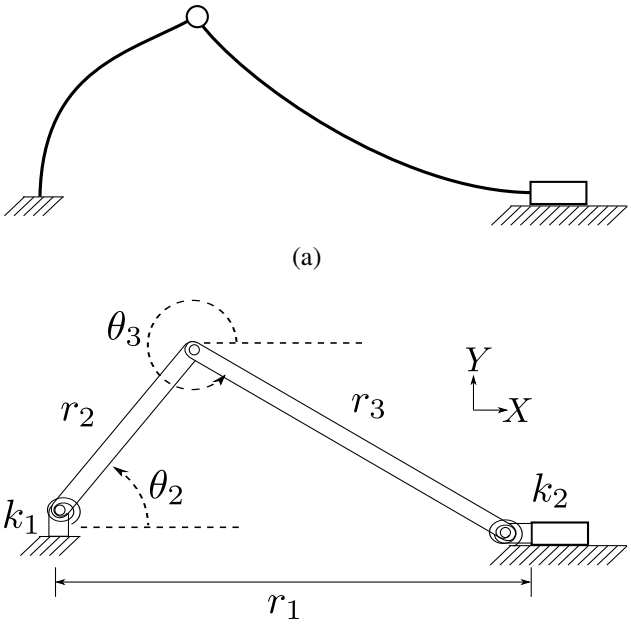

Figure 4.1: (a) An example underactuated single degree of freedom mechanism, and (b) its pseudo-rigid-body model.

Figure 4.1 shows a compliant crank-slider based on an example in [2]. In this mechanism, member r_2 is undeflected at $\theta_{2\circ} = \pi/2$ rad and member r_3 is undeflected at $\theta_{3\circ} = 0$ rad. The PRBM parameters are given in Table 4.1.

Using the method of virtual work, and taking r_1 as the generalized coordinate, nDOF $= 1$ non-linear equation can be found that describes the crank slider's equilibrium position.

$$\frac{r_2\cos(\theta_2)}{r_3\cos(\theta_3)}k_3(\theta_3-\theta_{3\circ})-k_2(\theta_2-\theta_{2\circ})=0 \tag{4.6}$$

where the values of θ_3 and r_1 are found by the kinematic relationships

$$\theta_3 = \arcsin(-\frac{r_2}{r_3}\sin(\theta_2)) \tag{4.7}$$

$$r_1 = r_2\cos(\theta_2)+r_3\cos(\theta_3) \tag{4.8}$$

The MinPE method solves for the crank slider's equilibrium position by minimizing the potential energy stored in the two pseudo-rigid torsional springs, subject to the equality constraints

of the x and y components of the vector loop being equal to zero

$$\min \qquad \frac{1}{2}\left(k_1(\theta_2-\theta_{2\circ})^2+k_2(\theta_3-\theta_{3\circ})^2\right) \tag{4.9}$$

$$\text{subject to} \qquad r_2\cos(\theta_2)+r_3\cos(\theta_3)-r_1=0 \tag{4.10}$$

$$r_2\sin(\theta_2)+r_3\sin(\theta_3)=0 \tag{4.11}$$

where r_1, θ_2 and θ_3 are optimized variables. No additional kinematic relationships need to be derived from the vector loop equations to find the dependent variables r_1 and θ_3. The initial guess, lower bounds, and upper bounds are given in Table 4.2.

The equilibrium positions predicted by both methods are given in Table 4.3. The two methods give essentially the same prediction for the mechanism's equilibrium position. The slight difference in the two answers can be attributed to truncation and round-off errors inherent in the numerical solution of Eq. (4.6) and the evaluation of Eqs. (4.9)–(4.11).

4.3.2 2-DOF Underactuated Mechanism

Figure 4.2 shows an example PRBM of a 2-DOF compliant triple slider and Table 4.4 gives the model parameters. Like a double slider, link lengths r_2 and r_1 are variable. Additionally, link r_3 is a compliant member with a linear spring constant k_1, and there is a spring of stiffness k_2 colinear with link r_1. The undeflected lengths of link r_3 and spring k_2 are $r_{3\circ}$ and $l_{s\circ}$, respectively. Given a single input at r_2, the mechanism is underactuated, with one DOF unspecified.

Table 4.2: Initial guess, lower bounds, and upper bounds for the MinPE analysis of the crank slider shown in Figure 4.1. Link lengths (r) are in inches, and angles θ are in radians.

	r_1	θ_2	θ_3
Initial Guess	15	0	$-\pi/2$
Lower Bound	0	π	$\pi/2$
Upper Bound	24.9	0.4	-0.6

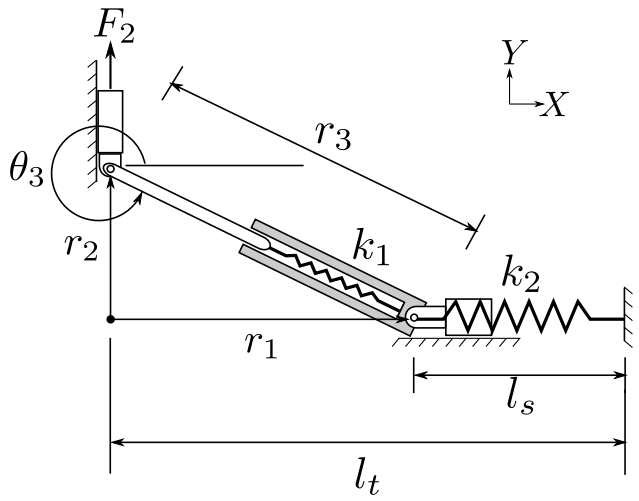

Figure 4.2: An example underactuated 2-DOF compliant mechanism. The length of r_2 is specified, leaving one DOF unspecified.

Taking r_3 and r_2 as the generalized coordinates the method of virtual work requires the derivation of nDOF $= 2$ simultaneous non-linear equations to give

$$F_2 + \tan(\theta_3) k_2 (l_t - r_1 - l_{s\circ}) = 0 \tag{4.12}$$

$$k_1 (r_3 - r_{3\circ}) - \frac{1}{\cos(\theta_3)} - k_2 (l_t - r_1 - l_{s\circ}) = 0 \tag{4.13}$$

where the following kinematic relationships must be substituted (or calculated) prior to solving Eqs. (4.12) and (4.13).

$$r_3 = \frac{-r_2}{\sin(\theta_3)} \tag{4.14}$$

$$r_1 = r_3 \cos(\theta_3) \tag{4.15}$$

Table 4.3: Comparison of predicted equilibrium positions for the 1-DOF mechanism pictured in Figure 4.1. Link lengths (r) are in inches, and angles θ are in radians.

	Virtual Work	**MinPE**	**Difference**
$r1$	24.5531	24.5531	1.580×10^{-8}
θ_2	0.1177	0.1177	2.107×10^{-9}
θ_3	-0.2371	-0.23717	4.350×10^{-9}

The solution of these two equations will give the equilibrium position of the mechanism and the input force F_2 for a given length of r_2.

Given a value of r_2, the MinPE methods finds the equilibrium position of the mechanism by solving

$$\text{minimize} \qquad \frac{1}{2}\left(k_1(r_3 - r_{3\circ})^2 + k_2(l_t - r_1 - l_{s\circ})^2\right) \tag{4.16}$$

$$\text{subject to} \qquad r_3\cos(\theta_3) - r_1 = 0 \tag{4.17}$$

$$r_2 + r_3\sin(\theta_3) = 0 \tag{4.18}$$

where r_1, r_3, and θ_3 are the optimized variables. The value of the input force F_2 is found by applying static equilibrium in the Y direction to link r_3 to give

$$F_2 = -k_1(r_3 - r_{3\circ})\sin(\theta_3) \tag{4.19}$$

Again, the MinPE method does not require the separate calculation of kinematic relationships, since these conditions are implicit in the vector loop constraint equations (4.17) and (4.18). The initial guess, lower bounds, and upper bounds given in Table 4.5 were the same for each point evaluated. The mechanism has two equivalent, symmetric configurations: one with θ_3 in the fourth quadrant (as shown in Figure 4.2) and one with θ_3 in the first quadrant. The lower and upper bounds on the angle θ_3 given in Table 4.5 restrict the MinPE method to the configuration with θ_3 in the fourth quadrant.

As shown in Figure 4.3, the virtual work and the MinPE analysis of the triple-slider give the same results for the unknown parameters θ_3, r_3, r_1, and F_{in}. The maximum absolute differences

Table 4.4: Geometric constants, undeflected link and spring lengths, and spring constants corresponding to the model shown in Figure 4.2. Lengths (l & r) are cm, spring constants (k) are N/cm.

Parameter	l_t	$l_{s\circ}$	$r_{3\circ}$	k_1	k_2
Value	10	3	10	1	3

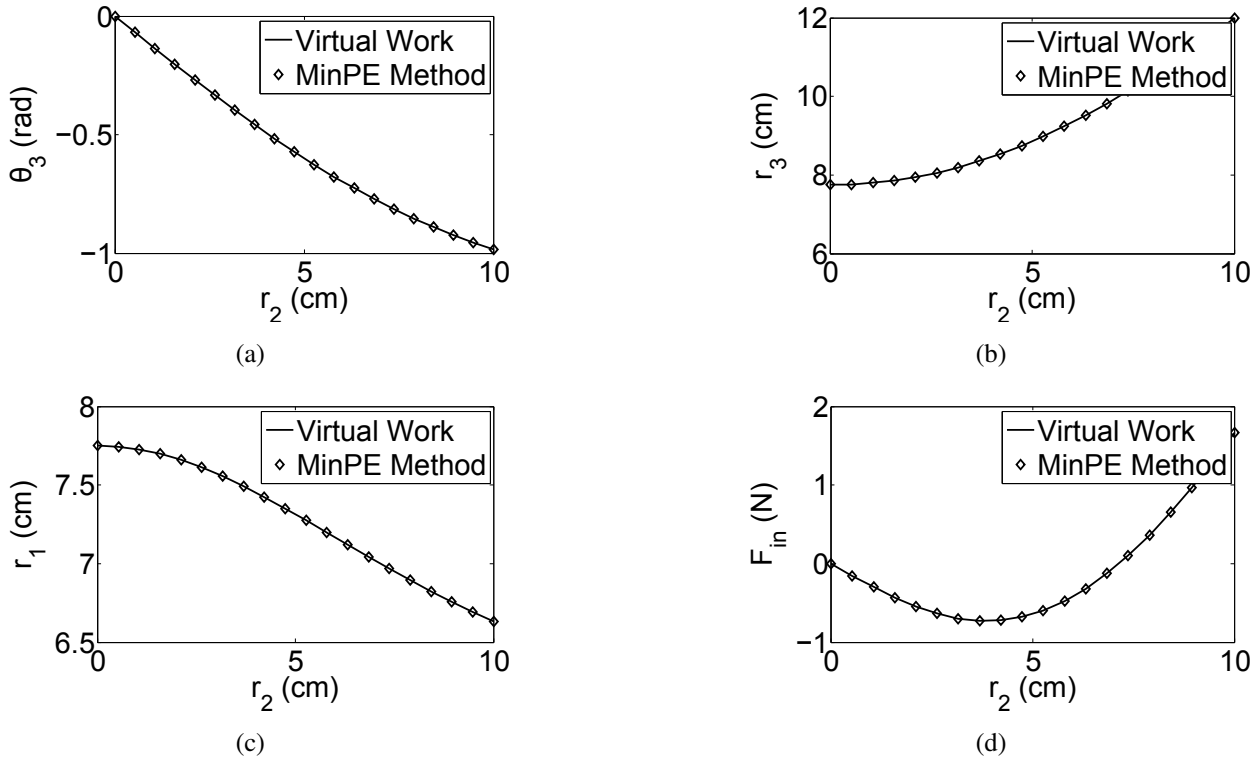

Figure 4.3: Comparison of virtual work analysis and MinPE analysis of a 2-DOF triple-slider mechanism shown in Figure 4.2. Both models were given a single input of r_2 and solved for θ_3, r_3, r_1, and F_{in}.

between the two methods given in Table 4.6 are likely due to truncation and round-off errors inherent in the numerical evaluation of both methods.

Table 4.5: Initial guess, lower bounds, and upper bounds for the MinPE analysis of the 2-DOF slider mechanism shown in Figure 4.2. Link lengths (r) are in inches, and angles θ are in radians.

	θ_3	r_2	r_3
Initial Guess	-0.3	8	7.5
Lower Bound	$-\pi/2$	1×10^{-4}	1×10^{-4}
Upper Bound	0	15	15

4.4 Comparison of the MinPE Method, non-linear FEA and Experimental Results in a 13-DOF Underconstrained PRBM

The following example considers an intended 1-DOF compliant mechanism which is not adequately represented by a 1-DOF model due to unintended, or parasitic, motion in its compliant elements. In this case, parasitic motion is caused by non-ideal loading of the mechanism's compliant elements. A more complete PRBM of the mechanism which accounts for these non-ideal loading conditions results in a much more accurate but underconstrained, MDOF representation of the intended 1-DOF mechanism.

The intended 1-DOF compliant mechanism described below is a fully compliant, lamina-emergent, constant-force mechanism. Constant-force mechanisms are mechanisms which have a virtually constant input force through a majority of their motion [135], and can be considered statically balanced [136], [137] through the constant-force portion of their deflection. Lamina emergent mechanisms (LEMs) are fabricated from one or more planar layers of material (lamina) and have significant components of motion normal to the fabrication plane [3], [138].

The constant-force LEM achieves its motion through the deflection of lamina emergent torsional (LET) joints [139]. Figure 4.4 shows a symmetric LET joint consisting of four torsional members and two bending members. Under a pure moment load, the LET joint does not experience extension or compression and can be accurately modeled as a 1-DOF pseudo-rigid torsional hinge. In the 1-DOF representation of the LET joint shown in Figure 4.5, the equivalent stiffness of the joint is found by first computing the stiffness of the torsional elements (k_t) and the bending

Table 4.6: Maximum absolute differences between the virtual work analysis and (MinPE) analysis of the compliant 2-DOF mechanism shown in Figure 4.2 for an input range of $r_2 = 0.01$ cm to $r_2 = 10$ cm.

Parameter	**Max Difference**
θ_3	5.08×10^{-9} rad
r_3	8.68×10^{-8} cm
r_1	8.70×10^{-8} cm
F_2	4.12×10^{-8} N

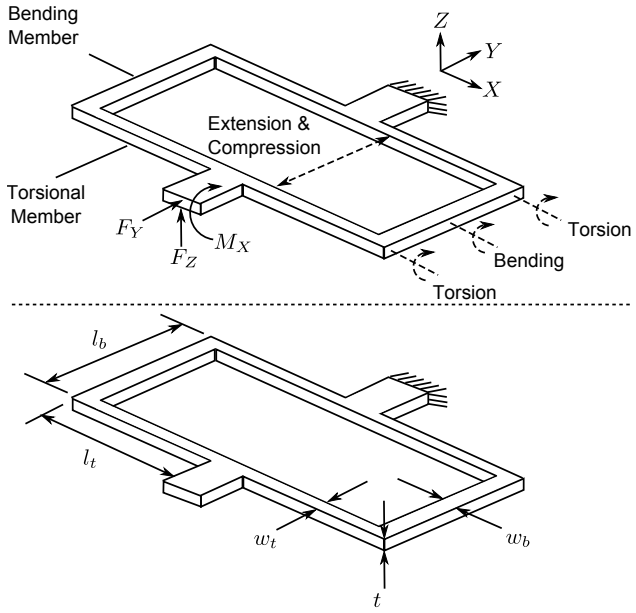

Figure 4.4: Schematic representation of a lamina-emergent torsional (LET) joint showing critical dimensions, the intended torsional and bending deflections about the X axis, and the parasitic extension or compression in the Y direction.

elements (k_b) [139] as

$$k_t = \frac{Gw_t t^3}{l_t}\left[\frac{1}{3} - 0.21\frac{t}{w_t}\left(\frac{1-t^4}{12w_t^4}\right)\right] \tag{4.20}$$

$$k_b = \frac{Ew_b t^3}{12l_b} \tag{4.21}$$

where E is Young's Modulus, G is the modulus of rigidity, and w_t, w_b, l_t, l_b, t are as defined in Figure 4.4. If the joint is symmetric about lines parallel to the X and Y axes, k_t and k_b can be combined in a single equivalent torsional spring with stiffness k_{eq}.

$$k_{eq} = \frac{2k_t^2 k_b}{k_t^2 + 2k_t k_b} \tag{4.22}$$

However, given forces in the Y direction, the torsional members also act as fixed-guided beams in the XY plane, extending or compressing the LET joint along the Y direction [139]. This parasitic motion can significantly impact the performance of a mechanism employing the LET joint, but is not accounted for in the LET joint's 1-DOF PRBM.

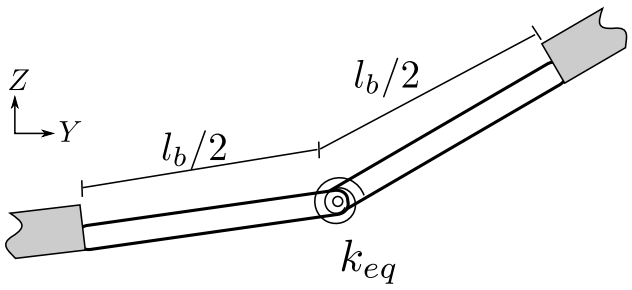

Figure 4.5: A 1-DOF pseudo-rigid-body model of the lamina emergent torsional (LET) joint modeling only rotation about a single axis.

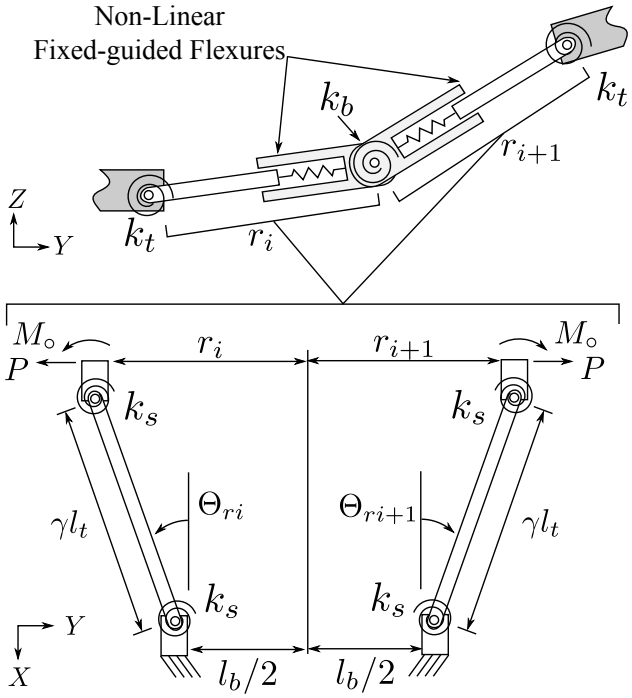

Figure 4.6: A 5-DOF pseudo-rigid-body model of the lamina emergent torsional (LET) joint which models three rotations and two translations.

Figure 4.6 shows a 5-DOF PRBM of the LET joint which accounts for its parasitic extension and compression. The 5-DOF LET PRBM has three rotational degrees of freedom accounting for the intended torsional and bending displacements, and two degrees of freedom accounting for the parasitic extension or compression of the LET joint's torsional members.

The stiffness of the torsional members k_t are found using Eq. (4.20), and the stiffness of the bending members are found using Eq. (4.21). The stiffness of the fixed-guided pseudo-rigid

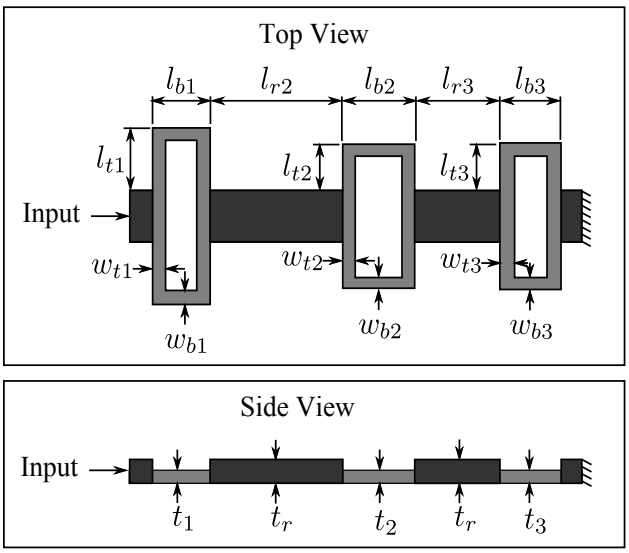

Figure 4.7: Dimensioned schematic of the fully compliant, lamina-emergent constant-force mechanism.

springs k_s is found using the PRBM of a fixed-guided beam [2] as shown in Figure 4.6

$$k_s = \left(\frac{E\gamma K_\Theta w_t t^3}{6 l_t} \right) \tag{4.23}$$

where $\gamma = 0.8517$ and $K_\Theta = 2.67617$. Considering the left fixed-guided beam, the angular displacement, Θ_{ri}, experienced by the pseudo-rigid springs is related to the length of the link r_i by

$$\Theta_{ri} = \arcsin\left(\frac{r_i - l_b/2}{l_t \gamma} \right) \tag{4.24}$$

The fully compliant constant-force LEM shown in Figures 4.7 and 4.8 contains three LET joints. When actuated as pictured in Figure 4.8(b), the mechanism emerges from the fabrication plane and gives a nearly constant input force through a large portion of its motion.

The constant-force LEM was modeled using the 1-DOF PRBM of the LET joint, the 5-DOF PRBM of the LET joint, and non-linear solid finite element analysis. These models are described next and their force-deflection predictions are then compared to an experimentally collected force-displacement curve for the physical prototype pictured in Figure 4.8.

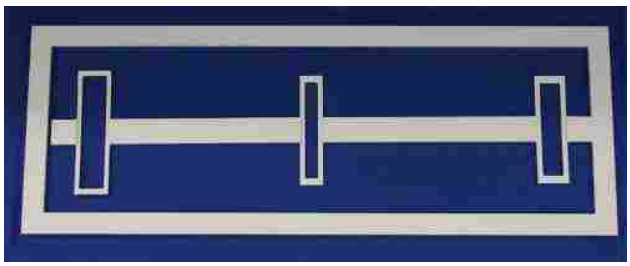

(a) As-fabricated position

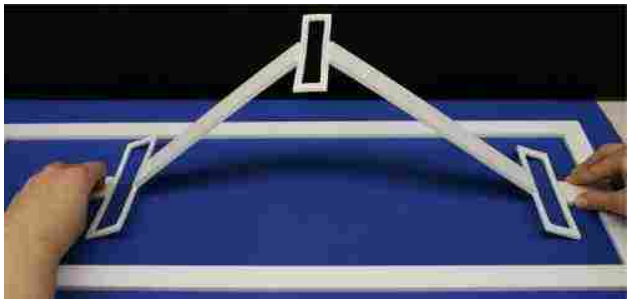

(b) Deflected position

Figure 4.8: A polypropylene constant-force lamina emergent mechanism in its as-fabricated and deflected positions.

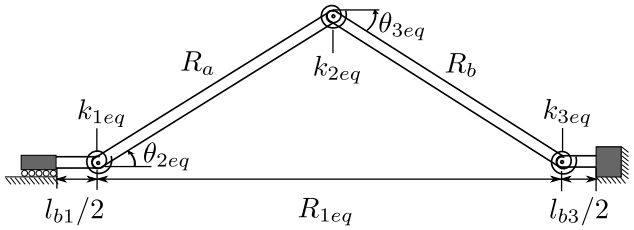

Figure 4.9: A 1-DOF pseudo-rigid-body crank-slider model of the lamina-emergent constant-force mechanism shown in Figure 4.7 based on the 1-DOF model of the lamina emergent torsional (LET) joint shown in Figure 4.5.

4.4.1 1-DOF Constant-force LEM Model

Modeling the constant-force LEM with the 1-DOF PRBM of the LET joint results in a 1-DOF crank-slider model of the mechanism. Using the pseudo-rigid link lengths and angles pictured in Figure 4.9, the unknown angles θ_{2eq} and θ_{3eq} can be found for a given value of R_{1eq} using rigid

body kinematics

$$\theta_{2eq} = \arccos\left(\frac{R_{1eq}^2 + R_a^2 - R_b^2}{2R_{1eq}R_a}\right) \tag{4.25}$$

$$\theta_{3eq} = \arcsin\left(\frac{-R_a \sin\theta_{2eq}}{R_b}\right) \tag{4.26}$$

where the pseudo-rigid link lengths R_a and R_b are found by

$$R_a = l_{r2} + (l_{b1}/2 + l_{b2}/2) \tag{4.27}$$

$$R_b = l_{r3} + (l_{b2}/2 + l_{b3}/2) \tag{4.28}$$

With the mechanism's position determined, the input force F_{in} is found using the method of virtual work. The resulting expression for F_{in} is

$$\begin{aligned} F_{in} &= R_b \cos(\theta_{3eq}) \frac{k_{1eq}\theta_{2eq} + k_{2eq}(2\pi + \theta_{2eq} - \theta_{3eq})}{R_a R_b \sin(\theta_{2eq} - \theta_{3eq})} \\ &+ R_a \cos(\theta_{2eq}) \frac{k_{2eq}(2\pi + \theta_{2eq} - \theta_{3eq}) + k_{3eq}(2\pi - \theta_{3eq})}{R_a R_b \sin(\theta_{2eq} - \theta_{3eq})} \end{aligned} \tag{4.29}$$

Executed in MATLAB, the 1-DOF PRBM required ≈ 0.06 seconds to generate 75 mechanism positions and force-deflection points. The force deflection curve predicted by the 1-DOF model is shown in Figure 4.12 and the angle of rigid link R_a is given in Figure 4.13. The 1-DOF model under-predicts the magnitude of the input force in the constant-force portion of the force-displacement relationship. Additionally, the 1-DOF model gives no information on the non-linear

Table 4.7: Initial guess, lower bounds, and upper bounds for the MinPE analysis of the 13-DOF underactuated PRBM slider mechanism shown in Figure 4.10. The initial guess given below is for the first solved position only (1 mm input displacement), and corresponds to the as-fabricated position. All subsequent steps used the previous mechanism position as the initial guess for the next mechanism position. Link lengths (r) are in millimeters, and angles θ are in radians.

	r_2	r_3	r_4	r_5	r_6	r_7	θ_2	θ_3	θ_4	θ_5	θ_6	θ_7	θ_8	θ_9
Initial Guess	20	20	13.7	13.7	18.25	18.25	0	0	0	0	0	0	0	0
Lower Bound	0	0	0	0	0	0	0	0	0	0	$-\frac{\pi}{2}$	$-\frac{\pi}{2}$	$-\frac{\pi}{2}$	$-\frac{\pi}{2}$
Upper Bound	22	22	15.1	15.1	20.1	20.1	$\frac{\pi}{2}$	$\frac{\pi}{2}$	$\frac{\pi}{2}$	$\frac{\pi}{2}$	0	0	0	0

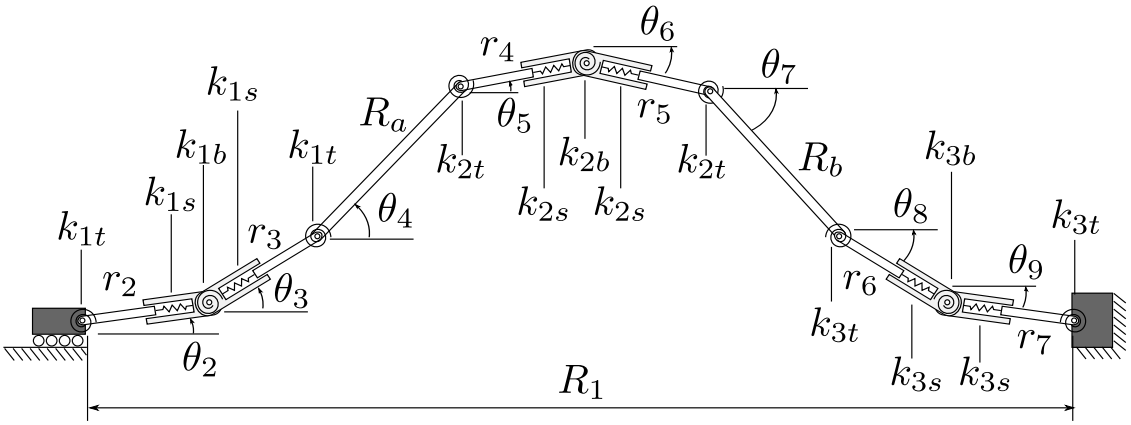

Figure 4.10: A 13-DOF pseudo-rigid-body model based on the 5-DOF model of the (LET) joint shown in Figure 4.6.

increase in input force below approximately 5 mm (Figure 4.12(b)), and over predicts the angle of link R_a as the mechanism emerges from its fabrication plane (Figure 4.13(b). This non-linearity is caused by parasitic compression of the LET joints, which is not accounted for in the 1-DOF model of the joint. Since the 1-DOF PRBM does not adequately model the mechanism's performance, a more complete model of the LEM constant-force mechanism was developed using the 5-DOF LET joint PRBM shown in Figure 4.6.

4.4.2 13-DOF Constant-force LEM Model

Accounting for the parasitic compression in the constant-force LEM's LET joints results in the more complex pseudo-rigid-body model shown in Figure 4.10. This pseudo-rigid-body model has a total of 13 DOF and one specified input R_1, leaving 12 DOF unspecified. Analyzing this mechanism using the method of virtual work would require the derivation and solution of 13 non-linear simultaneous equations, which is not done here.

When analyzing the 13-DOF mechanism by the MinPE method, only three equations are required to find the remaining 12 degrees-of-freedom: the total potential energy stored in the pseudo-rigid-body mechanism, and the *x* and *y* components of the mechanism's vector loop equa-

tion. Formally stated, the MinPE optimization problem is

$$\begin{aligned}
\text{minimize} \quad & k_{1t}(\delta_{\theta 2})^2 + 2k_{1s}\Theta_{r2}^2 + k_{1b}(\delta_{\theta 3} - \delta_{\theta 2})^2 + 2k_{1s}\Theta_{r3}^2 \\
& + k_{1t}(\delta_{\theta 4} - \delta_{\theta 3})^2 + k_{2t}(\delta_{\theta 5} - \delta_{\theta 4})^2 + 2k_{2s}\Theta_{r4}^2 \\
& + k_{2b}(\delta_{\theta 6} - \delta_{\theta 5})^2 + 2k_{2s}\Theta_{r5}^2 + k_{2t}(\delta_{\theta 7} - \delta_{\theta 6})^2 \\
& + k_{3t}(\delta_{\theta 8} - \delta_{\theta 7})^2 + 2k_{3s}\Theta_{r6}^2 + k_{3b}(\delta_{\theta 9} - \delta_{\theta 8})^2 \\
& + 2k_{3s}\Theta_{r7}^2 + k_{3t}(\delta_{\theta 9})^2 \qquad (4.30)
\end{aligned}$$

$$\begin{aligned}
\text{subject to} \quad & r_2\cos(\theta_2) + r_3\cos(\theta_3) + R_a\cos(\theta_4) + r_4\cos(\theta_5) \\
& + r_5\cos(\theta_6) + R_b\cos(\theta_7) + r_6\cos(\theta_8) \\
& r_7\cos(\theta_9) - R_1 = 0 \qquad (4.31)
\end{aligned}$$

$$\begin{aligned}
& r_2\sin(\theta_2) + r_3\sin(\theta_3) + R_a\sin(\theta_4) + r_4\sin(\theta_5) \\
& + r_5\sin(\theta_6) + R_b\sin(\theta_7) + r_6\sin(\theta_8) \\
& r_7\sin(\theta_9) = 0 \qquad (4.32)
\end{aligned}$$

where the Θ_{ri} terms are the pseudo-rigid angular displacements shown in Figure 4.6 and given by Eq. (4.24), and the k values are calculated by Eqs. (4.20), (4.21), (4.23). The relative angular displacement of the i^{th} torsional or bending pseudo-rigid spring is given by

$$\delta_{\theta i} = \theta_i - \theta_{i\circ} \qquad (4.33)$$

where θ_i is the current angular position of the pseudo-rigid spring, and $\theta_{i\circ}$ is the pseudo-rigid spring's initial position.

The input force to the mechanism is found from the parasitic deflection of link r_2.

$$F_{in} = \frac{2K_\Theta \arcsin((r_1 - l_{b1}/2)/(\gamma lt1))Ew_{t1}^3 t_1}{3l_{t1}^2} \qquad (4.34)$$

The value of R_1 is given as the input, and the optimized variables are θ_2 through θ_9, and r_2 through r_7. The mechanism's position points were found sequentially for 1 mm increments of R_1, beginning with the as-fabricated position. The lower bounds and upper bounds given in Table 4.7 were the same for each point evaluated. The 13-DOF PRBM has two equivalent, symmetric configurations: the configuration shown in Figure 4.10, and its mirror about the horizontal axis. The lower and upper bounds on the angles θ_2 through θ_9 given in Table 4.7 restrict the MinPE method to the configuration shown in Figure 4.10. The lower and upper bounds on the link lengths r_2 through r_7 were set to 100% compressed (0 length) at the lower bound, and 10% extended (110% original length) at the upper bound.

The initial guess for the first analyzed point (1 mm input displacement) was the as-fabricated position given in Table 4.7. To increase the computational efficiency of the solution routine, each subsequent step's initial guess was the previous position. For example, the position variables calculated at 3 mm input displacement were used as the initial guess for calculating of the position at 4 mm input displacement. Using an updated initial guess was $\approx 50\%$ faster than using the as-fabricated position as a constant initial guess. Both a constant and an updated initial guess converge to an identical solution.

Executed using MATLAB's fmincon function, the MinPE model solution of the 13-DOF pseudo-rigid-body model required ≈ 30 seconds to generate 75 mechanisms positions and force-deflection points. The force-displacement curve predicted by the MinPE solution of the constant-force LEM's 13-DOF pseudo-rigid-body model is plotted in Figure 4.12, and the angle of rigid link R_a is plotted in Figure 4.13.

The MinPE results agree well with the experimental results and the non-linear FEA results through the mechanism's entire range of motion, including the initial rise in force, the transition to the constant-force regime, and the magnitude of the constant force. Figures 4.12(b) and 4.13(b) give the absolute force and R_a angle error of the 13-DOF model as compared to the FEA results.

4.4.3 Finite Element Analysis

The constant-force LEM was analyzed using non-linear finite element analysis (FEA) in ANSYS 11.0. The mechanism geometry was meshed with ≈ 9000 SOLID95 quadratic (20-node) brick and tetrahedral elements, which are capable of large displacement and stress stiffening.

Quadratic bricks were used along in the LET flexures, and larger tetrahedral elements were used in the rigid segments. Solid element modeling was chosen over beam or shell element modeling because it gives a more comprehensive representation of the mechanism, especially in its post buckling state. The solid model FEA was used as a baseline for evaluating the accuracy of the 13-DOF PRBM solved using the MinPE method.

The model solved in 75 load-steps using ANSYS' static, non-linear solver. The model required ≈ 90 minutes to solve. In post processing, the simulation calculated the sum of the nodal forces acting on the input face, and the angle of rigid link R_a measured from the horizontal, given in Figures 4.12 and 4.13, respectively. The resulting force-displacement curve plotted in Figure 4.12 agrees well with the experimental force-displacement data throughout the mechanism's range of motion.

4.4.4 Physical Testing

Experimental force-displacement data was collected for the polypropylene constant-force LEM using a custom built force-displacement measurement system shown in Figure 4.11. The force output was generated by a capacitive load cell, and the displacement output was generated by a linear potentiometer. The free end of the constant-force LEM was secured to linear bearings and actuated by a linear stepper motor.

The mechanism was actuated at ≈ 4.9 mm/s, requiring a total of 15.9 seconds to cover the total travel range of the mechanism. The mechanism was actuated at this speed to approximate the quasi-static loading assumptions made by the MinPE solution and the FEA solution, while also preventing stress relaxation in the polypropylene during actuation.

The linear bearings prevented undesired motions and prevented moments from being transferred to the load cell. However, one or more imperfect bearings, or friction in at least one of the bearings introduced oscillating scatter into the constant force portion of the curve. The true force-displacement curve can be assumed to lie within this scatter.

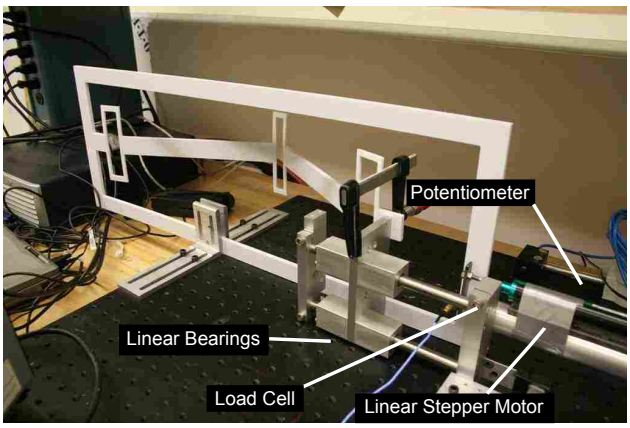

Figure 4.11: Labeled photograph of the constant-force lamina emergent mechanism undergoing testing in a custom-built force-displacement measurement system.

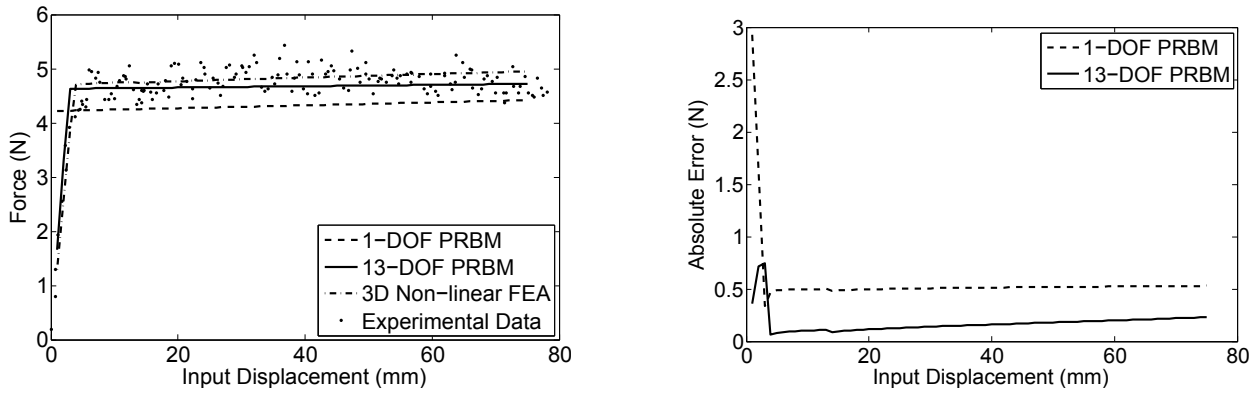

(a) Force Displacement Results

(b) Force Displacement Error

Figure 4.12: (a) Comparison of the force-displacement results from the 1-DOF PRBM, 13-DOF PRBM, finite element analysis (FEA) and experimental data from the constant force mechanism. (b) Absolute error of the 1-DOF PRBM and 13-DOF PRBM as compared to the FEA results.

4.5 Discussion of Results

The example 1-DOF and 2-DOF underactuated mechanisms presented in this paper were readily analyzed using both the method of virtual work and the MinPE method. Both virtual work and MinPE solve the underactuated mechanism problem by seeking the mechanism's lowest energy state, subject to the mechanism remaining assembled (the vector loop equations are satisfied). Both methods are solved using numerical methods, though the root finding methods suited to solving the virtual work equations are generally more efficient than the constrained optimization meth-

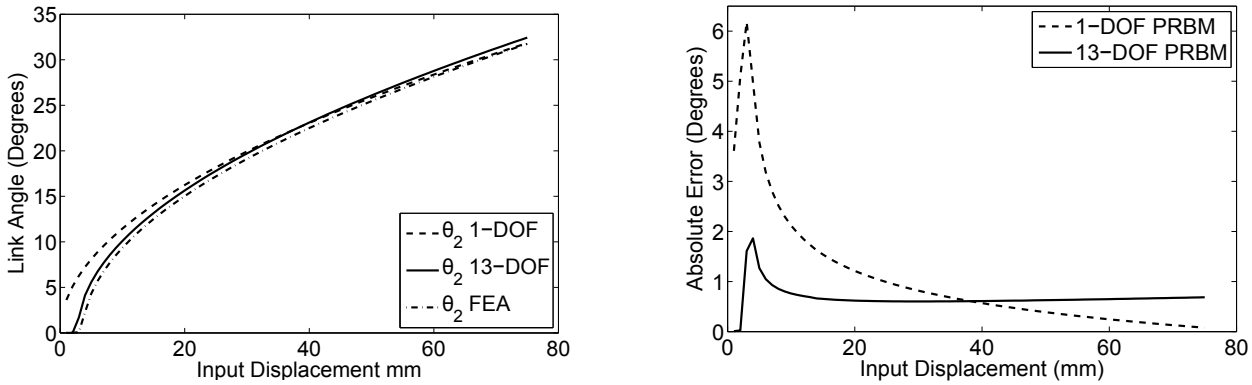

(a) Link Angle Results

(b) Link Angle Error

Figure 4.13: (a) Comparison of the angle of the constant force mechanism's rigid link R_a predicted by the 1-DOF PRBM, 13-DOF PRBM, and finite element analysis (FEA). (b) Absolute error of the 1-DOF PRBM and 13-DOF PRBM as compared to the FEA results.

ods suited to solving the MinPE method. Both methods agreed in the presented 1-DOF and 2-DOF cases to within truncation and round-off error for the numerical solution methods employed.

The compliant constant-force lamina emergent mechanism presented a more relevant case for the application of the MinPE method. Using the non-linear FEA results as a standard of comparison, several observations can be made. The 1-DOF PRBM of this mechanism is easily implemented and quickly analyzed, making it an appealing model for design tasks, such as dimensional optimization. However, when the force-displacement or position data from this model is compared to the FEA results, it becomes apparent that the 1-DOF model fails to accurately predict the non-linearity in the compliant hinges (see Figures 4.12(b) and 4.13(b).

A more complete, underactuated representation of the mechanism can be constructed using the 5-DOF PRBM model of the LET joint. From a design standpoint, a more complete mechanism model accounting for parasitic motion could be advantageous because it more closely represents the true mechanism behavior. However, with a total of 13 DOF, evaluating the PRBM using analytical methods can be challenging. Solution using the method of virtual work, for example, would require the derivation of 13 simultaneous non-linear equations, several kinematic coefficients and other kinematic relationships. Other analytical methods would require similar amounts of analytical manipulation.

The MinPE method makes the analysis of underconstrained and underactuated mechanisms more tractable. In the case of the constant force mechanism's 13-DOF PRBM, the MinPE method

required the statement of only three equations: a potential energy equation, and the X-direction and Y direction components of the vector loop equations. Each of these equations can be stated from the PRBM without further manipulation. Having accounted for the parasitic joint motion, the 13-DOF PRBM more accurately captured the mechanism's highly non-linear forces (Figure 4.12(b)) and link angles (Figure 4.13(b)) than the 1-DOF model.

4.6 Example Extensions of the MinPE Method

As presented here, the MinPE method modeled displacement loaded compliant mechanisms. However, the method can be extended to account for other loading cases and phenomena by modifying existing or adding additional constraint equations. Though certainly not a comprehensive list, the additional constraint equations proposed below are intended to give some examples of how the MinPE method can be extended to more complex cases.

Force or displacement loads may be applied to a mechanism in place of, or in addition to displacement loads. In either case, the MinPE optimization problem can be adapted by adding constraint equations stating that force and moment balance are is satisfied for the link where the forces are applied. For example, suppose a link, r_i, within a mechanism is subjected for force loads in the x and y direction and a moment about the z axis. The MinPE optimization problem would become

$$\begin{aligned}
&\text{minimize} && PE && (4.35)\\
&\text{subject to} && X \text{ direction vector loop} = 0 && (4.36)\\
& && Y \text{ direction vector loop} = 0 && (4.37)\\
& && \textstyle\sum F_x \text{ acting on link } r_i = 0 && (4.38)\\
& && \textstyle\sum F_y \text{ acting on link } r_i = 0 && (4.39)\\
& && \textstyle\sum M_z \text{ acting on link } r_i = 0 && (4.40)
\end{aligned}$$

Contact between a mechanism, such as a grasper, and a stationary can similarly be analyzed using additional constraint equations. Assuming no friction and a perfectly rigid body, the additional constraint equations would state that the end effector's location cannot be within the volume

of the body. For example, consider an end effector's location given by the points X_e, Y_e. Suppose that the end effector will contact a surface S to the right of origin whose x and y coordinates are defined by the functions $S_x(y)$ and $S_y(x)$. In this case, the end effector x coordinate, X_e must be less than (not touching) or equal to (touching) $S_x(Y_e)$. The same is true for the y coordinate, Y_e. Incorporating these constraints into the MinPE problem gives

$$\begin{aligned}
&\text{minimize} && PE && (4.41)\\
&\text{subject to} && X \text{ direction vector loop} = 0 && (4.42)\\
& && Y \text{ direction vector loop} = 0 && (4.43)\\
& && X_e - S_x(Y_e) \leq 0 && (4.44)\\
& && Y_e - S_y(X_e) \leq 0 && (4.45)\\
& && && (4.46)
\end{aligned}$$

4.7 Conclusion

Underconstrained and underactuated mechanisms models can be useful in compliant mechanism design. They may allow the designer to predict undesired parasitic motions in precision mechanisms, or they may be used to model purposely underactuated devices such as compliant graspers. The principal advantage of the MinPE method over analytical methods, such as virtual work, for analyzing underactuated or underconstrained mechanisms is the reduced analytical derivation prior to obtaining a numerical solution for the unknown degrees of freedom. The equations of the MinPE optimization problem can be readily stated from inspection of the pseudo-rigid-body model under consideration and require no additional manipulations. Additionally, all dependent position variables can found without separate derivation and calculation of kinematic relationships since these relationships are implicitly included in the vector loop constraint equations.

When compared to other methods, the MinPE analysis does have some limitations. One limitation of the MinPE method is that it does not provide any insight into the kinematic and energy relationships elucidated by virtual work analysis. Also, non-linear FEA provides a wealth

of information (stress concentrations, the complete displaced structure, etc.) not easily obtainable using the MinPE method.

In its current form, the MinPE method can analyze displacement-loaded pseudo-rigid-body models. Displacement-loaded underconstrained PRBMs may be particularly useful in designing and evaluating more complete PRBMs of compliant mechanisms whose joints have parasitic motion. Extension of the MinPE optimization problem to include force loading, contact, and other phenomenon which can be stated as constraint equations may make the analysis of complex underactuated and underconstrained mechanisms more tractable.

CHAPTER 5. GEOMETRICALLY NON-LINEAR ANALYSIS OF THIN-FILM COMPLIANT MEMS VIA SHELL AND SOLID ELEMENTS

This chapter presents a performance-based comparison of quadratic shell elements with shear deformation and 3-D quadratic solid elements for modeling geometrically non-linear coupled in-plane and out-of-plane deflection of thin-film compliant microelectromechanical systems. A mesh density study of a single out-of-plane torsional compliant element indicates that a relatively coarse shell element mesh can produce force, displacement, and stress results very similar to those predicted by a much larger and computationally costly 3-D solid element model for out-of-plane loading. Shell and 3-D solid element models of a macro-scale prototype of a MEMS compliant lamina emergent constant-force mechanism are shown to agree very well with experientially acquired force displacement data, and to agree well in their estimates of Von Mises stresses. Close agreement of shell element and 3-D solid element models is also demonstrated for models of a thin-film MEMS constant-force mechanism and a thin-film MEMS cellular lance mechanism. Both of these mechanisms exhibit highly non-linear mechanism stiffness, and large, coupled in and out-of-plane displacements. Together, these results strongly suggest that quadratic shell elements with shear deformation can be used to model the coupled in-plane and out-of-plane motion of thin-film compliant mechanisms.[1]

5.1 Introduction

Compliant microelectromechanical systems (MEMS) achieve some or all of their mechanical motion through the deflection of flexible members [2]. When fabricated using thin-film technologies, such as surface micromachining, compliant MEMS can achieve significant motion parallel to the fabrication plane (in-plane motion) [24], [140] and perpendicular to the fabrication plane (out-of-plane motion) [141]–[144].

[1]This chapter has been accepted for publication in *Finite Elements in Analysis and Design* with Brian Jensen and Larry Howell contributing as co-authors.

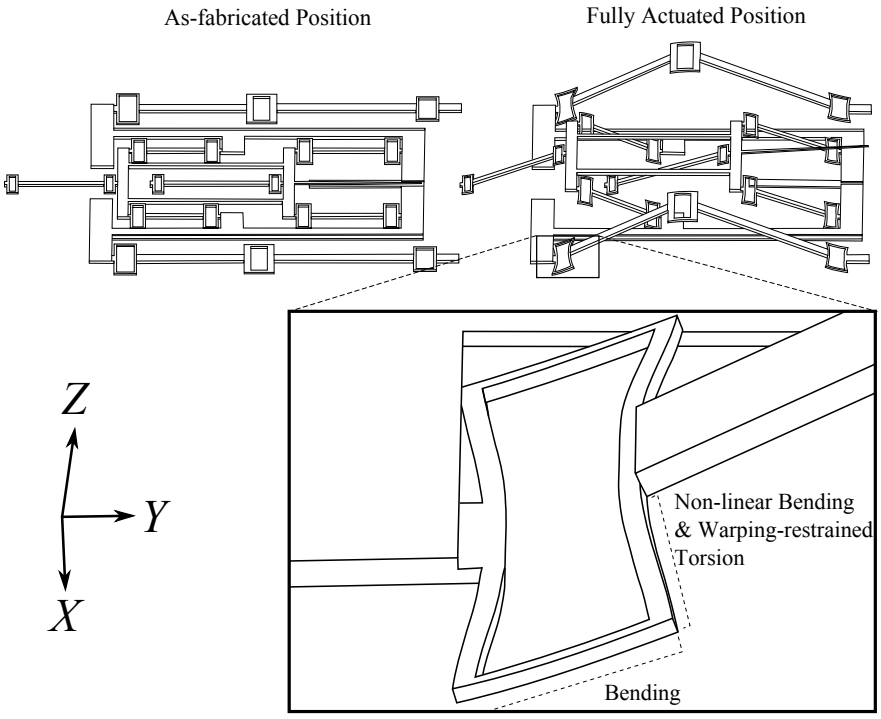

Figure 5.1: Schematic drawing of a fully compliant MEMS device, showing the non-linear combined stress states experienced by the compliant elements.

The anticipated displacement of a compliant mechanism (in-plane, out-of-plane, combined) can be used to select the appropriate type of structural finite element for the model (plane-stress membranes, shells, 3-D solids, etc). Purely in-plane motions can be analyzed with plane-stress membrane elements [145]–[147] or 3-D solid elements [148]. Out-of-plane motion of compliant mechanisms has been modeled using 3-D solid elements [141], [144], [149]–[151], and small out-of-plane deflections of thin structures, such as those experienced by thin-film parallel-plate MEMS switches, can be modeled by shell elements [142]–[144].

The choice of element is less clear for thin-film devices which undergo geometrically non-linear (large displacement, small strain) coupled in-plane and out-of-plane displacements. Large, coupled displacements can produce non-linear stresses in the three normal directions, $\sigma_x, \sigma_y, \sigma_z$, and the three shear stresses, $\sigma_{xy}, \sigma_{xz}, \sigma_{yz}$. Figure 5.1 shows one such case, where a compliant element within a thin-film MEMS device is experiencing combined loads which induce non-linear stress distributions in the flexible members.

The analysis of such mechanisms can be performed using 3-D solid elements, but the analysis can become quite costly, especially when multiple elements are added through a relatively small out-of-plane thickness. Less computationally expensive shell elements are appealing because of the reduced computational cost, but the stresses induced by such coupled motion may violate the shell element assumptions [152]. However, the stresses in the out-of-plane directions of thin-film compliant mechanism will likely be smaller than the in-plane stresses because the compliant members' in-plane widths are typically larger than their out-of-plane thicknesses.

This paper evaluates three cases to determine if shell elements may be used to analyze coupled in-plane and out-of-plane displacements of thin-film compliant MEMS. Each of the cases analyzes the coupled, geometrically non-linear displacements of lamina emergent mechanisms (LEMs) [3], [138]. LEMs are compliant mechanisms fabricated from thin layers of material (lamina) and have elements which emerge from the fabrication plane, achieving significant out-of-plane motion, often applying an in-plane displacement to part of the mechanism.

The three cases considered are the analysis of a micro-scale lamina emergent torsional (LET) joint [139], a fully compliant constant-force [135] LEM analyzed both on the macro and micro-scales, and a fully compliant metamorphic [3] MEMS lance LEM intended for cellular manipulation.

5.2 Case Descriptions

This section describes each of the three cases evaluated. The analyses progress from the simple geometry and loading conditions of a single LET joint, to a constant-force mechanism analyzed on the macro-scale and on the MEMS scale, and finally to a more complex metamorphic MEMS lance mechanism.

5.2.1 Case 1: Analysis of a Lamina Emergent Torsional Joint

Figure 5.2 shows a schematic of the LET joint, and its potential joint deflections. In the first case evaluated, the joint is deflected to 30° of total joint rotation. A shell element model of the LET joint is analyzed at seven different mesh densities and compared to a finely meshed 3-D solid

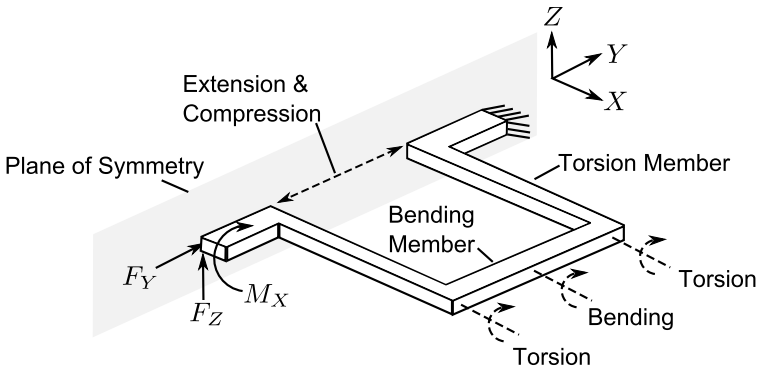

Figure 5.2: A schematic of the lamina emergent torsional (LET) joint, showing its potential joint deflections.

model. This comparison gives an estimate of the shell element mesh density required to produce the same force-deflection and stress results as a finely meshed 3-D solid model.

5.2.2 Case 2: Analysis of a Constant-force Mechanism

The shell element density required to model a single LET joint in Case 1 is applied to model a constant-force compliant mechanism [135] which employs three LET joints of different dimensions, shown in Figure 5.3. Shell and 3-D solid element models of a macro-scale polypropylene constant-force LEM mechanism are compared to experimentally collected force-displacement data reported in [149] to validate the shell and solid models. The Von Mises stress results of the shell and solid element models are also compared.

Shell and solid element models are then developed and compared for a MEMS constant-force mechanism similar in design to the macro-scale constant-force mechanism. The MEMS scale constant-force mechanism is designed for fabrication through the PolyMUMPs prototyping service [4], which allows for two polycrystalline silicon layers, POLY1 and POLY2, which are 2 μm and 1.5 μm thick, respectively.

5.2.3 Case 3: Analysis of a MEMS Lance Mechanism

The third, and most complex case, is the analysis of a fully-compliant, metamorphic, cellular lance mechanism shown in Figure 5.4. The device is intended to inject foreign molecules into cells with a micro-lance and is designed for fabrication using the PolyMUMPs service. The

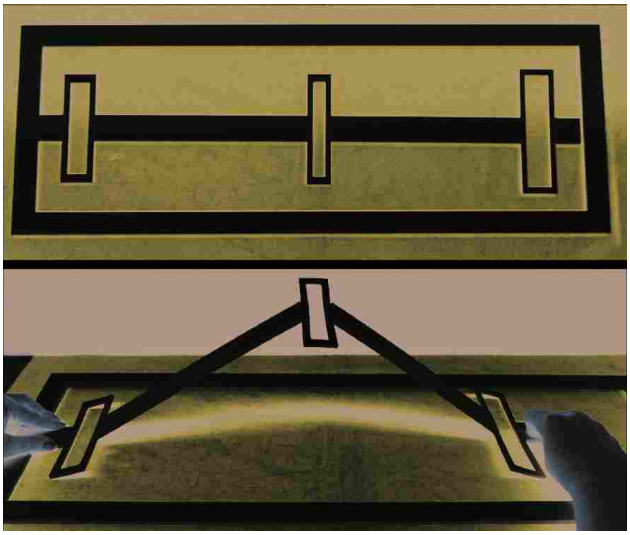

Figure 5.3: Photographs of the macro-scale constant-force mechanism physical prototype in its actuated (top) and as-fabricated (bottom) positions.

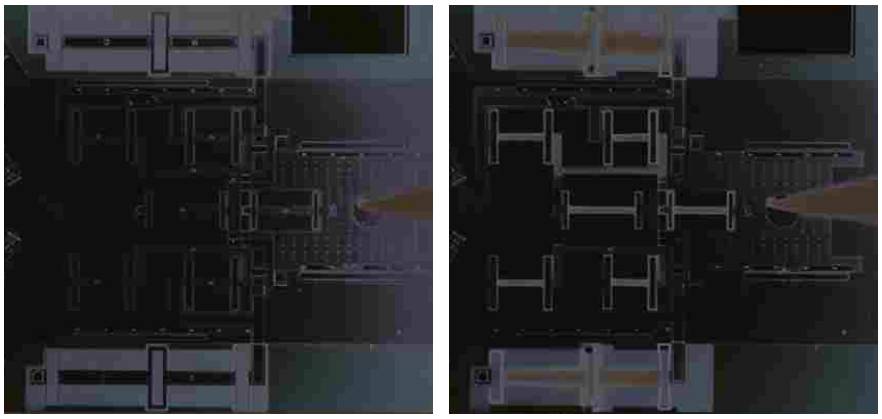

Figure 5.4: Optical micrographs of the LEM cellular lance mechanism in its as-fabricated (left) and fully-actuated (right) positions. A microprobe (right) is actuating the mechanism via a slider. Note: darkening of the rigid links in the displaced configuration (right) indicates those links have rotated as the mechanism moves out-of-plane.

device incorporates multiple LET joints and the MEMS-scale constant-force mechanism analyzed in Case 2. Force displacement and Von Mises stress results are compared for shell and 3-D solid element models of the mechanism.

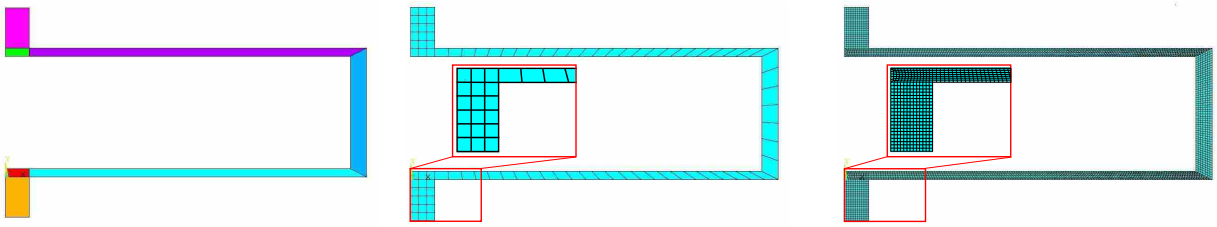

(a) Model Areas (b) Coarsest Mesh Tested (c) Finest Mesh Tested

Figure 5.5: (a) The areas used to form the shell and 3-D solid element models of the LET joint. (b) Coarsest shell element model tested. (b) Finest shell element model tested. Insets show mesh detail.

5.3 Model Meshes, Loads, and Boundary Conditions

All of the finite element analyses were performed using ANSYS 11.0. The shell element models were meshed with SHELL93, quadratic 8 node quadrilateral/triangular elements with shear deformation. The SHELL93 element assumes a linear gradient in the out-of-plane (σ_z) stress and constant transverse shear stresses (σ_{yz}, σ_{xz}), both of which may not be true for large coupled in-plane and out-of-plane displacements. The 3-D solid element models were meshed with SOLID95, quadratic 20-node hexahedral/tetrahedral elements. All the models are displacement and force loaded as described in their respective descriptions.

A consistent units set convenient to MEMS was used to model the MEMS devices presented in this paper. Lengths are in μm, forces are in μN, and stresses are in MPa. The macro-scale constant-force mechanism models were similarly scaled with lengths in mm, forces in mN, and stresses in kPa. Table 5.1 gives the material properties of the polypropylene and polycrystalline silicon of the macro-scale and micro-scale mechanisms, respectively.

Table 5.1: Material properties for the polypropylene and polycrystalline silicon used in macro-scale and micro-scale mechanisms, respectively.

	Young's Modulus	**Poisson's Ratio**
Polypropylene	1.37×10^6 kPa	0.3
Polycrystalline Silicon	1.64×10^5 MPa	0.22

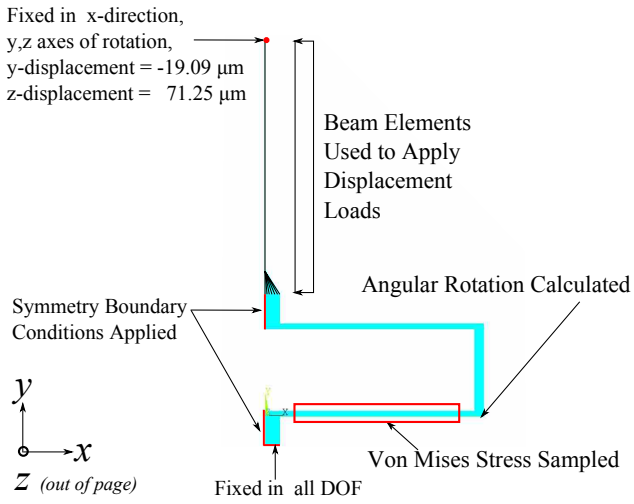

Figure 5.6: Diagram of the boundary conditions and loads applied to the LET joint model.

5.3.1 Case 1: Analysis of a Lamina Emergent Torsional Joint

The polycrystalline silicon MEMS LET joint's symmetry about the plane indicated in Figure 5.2 was exploited, and only half of the joint was modeled as shown in Figure 5.5(a). The geometry of the single LET joint was created directly in ANSYS, and the geometry creation commands were given parametric inputs allowing rapid variation of the joint's geometry if desired. The shell element models used mapped meshing of quadrilateral SHELL93 elements along the torsional and bending members, and free meshing of quadrilateral elements was used in the rigid portions of the LET joint. Additionally, an extension of the rigid portion of the LET joint was modeled using 6-degree-of-freedom (BEAM4) beam elements, as shown in Figure 5.6.

The shell element model was evaluated at the seven different mesh densities given in Table 5.2. Two example meshes are shown in Figure 5.5, the coarsest mesh tested (Mesh 1) and the finest mesh tested (Mesh 7). The 3-D solid element model was generated by extruding a planar mapped mesh pattern to form hexahedral SOLID95 elements. The number of nodes and elements in the 3-D solid element model are also given in Table 5.2.

Both the shell and solid element models were loaded to reflect the symmetry boundary conditions, and a total LET joint rotation of 30°. The rotation was input as y and z components of displacement at the free end of the beam element. The boundary conditions and loads are shown in Figure 5.6. For the shell element model, the boundary conditions along the plane of symmetry

and the fixed end were applied to lines. In the 3-D solid element model, the boundary conditions were applied to areas. Appendix B gives the ANSYS script to analyze shell element model #7.

5.3.2 Case 2: Analysis of a Constant-force LEM

Two LEM constant-force mechanisms were analyzed: one macro scale polypropylene device, shown in Figure 5.3, and a topologically similar MEMS device. The geometries of the macro-scale and micro-scale constant-force LEMs were generated in Siemens NX 5.0 and imported into ANSYS as parasolid (.x_t) files. The polypropylene prototype was fabricated to collect force displacement data for validation of the 3-D solid and shell element modeling methods being applied to the MEMS devices. The aspect ratios of the LET joint members, and the relative thickness of the LET joints and the rigid portions of the constant-force mechanism are approximately the same as those in the MEMS-scale device. Models of both the macro-scale and MEMS-scale constant-force LEM were similarly meshed and loaded as shown in Figures 5.7.

The areas representing the three LET joints were divided as shown in Figure 5.5(a) to facilitate mapped meshing. The shell-element model used mapped meshing of quadrilateral element in the LET, and the rigid sections free meshed with much larger triangular elements. A mesh density similar to that of Shell Mesh 4 from Table 5.2 was used within each LET joint as shown in Figures 5.7(a) and 5.7(c). Table 5.3 gives the total number of nodes and elements in the shell element models.

Table 5.2: Total number of elements and nodes in the shell and solid element models of the LET joint.

	Elements	**Nodes**
Shell Mesh #1	93	428
Shell Mesh #2	334	1,287
Shell Mesh #3	528	1,919
Shell Mesh #4	830	2,899
Shell Mesh #5	1,354	4,579
Shell Mesh #6	1,990	6,635
Shell Mesh #7	3090	10,089
Solid Mesh	11,775	59,837

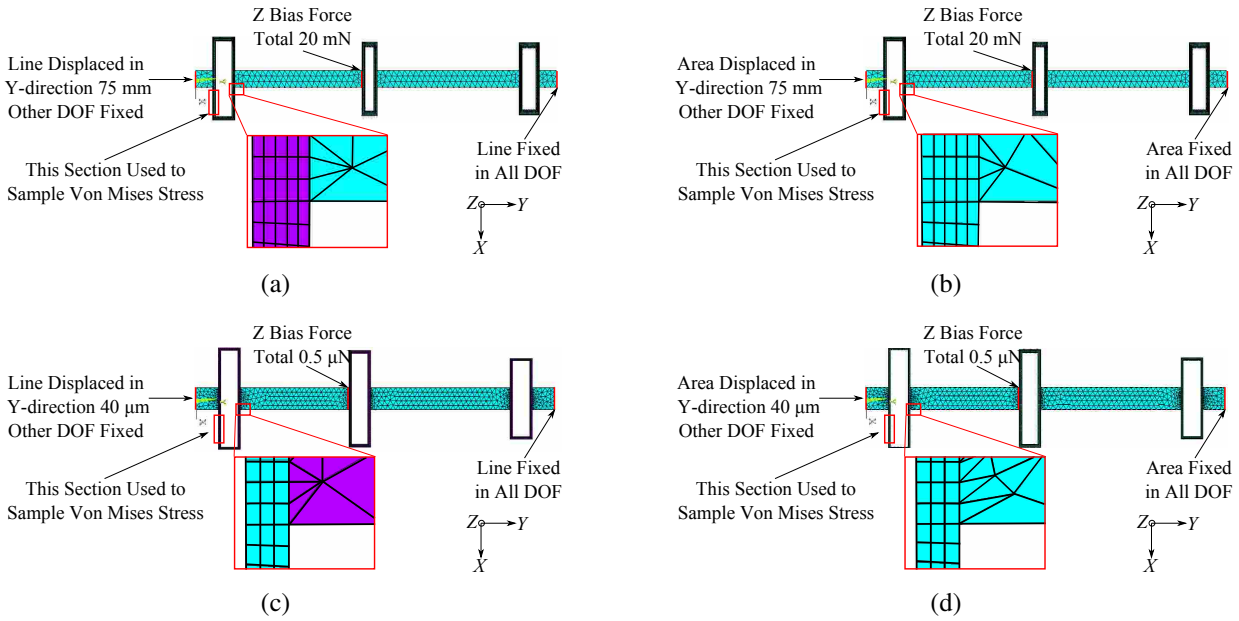

Figure 5.7: Mesh and boundary conditions for the constant-force mechanisms. (a) macro-scale shell element model, (b) macro-scale 3-D solid element model, (c) MEMS shell element model, (d) 3-D solid element model. Insets highlight mesh detail within a compliant joint.

The 3-D solid element models shown in Figures 5.7(b) and 5.7(d) were generated by extruding the unmeshed areas into volumes. The volumes within each LET joint used a hexahedral element mapped mesh, and the volumes representing the rigid portions of the mechanism were free meshed with tetrahedral elements. Table 5.3 gives the total number of nodes and elements in the shell element and 3-D solid element models.

All the models were displacement loaded as shown in Figure 5.7. Each model was also given a small biasing force in the Z-direction (Figure 5.7). The biasing force alone is insufficient to cause the mechanism's large out-of-plane displacements, but is necessary for convergence to

Table 5.3: Total number of nodes and elements in the shell and 3-D solid element models of the constant-force mechanisms.

	Number of Nodes	**Number of Elements**
Macro-Scale Shell	10,364	3,266
Macro-Scale Solid	38,419	7,481
Micro-Scale Shell	9,364	3,000
Micro-Scale Solid	30,966	9,825

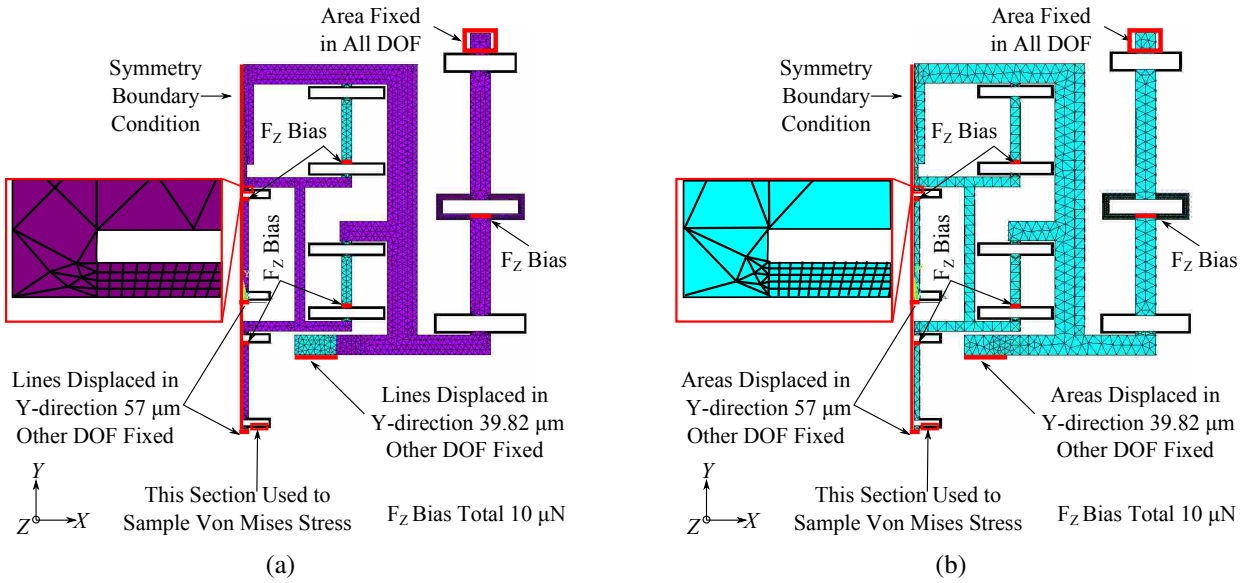

Figure 5.8: Mesh and boundary conditions for the MEMS cellular lance mechanism. (a) Shell element model, (b) 3-D solid element model. Insets highlight mesh detail within a compliant joint.

the out-of-plane motion seen in the physical prototype. The minimum required magnitude of the biasing force was found through trial and error, deceasing the biasing force until no Z-displacement occurred.

5.3.3 Case 3: Analysis of a MEMS Lance Mechanism

The symmetry of the MEMS cellular lance LEM was exploited and only half of the mechanism was modeled in Siemens NX 5.0 and imported into ANSYS as a parasolid (.x_t) file. Figure 5.8 shows the shell element and 3-D solid element meshes of the MEMS cellular lance mechanism. The meshing followed the same pattern as in the constant-force mechanism models; mapped meshing of quadrilateral/hexahedral elements in the flexible members of each LET joint, and free

Table 5.4: Total number of nodes and elements in the shell and 3-D solid element models of the MEMS cellular lance mechanism.

	Number of Nodes	**Number of Elements**
Lance Mechanism Shell	30,966	9,825
Lance Mechanism Solid	121,699	25,406

meshing of much larger triangular/tetrahedral elements in the rigid segments. Table 5.4 gives the total number of nodes and elements in the two models.

The loads and boundary conditions for the shell and solid element models are shown in Figure 5.8. As in the constant-force mechanisms, the displacement loads were applied to lines in the shell element model and applied to areas in the 3-D solid element model. Also, similar to the constant-force mechanism models, small Z-direction biasing loads were applied to nodes as shown in Figure 5.8 to encourage convergence to the out-of-plane configuration.

5.4 Solution Parameters

All models were solved using a sparse matrix, non-linear solver employing a full Newton-Raphson algorithm (ANSYS NLGEOM command). The displacement loads were ramped across multiple load steps, and biasing loads in the constant-force and MEMS lance mechanisms were constant through all load steps. The number of load steps in each model, the RAM required to solve each non-linear iteration, and time required to solve each complete model are given in Table 5.5.

Table 5.5: Load steps, RAM required for one non-linear iteration, and time required to solve each complete model.

	Load Steps	**RAM (MB)**	**Time (min)**
LET Joint Shell #1	10	2.4	0.1
LET Joint Shell #2	10	9.0	0.3
LET Joint Shell #3	10	14.1	0.5
LET Joint Shell #4	10	38.0	0.6
LET Joint Shell #5	10	44.5	1.0
LET Joint Shell #6	10	62.9	1.4
LET Joint Shell #7	10	115.7	2.3
LET Joint 3-D Solid	10	907	19.4
Macro Constant-Force Shell	50	110.2	7.0
Macro Constant-Force 3-D Solid	50	363.3	24.3
MEMS Constant-Force Shell	40	85.4	5.1
MEMS Constant-Force 3-D Solid	40	257.7	15.9
MEMS Lance Mechanism Shell	100	257.7	39.0
MEMS Lance Mechanism 3-D Solid	100	990.3	118

5.5 Post Processing Results

Two broad performance metrics were evaluated for each model: the force displacement behavior of the model and the maximum Von Mises stress sampled at a predetermined region in the model. The Von Mises stress was sampled in the middle of a LET joint torsional member in each model, as shown in Figures 5.6, 5.7 and 5.8. This location in the LET joint experiences combined bending and torsional loads and would highlight any discrepancies between shell and 3-D solid element model stress results.

5.5.1 Case 1: Analysis of a Lamina Emergent Torsional Joint

The force displacement behavior of each LET joint model was characterized by the reaction loads at the free end of the beam element and the angular rotation of the lower right torsional member (measured at the lower right outside corner of the LET joint) as shown in Figure 5.6. In the shell element model, the torsion member's rotation was extracted from the X-axis rotation of the node at the location shown in Figure 5.6. In the 3-D solid element model, the rotation was found by calculating the angular rotation of the vertical (Z-direction) edge at the location shown in Figure 5.6 from individual nodal displacements. The maximum Von Mises stress in the region indicated in Figure 5.6 was also found.

When plotted graphically, a pattern of asymptotic convergence can be seen in the displacement and reaction force/moment results shown in Figures 5.9 and 5.10. The maximum Von Mises stress predicted by the shell element models also converges to within a few percent of the solid element model predictions, though with a slight oscillation.

5.5.2 Case 2: Analysis of a Constant-force LEM

Figure 5.11 shows the displaced constant-force mechanisms, plotted with Z-direction contours. The input force (model Y-direction) and the input displacement (model Y-direction) were calculated for the four models analyzed. Figure 5.12(a) compares the shell and solid element results for the macro-scale polypropylene constant-force mechanism with a force displacement curve from physical testing of the mechanism reported in [149]. Figure 5.12(b) shows the force deflection curves for the shell and solid element models of the MEMS constant-force mechanism. Note

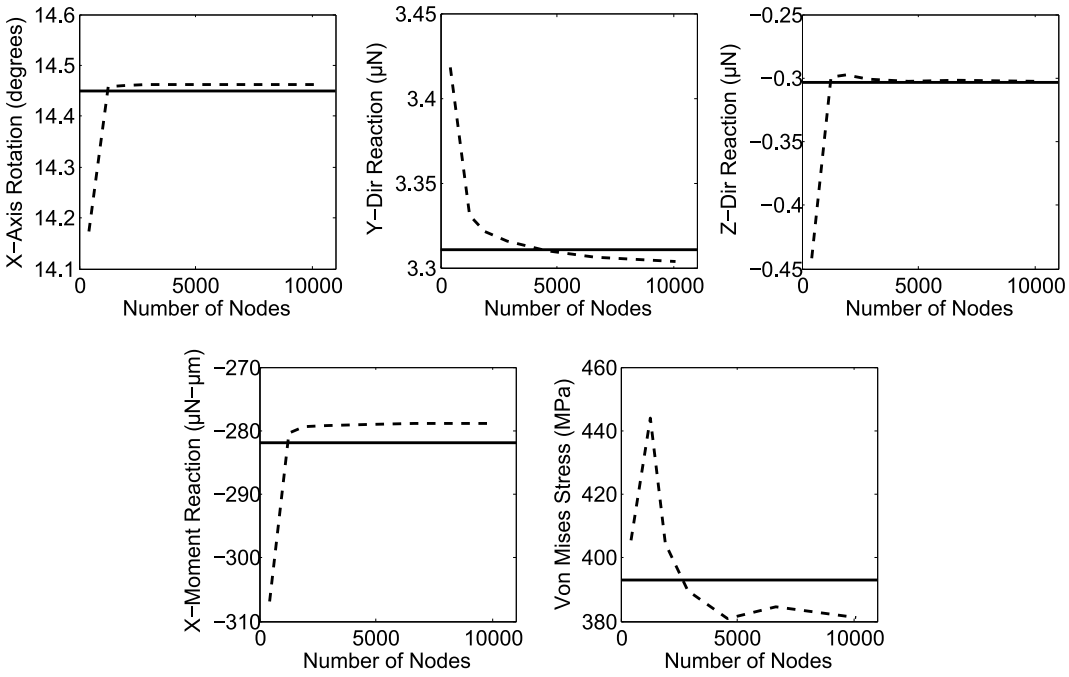

Figure 5.9: Displacement and reaction force results as functions of total nodes in the shell element models of the LET joint. The solid line in the figure indicates the result obtained with the 3-D solid element model.

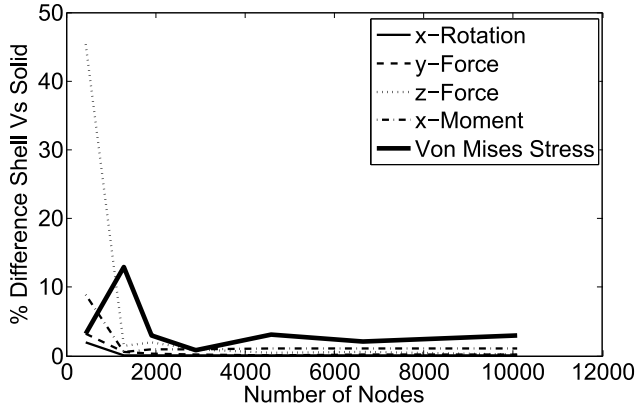

Figure 5.10: Percent difference between shell and 3-D solid element model displacement and reaction force results as functions of total nodes in the shell element models.

the highly non-linear nature of the force-displacement curves, especially the relatively large, flat, nearly constant-force region.

Table 5.6 gives the maximum Von Mises stress in the sample region indicated in Figure 5.7, and the percent difference in the Von Mises stress between shell and 3-D solid element models.

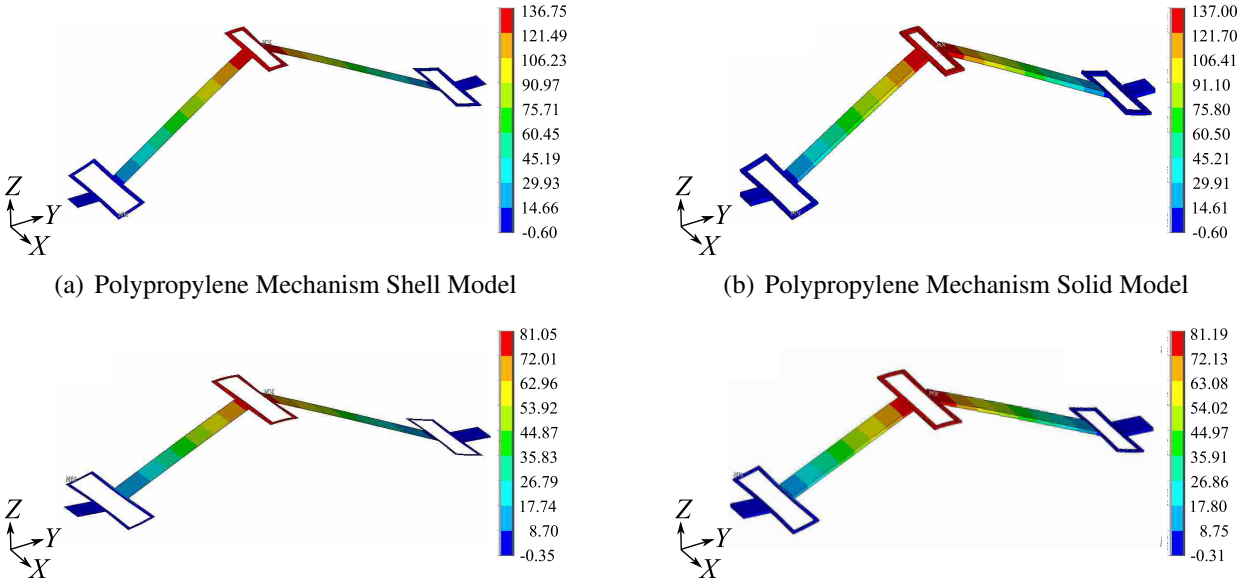

(a) Polypropylene Mechanism Shell Model

(b) Polypropylene Mechanism Solid Model

(c) MEMS Mechanism Shell Model

(d) MEMS Mechanism Solid Model

Figure 5.11: Z-direction displacement contour plots of the constant-force mechanisms. (a) polypropylene shell element model, (b) polypropylene 3-D solid element model, (c) MEMS shell element model, (d) MEMS 3-D solid element model. The polypropylene model displacements are in mm, and the MEMS model displacement are in μm.

5.5.3 Case 3: Analysis of a MEMS Cellular Lance LEM

Figure 5.13 shows the MEMS lance mechanism in its final displaced configuration, plotted with Z-direction contours. Figure 5.14 compares the shell and solid element force displacement results (Y-direction input force vs input displacement) for the shell and 3-D solid element models. Again, note that both the shell and 3-D solid element models captured the highly non-linear force deflection characteristics of the compliant MEMS lance mechanisms. Table 5.7 gives the maximum

Table 5.6: Maximum Von Mises stress in the sample regions indicated in Figure 5.7, and the percent difference in the Von Mises stress for the macro-scale and MEMS constant-force mechanisms.

	Von Mises Stress (MPa)	**Percentage Difference**
Macro-scale Shell	12.07	7.58%
Macro-scale 3-D Solid	13.06	N/A
MEMS-scale Shell	890.5	5.84 %
MEMS-scale 3-D Solid	945.7	N/A

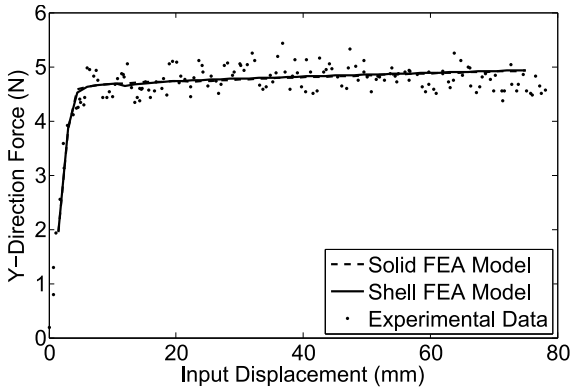

(a) Polypropylene Constant-force Mechanism

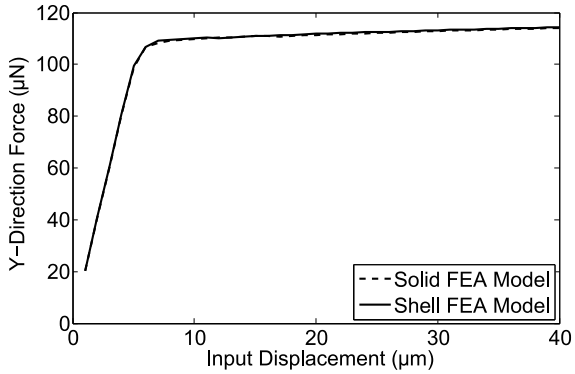

(b) MEMS Constant-force Mechanism

Figure 5.12: (a) Comparison of force-displacement results for the constant force LEM's shell element model, solid element model, and the data collected from the physical prototype. (b) Comparison of force-displacement results for the constant force MEMS-scale LEM's shell element model and 3-D solid element model. Note, in both cases, the shell and solid element models' force displacement overlap each other.

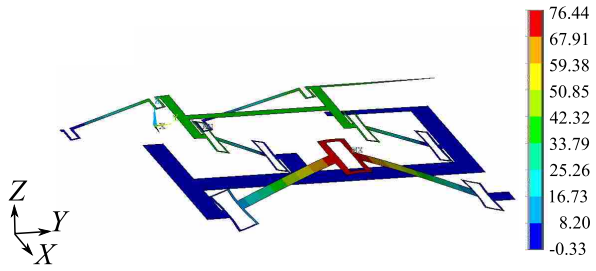

(a) Lance Mechanism Shell Model

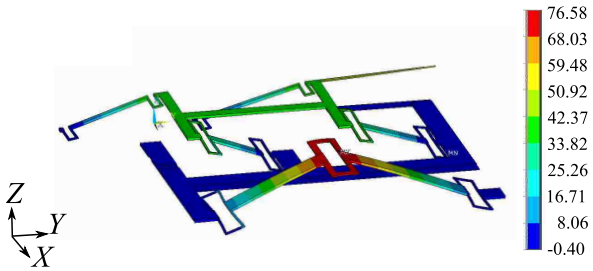

(b) Lance Mechanism 3-D Solid Model

Figure 5.13: Z-direction displacement contour plots of the MEMS lance mechanism (a) shell element model and (b) 3-D solid element model. The displacements are in μm.

Von Mises stress in the sample region indicated in Figure 5.8, and the percent difference in the Von Mises stress.

5.6 Discussion of Results

The shell element models of a single LET joint showed rapid displacement and reaction convergence to within 1% of the values given by the solid element model of the same geometry. The maximum Von Mises stress quickly converged to within 3% of the solid model predictions. In comparing the trade-off between computational effort and results convergence, it was found that

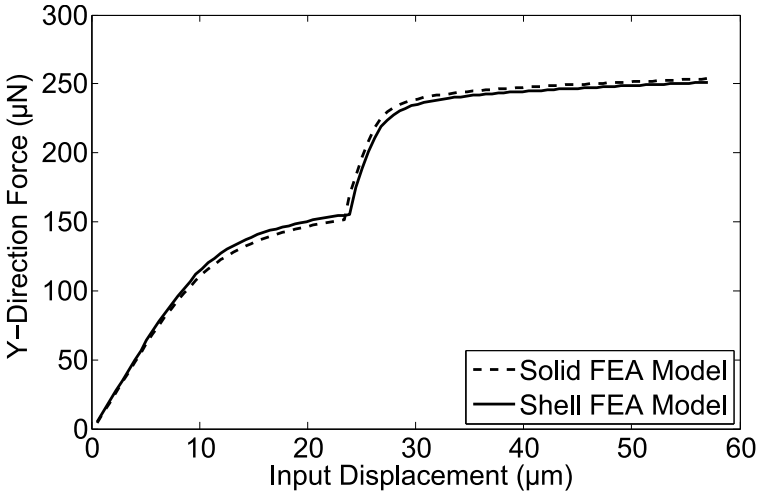

Figure 5.14: Force displacement results for the shell and 3-D solid models of the MEMS lance mechanism. Forces are in μN and displacements are in μm

the mesh density in LET joint shell element model #4 provides force, displacement, and stress results within 3% of the solid model results, but approximately 30 times faster than the 3-D solid element model. LET joint shell element model #4's mesh density was applied to the LET joints of the shell and 3-D solid element models of the constant-force mechanisms and the MEMS lance mechanism.

For the macro-scale polypropylene constant force mechanism, both the force-deflection curves produced by the shell element and 3-D solid element models agree very well with the experimentally collected force-deflection data. This result indicates that both the shell and 3-D solid element models accurately predict the non-linear stiffness of this compliant mechanism. The Von Mises stress results for the shell and 3-D solid element models are also in close agreement, differing by 7.58%. The time to solve each model, however, is quite different, with the shell

Table 5.7: Maximum Von Mises stress in the MEMS lance mechanism for the sample region indicated in Figure 5.8, and the percent difference in the Von Mises stress shell and 3-D solid element models.

	Von Mises Stress (MPa)	**Percentage Difference**
Lance Mechanism Shell	879.5	0.80 %
Lance Mechanism 3-D Solid	886.6	N/A

element model solving approximately three times faster than the 3-D solid element model of similar mesh density.

The macro-scale constant force-mechanism was designed to have similar aspect ratios and relative displacement (input displacement compared to overall mechanism size) as the topographically similar MEMS constant-force mechanism. The close agreement between the experimental and computed force-displacement curves for the macro-scale case suggests that the shell and 3-D solid element models of the micro-scale constant-force mechanism will likely also be accurate.

As was the case for the macro-scale constant-force mechanism models, the MEMS constant-force mechanism shell and 3-D solid element models agree very closely. The force-deflection curves for the two models are nearly identical, and the Von Mises stress results for the shell and 3-D solid element models closely agree, differing by 3.17%. Once again, though the force-deflection and stress results are similar for the shell and 3-D solid models, the shell element model solved over ten times faster than the 3-D solid element model of similar mesh density.

The finite element MEMS cellular lance mechanism is a more complete and complex model of a fully compliant MEMS mechanism. In this case, the shell and 3-D solid element models predict essentially the same highly non-linear force-displacement behavior for the MEMS lance mechanism. The two models' Von Mises stress estimates are also very similar, differing by only 0.08%. The shell element model achieved these results while solving approximately 3 times faster than the 3-D solid element model.

5.7 Conclusion

This paper presented comparisons between quadratic shell elements with shear deformation and 3-D quadratic solid elements for modeling geometrically non-linear coupled in-plane and out-of-plane behavior of thin-film MEMS compliant mechanisms. A mesh density study of a single compliant lamina emergent torsional joint demonstrated that a relatively coarse shell element mesh could produce force, displacement, and stress results very similar to those predicted by a much larger and computationally costly 3-D solid element model. When comparing shell and 3-D solid element models for increasingly complex thin-film MEMS, the shell elements consistently provided results close to those of the 3-D solid element models. Together, these three cases

strongly suggest that quadratic shell elements with shear deformation can be used to model the coupled in-plane and out-of-plane motion of thin-film compliant mechanisms.

CHAPTER 6. PRELIMINARY RESULTS FOR CYTOPLASM-TO-PRONUCLEUS NANOINJECTION

This report gives the motivation and preliminary results for a proposed method of DNA transfer called cytoplasm-to-pronucleus nanoinjection. Cytoplasm-to-pronucleus nanoinjection is based on the principle that an electric field formed around a charged body can cause micro-pores to open in the membranes of a living cell. By placing a DNA coated lance into the cytoplasm of a mouse zygote and applying a voltage pulse of sufficient magnitude and duration, pores may open in the pronuclear membranes and DNA is electrophoretically repelled from the lance. If effective, this process could result in transgenes without having to visualize and physically penetrate into the pronucleus. 24-hour and 10-day embryo viability data are presented for mouse zygotes nanoinjected at voltages above the decomposition voltage of the nanoinjector system. Observed 24-hour viabilities ranges from 23% (1.25 volts above electrolysis 10 ms pulse) to 67% (1 volt above electrolysis 10 ms pulse). Further study is needed to increase consistency and to determine if cytoplasm-to-pronucleus nanoinjection can generate transgenic animals.[1]

6.1 Introduction

This report summarizes the preliminary cell viability results for a proposed cytoplasm-to-pronucleus nanoinjection process. In this embodiment of the nanoinjection process, a DNA coated, positively charged nanoinjector lance (Figure 6.1) is inserted into the cytoplasm of a cell without regard to the location of the pronucleus within the cell. A sufficiently large negative voltage pulse (or pulses) is applied to the lance to induce pore formation [153], [154] in the pronucleus. The accumulated DNA is then moved off of the lance, and through the newly opened pores into the pronucleus via electrophoretic motion. A schematic of the proposed process is shown in Figure 6.2.

[1]This chapter has submitted as a status report to Nanoinjection Technology LLC with Robert Rawle, Nathan Toone, Larry Howell, Brian Jensen and Sandra Burnett, contributing as co-authors. Robert Rawle performed most of the experiments reported in this chapter, and Nathan Toone provided the mathematical modeling reported in this chapter.

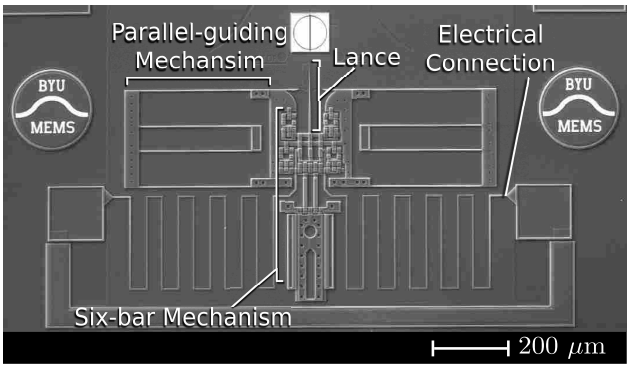

(a) SEM of a nanoinjector

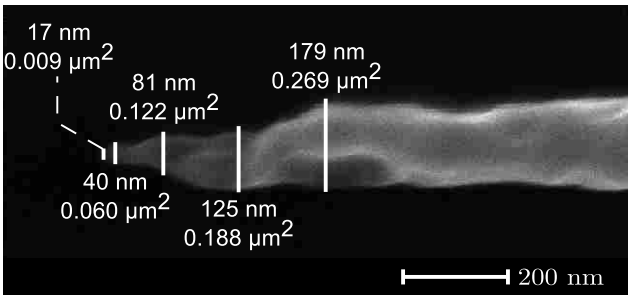

(b) SEM of the lance tip

Figure 6.1: Labeled scanning electron microscope (SEM) images of (a) the nanoinjector in its as-fabricated position with its principal components labeled and (b) the tip of the nanoinjector lance showing several in-plane widths and cross-sectional areas. The lance has a nominal thickness of 1.5 μm.

Our recent results for targeted pronuclear nanoinjection have demonstrated that electrophysical injection of DNA can result in transgene integration. However, operating the nanoinjector at voltages below those required to form pores in the pronuclear membranes necessitates physical entry of the lance into the pronucleus, as is currently done in microinjection [5], [52], [57]. Eliminating the need to target the pronucleus would increase the speed and ease of transgenic animal production. Additionally, cytoplasm-to-pronucleus nanoinjection would be insensitive to the size, location, and visibility of the pronuclei. This would make transgenesis more accessible in biologically important animals whose zygotes are difficult to transfect because of the visibility of their pronuclei [62], [63], [155].

Successful cytoplasm-to-pronucleus nanoinjection will have a significant accelerating impact on the many research areas that use transgenic organisms. Improved ability to generate transgenic animals will promote the development of new treatments for disease, new understanding of

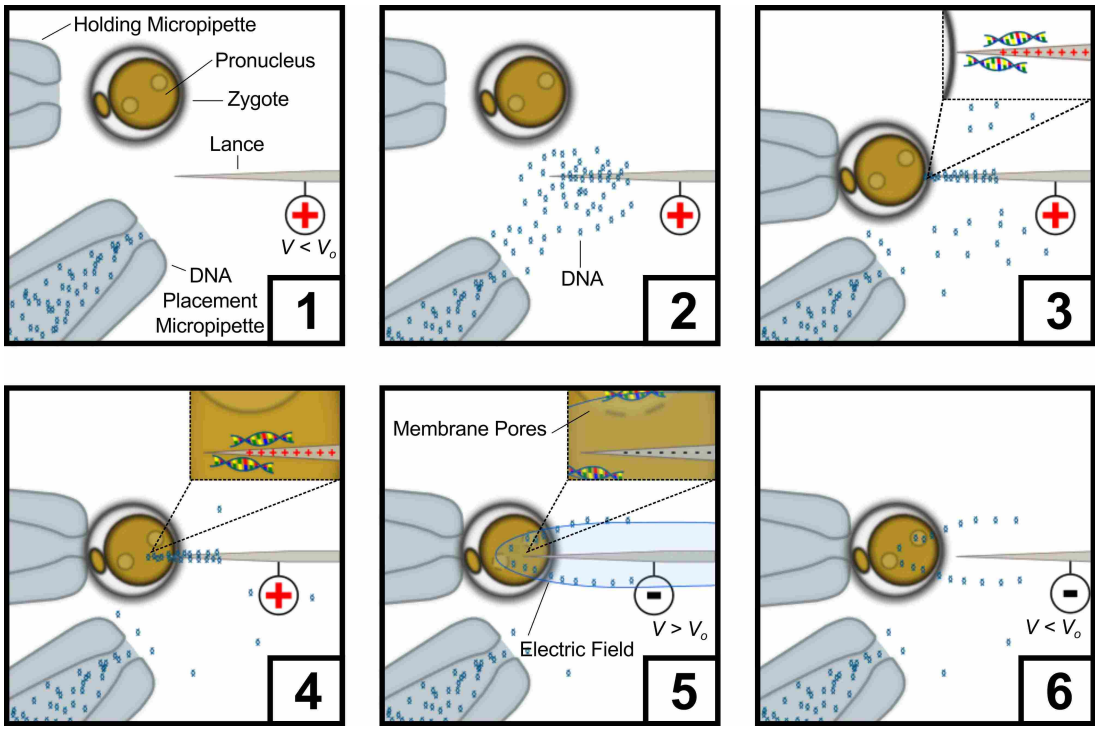

Figure 6.2: Schematic illustration of one cycle of cytoplasm-to-pronucleus nanoinjection. (1) the lance is connected to the positive terminal of a voltage source operating below the decomposition voltage (V_o). (2)-(3) DNA added to the ambient media accumulates on the lance. (4) The positively charged lance penetrates into the cytoplasm. (5) A the lance is connected to a the negative terminal of a voltage source operating above the decomposition voltage ($V > V_o$) for a millisecond-scale duration. The resulting electric field forms pores in the pronuclear membrane, and repels DNA from the lance. (6) The voltage is reduced to below the decomposition voltage ($V < V_o$) and the lance is withdrawn.

genetic effects in responses to drugs, and expanded knowledge of the causes of and treatments for genetic disorders and cancer. This broad influence is possible because transgenic organisms are a vital part of many research areas, including immunology [16]–[19], cancer [11]–[13], genetic disorders, genomics, reproduction [14], [15], infectious diseases, development, aging [21], and metabolism.

6.2 Background

This section provides a brief survey of the enabling principles and preliminary results for cytoplasm-to-pronuclear nanoinjection. Specifically, this section describes the decomposition voltage of a system, its importance for electrophoretic motion, and how the decomposition voltage may

be determined. The principles and some existing applications of the electric-field-mediated formation of membrane pores are discussed. Finally, prior modeling results are presented which suggest that cytoplasm-to-pronuclear nanoinjection may be feasible.

6.2.1 Decomposition Voltage and Electrophoretic Motion

Electrophoretic motion, or the electric-field-driven motion of charged particles in an ionic solution, only occurs when the voltage applied to the system exceeds a threshold called the decomposition voltage [114], [156]. Electrophoresis can be used to move molecules having a net charge, or an effective net charge like DNA [97], across micro-scale [27], [28] and macro-scale distances [157], [158].

In a simplified model, the decomposition voltage is a consequence of the dissolved ions surrounding each electrode, called the electric double layer (EDL) [88]. As shown in Figure 6.3(a), below the decomposition voltage the EDL effectively shields the charges on the electrodes. Thus, a charged particle between the electrodes does not experience any electromotive force, and there is no electrical current flow due to the movements of ions in the solution [115]. During micro-scale gel electrophoresis of DNA reported in [114], with applied voltages below the decomposition voltage, no significant motion of the DNA was detected.

Above the decomposition voltage, the electric field extends beyond the EDL and current flows between the electrodes through the movement of ions in the electrolyte solution. This principle is shown schematically in Figure 6.3(b), and is observed, for example, in the directed motion of DNA between electrodes during gel electrophoresis [114]. Additionally, in aqueous solutions, electrolysis occurs above the decomposition voltage, forming hydrogen at the negative electrode and oxygen at the positive electrode. Figure 6.4 shows an example of hydrogen bubbles generated on the nanoinjector lance when a negative pulse greater than the decomposition voltage was applied to the lance.

The decomposition voltage depends upon such factors as the electrode material(s), the presence of a surface oxide on the electrode material, and the electrolyte solution's composition [156]. An empirical plot of current as a function of applied voltage (an IV curve) can be developed for a system by measuring the current flow between electrodes at voltages above and below the decomposition voltage. An example IV curve for the nanoinjector in room temperature phosphate

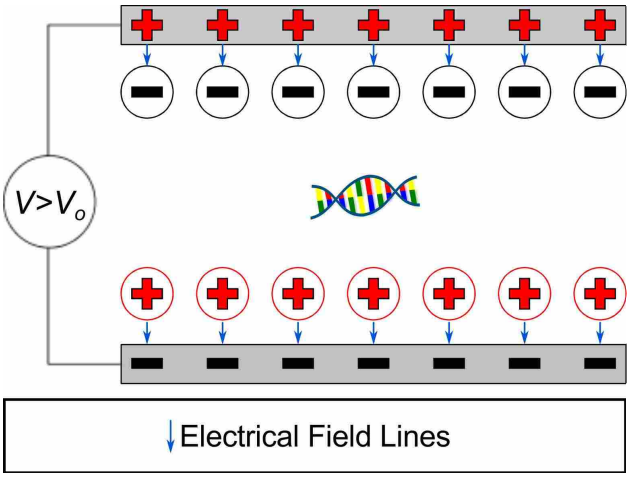

(a) Below the Decomposition Voltage V_o

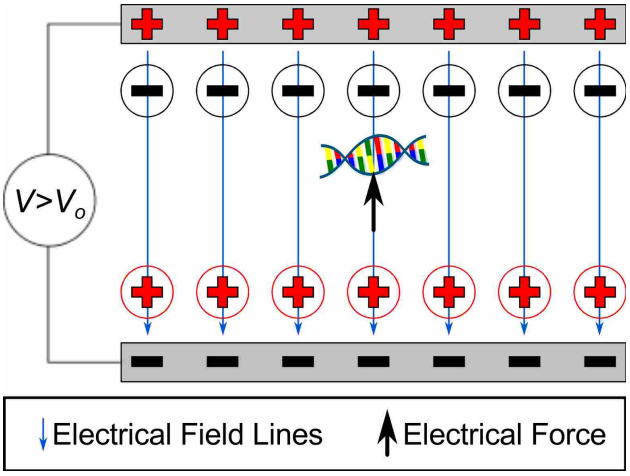

(b) Above the Decomposition Voltage V_o

Figure 6.3: Simplified representation of the electric double layer (EDL) showing how (a) below the decomposition voltage (V_o) the ions in solution effectively shield the surface charges on the electrode such that the DNA molecule between the electrodes experiences no electrical force. (b) If the voltage $V > V_o$ then the electric field extends beyond the EDL and the DNA particle experiences an electric force.

buffered saline (PBS)[2] is shown in Figure 6.5. Note that the voltage at which visible electrolysis on the nanoinjector lance occurs is above the decomposition voltage.

[2] 137 mM NaCl, 2.7 mM KCl, 11.7 mM Na_2PO_4-$7H_2O$

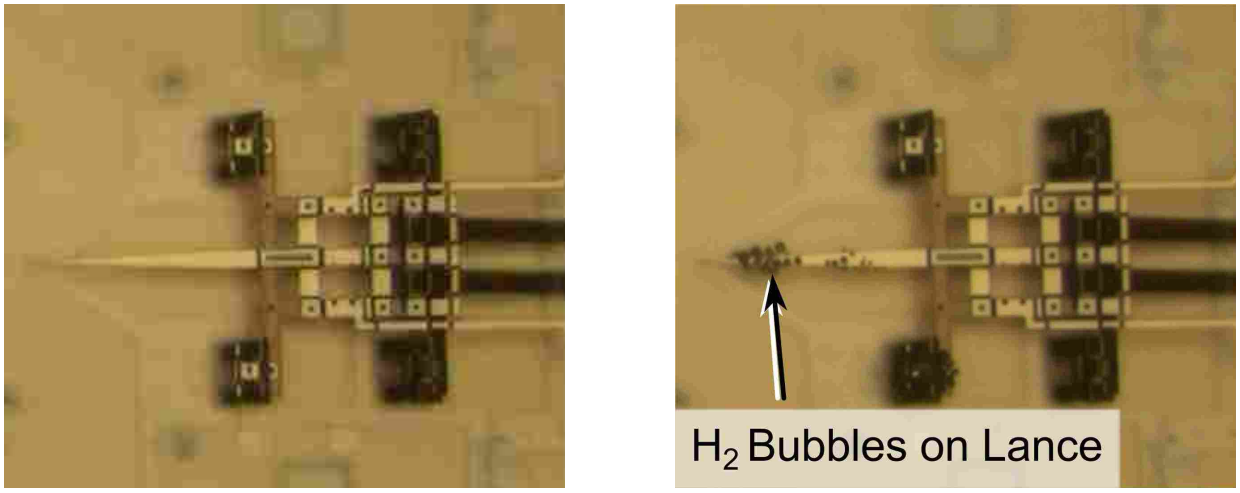

(a) Before Applying Pulse

(b) After Applying Pulse

Figure 6.4: Video frames showing (a) before and (b) after a pulse with V$> V_o$ (-8 V, 10 ms) was applied to the nanoinjector. Hydrogen bubbles formed by electrolysis can be seen on the tip of the lance.

6.2.2 Electroporation

Electroporation is the process of opening micropores in the cell and/or nuclear membranes of a cell by applying an electric field [153], [154] . Under normal conditions the membrane lipid bilayer (BLM) surrounding the cell or nucleus is semipermeable, with the BLM being impermeable to large and/or hydrophilic molecules. When a sufficiently large electric field is applied for microseconds to milliseconds, pores open in the BLM within microseconds, and additional pores may also open through the denaturing of membrane proteins. The pores allow large and/or hydrophilic molecules such as DNA, RNA, or drugs to enter the cell, and simultaneously allow ions and macromolecules to leak from the cell into the surrounding media. [153]

If the magnitude and duration of the pulses are small enough, the membrane pores will close in milliseconds to seconds, resulting in reversible electroporation. However, if the magnitude and duration of the pulses are too large, the membrane may undergo irreversible electroporation, in which the BLM or protein pores close in minutes to hours. Irreversible electroporation may result in cell lysis and cell death. [153]

Transfection of eukaryotic cells is one of the most valuable applications of reversible electroporation. DNA transfer via electroporation has been demonstrated in differentiated cells [72],

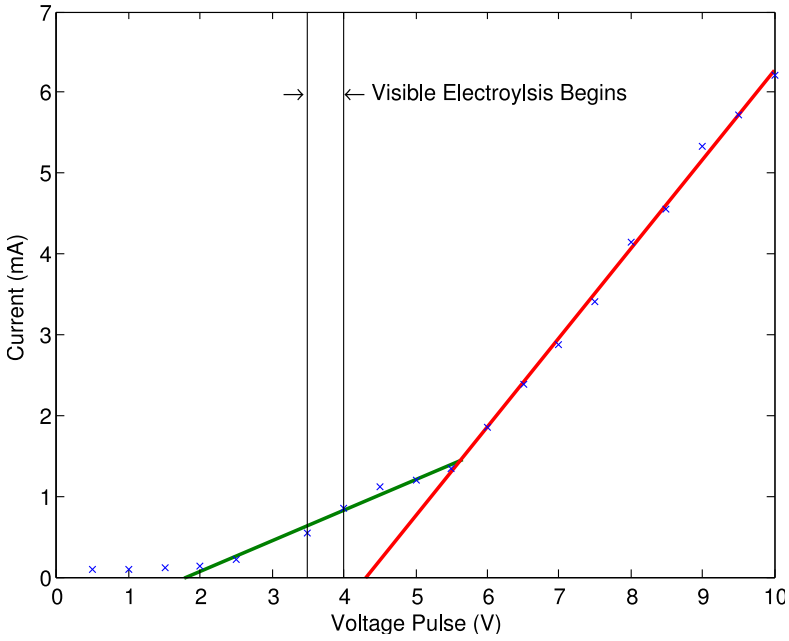

Figure 6.5: Current as a function of voltage (IV curve) for the nanoinjector. The current measurements were taken by measuring the current flow to the nanoinjector during 50 ms pulses with the nanoinjector connected to the negative voltage terminal.

whole post-implantation embryos [74], [154], and embryonic stem cells [20], [80], [81]. Mouse zygotes have been shown to survive electroporation conditions [75]. Dyes and siRNA have been electroporated into mouse zygotes [76], and siRNA has been electroporated into pre-implantation embryos through the blastocyst phase [159]. However, successful electroporation transfer of transgenes into pre-implantation mouse embryos, including zygotes, has not been demonstrated. Electroporation of siRNA, as reported in [76], [159], was most efficient for millisecond scale pulses with field strengths of approximately 20–30 V/cm.

6.3 Modeling the Lance's Electric Field

The mathematical model of DNA motion around the nanoinjector lance presented in [87], [114], [156] was used to determine pulse magnitudes and durations likely to cause electroporation of the pronuclei within a mouse zygote.[3] For successful cytoplasm-to-pronucleus injection two conditions must be met. First, the duration of the pulse must be sufficient to repel the DNA from the lance into the pronucleus using electrophoretic motion. Second, the "electric field envelope" in

[3]The data and images presented in this section were generously contributed by Nathan Toone

which the magnitude of the electric field is greater than or equal to that required to open membrane pores must coincide with the location of one or both of the pronuclei.

Simulations were run for the repulsion of 50 DNA molecules from a lance placed approximately 60 μm into the zygote's cytoplasm. The model included one electrode representing the silicon nanoinjector lance, one electrode representing one of the nanoinjector's silicon bond pads, and one electrode representing the gold return electrode on the nanoinjector chip's surface. The model assumes that the DNA motion takes place in a solution with the same electrical properties as phosphate buffered saline (PBS).

The time required for each particle to reach the edge of the cell was calculated, as was the electric field envelope for 200 V/cm. In practice, the time required to reach the edge of the cell is a conservative estimate for the required pulse duration, because of the proximity of the pronuclear membranes to the center of the cell. The field strength of 200 V/cm was chosen to find the electric field envelope based on the successful electroporation of siRNA reported in [76].

Table 6.1 gives mathematical modeling results predicting the time required for DNA particles to travel from random locations along the length of the lance to edge of the cell. Three simulations were run for each voltage level tested. As expected, at the decomposition voltage of the system, the DNA motion is quite slow in comparison to one, two, or three volts above decomposition.

Figure 6.6 shows the mathematical predictions for the size of electric field envelope where the electric field's magnitude is $\geq$ 200 V/cm. As the voltage is increased from $V_o + 1$ V to $V_o + 3$ V,

Table 6.1: Mathematical model predictions of the minimum, maximum, and average time for 50 individual DNA particles repelled from the nanoinjector lance to reach the edge of the cell. All times are in milliseconds.

	$\mathbf{V_o}$	$\mathbf{V_o + 1}$ V	$\mathbf{V_o + 2}$ V	$\mathbf{V_o + 3}$ V
Run 1 Ave	1977.1	27.3	13.0	9.2
Run 2 Ave	2274.9	25.9	13.9	8.6
Run 3 Ave	2139.2	29.5	13.3	8.5
Total Ave	2132.5	27.6	13.4	8.7
Total Std Dev	1702.0	7.4	3.9	2.5
Max	8331.0	36.0	18.2	12.1
Min	140.1	7.7	3.8	2.7

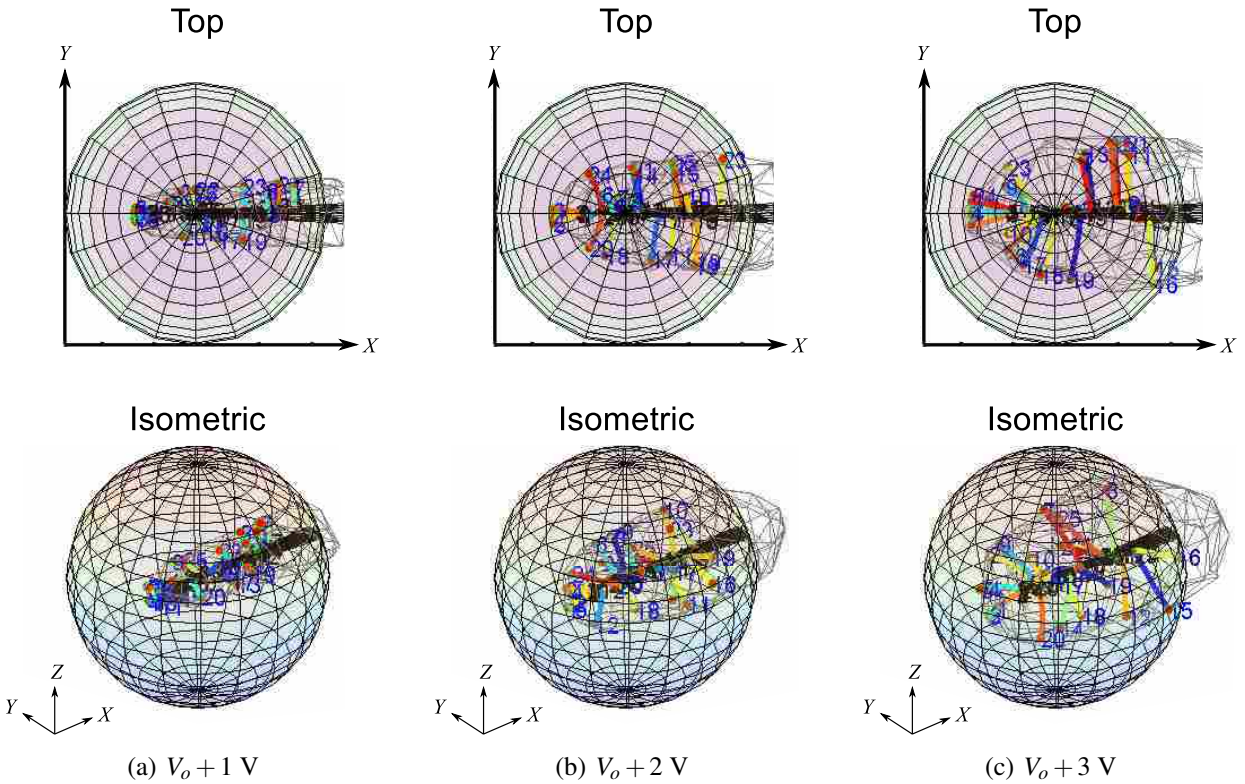

(a) $V_o + 1$ V (b) $V_o + 2$ V (c) $V_o + 3$ V

Figure 6.6: Plots from the mathematical modeling of the electric field around the nanoinjector lance showing the portion of the cell where the electric field strength is ≥ 200 V/cm. This electric field strength is expected to cause electroporation of the cell membrane and pronuclear membrane [76]. The colored lines and numbers indicate the paths followed by individual DNA particles repelled by the lance.

the size of the electric field envelope increases. At $V_o + 3$ V the electric field is ≥ 200 V/cm in a volume large enough to encompass some or all of both pronuclei. Note, however, that at even at $V_o + 3$ V, the electric field envelope only impacts a portion of the cell membrane, suggesting that pores may be opened only in a localized region around the lance.

The results presented in Table 6.1 and Figure 6.6 both suggest that operating at increasingly higher voltages above the decomposition voltage increases the likelihood of successful cytoplasm-to-pronucleus nanoinjection via reversible, localized electroporation. However, as noted above, increasing the magnitude and/or duration of the applied pulse can lead to irreversible electroporation and cell lysis. Thus a balance must be found between cell survival and increasing pulse magnitude and duration to maximize the electroporated region and the DNA velocity.

6.4 Cytoplasm-to-Pronucleus Materials and Methods

Cytoplasm-to-pronucleus nanoinjections were performed under a variety of conditions to determine the effects of pulse magnitude and duration on zygote survival. Also, surviving embryos were transferred to surrogate females, and any developing embryos were examined for transgene integration and expression.

6.4.1 Device and Microprobe Preparation

Chips containing nanoinjector devices were fabricated using MEMSCAP Inc.'s polyMUMPs prototyping service [4]. On delivery the chips were coated in photoresist and have sacrificial phosphosilicate glass (PSG) layers. The photoresist and PSG were removed by soaking the chip in acetone, isopropyl alcohol, deionized water, and 47% hydrofluoric acid. This process both released and sterilized the nanoinjector. The released nanoinjector chip was bonded to the lid of a 3.5 cm culture dish with a doubled sided adhesive film and stored in deionized water prior to use.

During some of the initial experiments, large hydrogen bubbles (> 300 μm in diameter) formed on the submerged portion of the tungsten microprobe applying voltage to the nanoinjector. These bubbles would cause significant fluid flow when they moved to the liquid's surface, and cells coming into contact with these bubbles were observed to lyse within minutes of contacting the bubbles. To minimize the formation of hydrogen and oxygen bubbles during cytoplasm-to-pronuclear nanoinjection, a polymer coating was applied to the surface of the tungsten microprobes which applied voltage to the nanoinjector and the gold, on-chip return electrode.

The microprobes were dipped in a cyanoacrylate based polymer liquid and heat cured using a heat gun or the hot air above an alcohol flame. The coating process was repeated three to four times until an electrically insulating layer was formed (as verified by microprobe to microprobe contact measurements). The tip of each microprobe was exposed by abrasion against a rough surface. Prior to use, microprobes were soaked in 70% isopropyl alcohol.

6.4.2 Determination of the Electrolysis Voltage

Due to variations in the decomposition caused by oxidation of the nanoinjector, the voltage used for cytoplasm-to-pronucleus nanoinjection should be made based on the decomposition

voltage for the particular nanoinjector being used. However, determining the decomposition voltage using an IV curve, such as the one shown in Figure 6.5, requires multiple voltage-current measurements followed by mathematical post processing.

Rather than developing an IV curve for each device, the lowest voltage at which visible electrolysis occurs on the nanoinjector lance (E_o) was used as a benchmark for setting the nanoinjector's voltage. As shown in Figure 6.5, visible electrolysis on the nanoinjector lance occurs above the decomposition voltage. The absolute magnitudes of the pulses applied during nanoinjection are reported relative to E_o.

E_o was found by visual inspection with the microscope at 500x. An initial 50 ms pulse was applied well in excess of the anticipated E_o ($E_o + 5$ V for example) to nucleate bubbles on the nanoinjector lance. Once these bubbles had dissipated from the nanoinjector lance (typically in a matter of seconds), the pulse magnitude was reduced, and another 50 ms pulse applied. The process was repeated until the voltage at which electrolysis ceases on the lance is found to within 0.1 V. The lowest magnitude pulse causing visible electrolysis was taken as E_o.

6.4.3 Zygote Collection and Embryo Culture

Zygotes from super-ovulated CD1 or Swiss-Webster mice were harvested according to the procedures given in [51]. Cumulus masses dissected from the ovaduct were soaked in hyaluronidase in M2 media for up to two-minutes to release the cumulus cells from the zygotes. Zygotes were then washed in PBS and M2 before being placed in 40 μl droplets of KSOM media under silicone oil. Embryos were cultured in KSOM at 37 C and 5% CO_2.

6.4.4 Cytoplasm-to-Pronucleus Nanoinjection

Cytoplasm-to-pronucleus nanoinjections were performed with the nanoinjector submerged in 1.5–2 μl of room-temperature PBS. All nanoinjections were performed using a transgene encoding for enhanced green fluorescent protein (EGFP) with a chicken beta-actin promoter and SV-40 poly adenylation signal. Approximately 15-25 zygotes were placed on the nanoinjector chip at a time, and were allowed to remain on the chip for a maximum of 30 minutes. Care was taken to not leave groups of zygotes in the direct, straight-line conduction path between the nanoinjector

and the return electrode. During early experiments, zygotes placed directly between the nanoinjector and the return electrode lysed at a significantly higher rate than embryos not in the direct conduction path.

A typical nanoinjection cycle for a single zygote followed the process below (see also Figure 6.2):

- The nanoinjector was connected to the positive terminal of a 1.5 V source.
- The nanoinjector was elevated to its full out-of-plane elevation.
- 0.125–0.25 μl of DNA at 10–15 ng/μl were placed on the chip by a glass micropette attached to a microliter syringe pump.
- A zygote was placed in front of the nanoinjector, without aligning the pronucleus to the nanoinjector lance.
- The nanoinjector was actuated, translating in-plane until the lance penetrated 50—75% of the cell diameter into the cytoplasm.
- Electromechanical relays disconnected the 1.5 V source and connected the nanoinjector to the negative terminal of a voltage source that was x volts above (or for some experimental groups below) the electrolysis point (E_o). Duration of the voltage pulse of magnitude $E_o + x$ was on the millisecond-scale. See Table 6.2 for the voltage magnitudes and durations tested.
- Electromechanical relays connected the nanoinjector to the negative terminal of the $1.5V$ source.
- The nanoinjector lance was withdrawn from the cell, and the process repeated for each zygote injected.
- After 30 minutes (or when all zygotes had been injected) the zygotes were transferred to fresh KSOM droplets under silicone oil and cultured for 24 hours.

Untreated control zygotes, and zygotes which were on the nanoinjector chip during nanoinjections but not nanoinjected, were also cultured for 24 hours.

6.4.5 24-Hour Viability and Embryo Transfer

After 24 hours in culture the embryos in the untreated control, on-chip control, and injected groups were imaged by optical microscopy. The number of viable embryos (morphologically normal two or four-cell embryos) and lysed/arrested zygotes in each culture well were recorded. These results are presented in Table 6.2 and Figures 6.7 and 6.8. Injected embryos progressing to the two-cell stage were transferred into the oviducts of pseudo-pregnant female Swiss-Webster mice following the protocols outlined in [51].

6.4.6 Phenotype and Genotype Analysis of E9.5 Embryos and Deciduas

Post-implantation embryos and deciduas were harvested ten days post injection (the E9.5 embryonic phase). Each decidua, and embryo if one had developed, was dissected from the uterine lining and photographed using transmitted light and GFP filtered fluorescence microscopy. One half of each harvested decidua/embryo was homogenized in a stomacher bag filled with Hanks Balanced Salt Solution (HBSS) and analyzed by flow cytometry to provide a second method of GFP detection. PCR for the EGFP gene was performed on DNA extracted from the second half of each decidua/embryo harvested.

6.5 Results

Table 6.2 presents the 24-hour viability data for untreated control, on-chip control, and each combination of voltage magnitude and pulse duration tested. Figure 6.7(a) plots the 24-hour viability of each untreated control, on-chip control, and voltage magnitude group examined as an "x".

Assuming that the time duration tested within each voltage level did not have a significant impact allowed the data to be aggregated by control or voltage treatment. Figure 6.7(b) plots the mean and 95% standard deviation confidence intervals for the experimental replicates. There were no statistical differences between control groups or voltage levels.

The effect of pulse duration was not statistically significant for any voltage level. The greatest number of pulse durations were tested at $E_o + 1$ V. Figure 6.8 shows the 24-hour viability

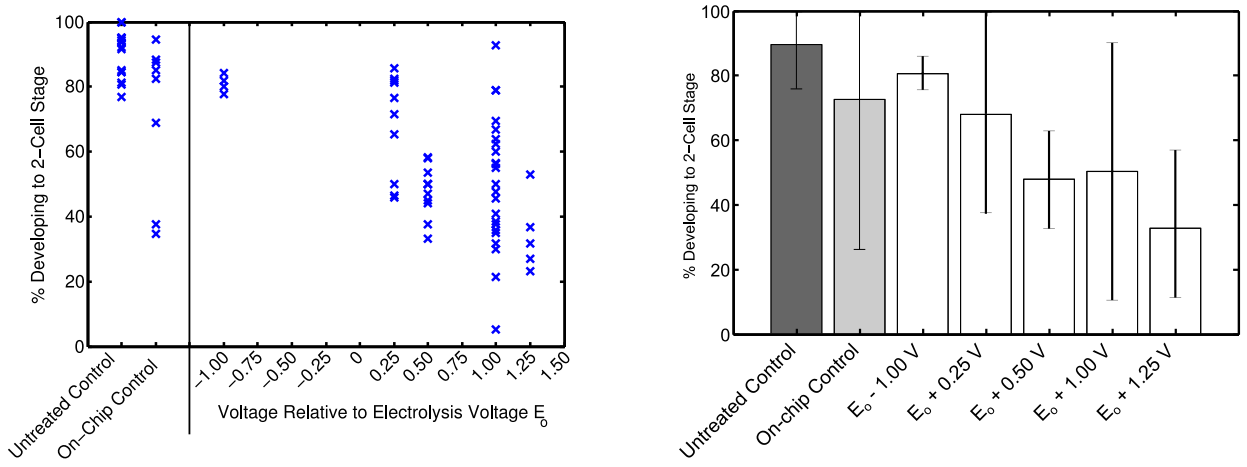

(a) Individual Experiments

(b) Aggregated Data

Figure 6.7: Proportion of cells progressing to the two-cell phase for untreated control, on-chip control, and nanoinjected embryos. (a) The proportion of two-cell embryos with each "x" corresponding to a replicate at the indicated voltage level. (b) Bar charts of the aggregated data at each voltage level. Error bars are 95% standard deviation confidence intervals. Error bars in excess of 100% are truncated to 100%. See Table 6.2 for the pulse durations tested at each voltage level.

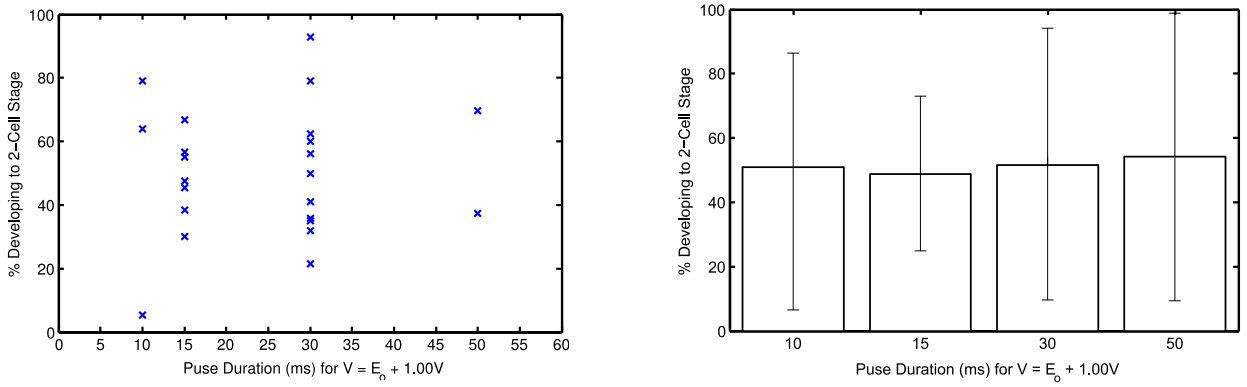

(a) Individual Experiments

(b) Aggregated Data

Figure 6.8: Proportion of cells progressing to the two-cell phase for nanoinjected zygotes at $E_o + 1$ V as a function of pulse duration. (a) The proportion of two-cell embryos with each "x" corresponding to a replicate at the indicated pulse duration level. (b) Bar charts of the aggregated data at each pulse duration level. Error bars are 95% standard deviation confidence intervals. See Table 6.2 for the pulse durations tested at each voltage level.

Table 6.2: Control and experimental groups used in testing cytoplasm-to-pronucleus nanoinjection. E_o indicates the electrolysis voltage as found using the protocol outlined above.

Group	Pulse Duration (ms)	2-Cell	Total	Percentage
Untreated Control	N/A	253	282	89.72%
On-Chip Control	N/A	120	165	72.73%
$E_o - 1.00$ V	50	34	42	80.95%
	10	37	46	80.43%
$E_o + 0.25$ V	30	144	212	67.92%
$E_o + 0.50$ V	30	102	205	49.76%
	20	9	27	33.33%
$E_o + 1.00$ V	50	22	39	56.41%
	30	82	165	49.70%
	15	69	140	49.29%
	10	31	63	50.79%
$E_o + 1.25$ V	15	29	81	35.80%
	10	6	26	23.08%

Table 6.3: Numbers of two-cell embryos transferred and embryos / deciduas harvested according to voltage pulse magnitude and duration. Note: embryos in the $E_o + 1.25$ V treatment were grouped together during transfers.

Voltage	Duration (ms)	2-Cell Embryos Transferred	Embryos / Deciduas Harvested
$E_o + 0.25$ V	30	67	8
$E_o + 0.50$ V	30	115	10
$E_o + 1.00$ V	50	18	5
$E_o + 1.00$ V	30	96	35
$E_o + 1.00$ V	15	67	28
$E_o + 1.25$ V	10 – 15	48	0
	Total	411	86

for individual replicates and the mean data at each pulse duration tested with a pulse magnitude of $E_o + 1$ V.

Table 6.3 gives the number of 2-cell embryos transferred and the number of deciduas harvested from each experiential treatment. Each of these embryos / deciduas were examined for

expression and integration of the EFGP transgene. All of the embryos or deciduas were negative for transgene expression by fluorescence microscopy and flow cytometry, and negative for transgene integration by PCR.

6.6 Discussion of Results

As expected, Figure 6.7 shows a negative correlation between applied voltage and embryo viability. The highest aggregate viability among injected cells occurred among those injected at 1.00 V below the electrolysis point. The lowest viability was for those injected 1.25 V above electrolysis. This result agrees with the experimental observation that the formation of hydrogen bubbles on the lance, and especially within the zygote, was correlated with higher cell mortality.

However, looking only at the aggregate data (Figure 6.7(b)) it would appear that there are inconsistencies in this general, predicted trend. For example, the non-injected on-chip control group had lower aggregate viability than the $E_o - 1.00$ V group, and the $E_o - 0.50$ V had lower viability than the $E_o + 1.00$ V group. These results can be explained by the variability within each experimental group as shown in Figure 6.7(a), and as quantified by the confidence intervals in Figure 6.7(b). This variability was partly due to identification and remediation of harmful phenomena observed during the development of this new process. For example, on-chip control zygotes placed in the direct current path between the nanoinjector and the return electrode had a high rate of lysis. Low viability in these cells led to guidelines for cell placement on the nanoinjector chip, which remedied that source of cell lysis.

Though not statistically significant, the data shown in Figure 6.8(a) suggests that deceasing pulse duration may have a positive effect on embryo viability. Again, there is significant scatter in the data collected at each pulse duration which clouds the quantitative interpretation of the data. This scatter is largely due to damaging conditions at voltages above electrolysis. For example, during nanoinjections at $E_o + 1.00$ V, 10 ms, very low survival was observed for a group of nanoinjected zygotes (5.3%) placed in close proximity to the bubbles on the tungsten microprobe connected to the nanoinjector. During the same day's experiments, a group of identically nanoinjected zygotes cells maintained far from the tungsten microprobe had much better viability (79.0%). Based on this observation, insulating cyanoacrylate was applied to the tungsten microprobes to reduce bubble formation.

It was repeatedly observed throughout the $E_o + 1.00$ V experiments, that the formation of bubbles on the lance and within the cell is a strong predictor of cell lysis. Though the formation of hydrogen bubbles on the lance may not be the mechanism for cell death, it may be helpful as a physical indication of damaging electric fields and currents. It was observed that for a given voltage, decreasing pulse duration decreases the size and number of hydrogen bubbles formed on the lance tip. Though not statistically significant, the limited number of data points at 10 and 15 ms seem to indicate that decreasing pulse duration increases post injection survival.

Embryos which have been exposed to voltages in excess of the electrolysis voltage have developed into post-implantation embryos. To date, no embryos or deciduas have exhibited transgene integration or expression. The rate of transgene integration following localized electroporation is not known, and may be lower than that for other transgenic methods. Additionally, no deciduas have been examined from the highest voltage yet tested ($E_o + 1.25$ V), which, according to the modeling and literature, should be the most promising group. It is not clear if the absence of post-implantation development in this group is a result of embryo damage, or simply a result of the delicate nature of embryo transfer.

6.7 Conclusion and Recommendations

Thus far, research on localized electrophoresis of mouse zygotes has led to the development of hardware and protocols which allow zygotes to survive electric fields and electrolytic products generated during cytoplasm-to-pronucleus nanoinjection. Additionally, cytoplasmically nanoinjected zygotes have developed into post-implantation embryos. The presented data indicate that applied voltage has a statistically significant effect on embryo survival. Qualitative examination of the data and experiential observations suggest that decreasing pulse duration likely also has a positive effect on embryo survival.

The work presented here poses two important questions for future research. First, how can the cytoplasm-to-pronucleus nanoinjection process be made more consistent? Much effort has already been expended to answer this question, and further careful experimentation will help improve the consistency of the process. For example, while PBS has been shown to be adequate for pronuclear nanoinjection below the decomposition voltage, the literature suggests other media, such as HEPES-buffered saline, may help improve viability during electroporation [76].

Second, can zygotes survive greater pulse magnitudes if the duration of the pulse is sufficiently short? The longer, single pulses employed in this research were motivated by the mathematical modeling results presented above. The literature on electroporation documents the use of multiple short pulses (1 ms or less) rather than a single longer pulse [76], [159]. This practice may help prevent irreversible pore formation and cell lysis and increase post-injection viability [153].

CHAPTER 7. CONCLUSIONS AND RECOMMENDATIONS

7.1 Conclusions and Contributions

Taken as a whole, the research described in this dissertation demonstrates that localized electrical accumulation and release of DNA molecules by MEMS, coupled with precise mechanical penetration of cellular membranes by MEMS devices, can result in genomic integration of exogenous DNA. Electrophysical injection of DNA is made feasible by MEMS' capacity for nanoscale feature sizes, complex mechanical motion, and electrical interaction with their surrounding media.

Rigid-body, compliant, and metamorphic mechanism design techniques were applied to produce the nanoinjector lance mechanism's unique self-reconfiguring metamorphic motion. This metamorphic motion was instrumental to allowing the nanoinjector to be fabricated with existing thin-film, surface-micromachining processes. The thin-film processing allowed the lance to be on the order of 1 μm thick, and only tens of nanometers wide. Rigid-body, compliant, and metamorphic mechanism design allowed these thin layers of material to raise out–of-plane, then to penetrate the lance into a mouse zygote all while consistently causing minimal damage to the injected zygotes. The nanoinjector's self-reconfiguration though the variable stiffness of its sub-phases can be applied to design other rigid-link or compliant self-reconfiguring metamorphic mechanisms.

Pronuclear nanoinjection successfully coupled the nanoinjector's unique motion with electrical accumulation and release of DNA to produce transgenic mice. Nanoinjection demonstrated higher rates of in-vitro (two-cell development) and gestational viability, when compared to a pronuclear microinjection positive control. Higher post-injection viability resulted in fewer zygotes, injections, and surrogate mothers being required to produce each transgenic mouse. The higher viability in the nanoinjected zygotes may be the result of the lance's fine features, and nanoinjection's non-fluidic method of gene transfer.

Since the completion of the nanoinjection experiments reported in Chapter 3, one other graduate student and one part time lab technician have been trained to perform pronuclear and cytoplasm to pronucleus nanoinjection. Even though neither user had previous MEMS operation or microinjection experience, both achieved rates of zygotic viability similar to those reported in Chapter 3 after approximately 6–8 nanoinjection sessions. In comparison, individuals can require up to 6 months of training to become proficient at pronuclear microinjection. This anecdotal evidence suggests that nanoinjection can be learned quickly by users with little previous experience in MEMS operation or microinjection. The lance's constrained movement, the simplicity of the on-chip manipulations, and the minimal trauma caused by the nanoinjection process all likely contribute to the ease of learning nanoinjection.

Nanoinjection represents a fundamentally new method of macromolecule transfer. Further refinement and commercialization of the nanoinjection concept will allow for the use of nanoinjection in many important scientific studies. Pronuclear nanoinjection has the possibility to increase the efficiency of transgenic animal production.

Throughout the nanoinjector's design and testing, it was observed that the precision of the mechanism's motion could be increased if the parasitic motion in the rigid-link MEMS joints were eliminated. This could be achieved by the development of a fully compliant lamina emergent mechanism (LEM) nanoinjector. However, the design of compliant LEMs necessitated the development and evaluation of methods for modeling the compliant members. To this end, the minimum potential energy method (MinPE method) was developed for analyzing underactuated pseudo-rigid-body models of compliant mechanisms. Unlike existing analytical methods, which require lengthy derivations for each new topology analyzed, the MinPE method can be rapidly implemented to evaluate new design topologies. Additionally, because of its simple implementation, the MinPE method could be rapidly adopted and applied in a variety of fields which commonly deal with underactuated or underconstrained compliant mechanisms.

Finite element modeling is a crucial, and often time consuming step in the design of any compliant MEMS device, such as a fully compliant nanoinjector. However, the literature provides little guidance on the proper selection of finite element types to analyze geometrically non-linear deflections of thin film MEMS devices. Because thin-film mechanisms may have in-plane features which are many times larger than their out-of plane thicknesses, shell finite elements are an appeal-

ing option to decrease the computational effort required to model such mechanisms. A quantitative, performance-based comparison of 3-D and shell finite elements in models of prototype compliant nanoinjectors was conducted to determine if shell elements can be applied to combined loading of thin-film devices. The analyses showed that shell elements are more computationally efficient than 3-D elements while still providing essentially the same force, displacement, and stress results. Shell finite element models may be useful not only in modeling thin-film compliant MEMS, but also other thin-film compliant members and mechanisms, such as LEMS.

Finally, this research has taken initial steps in exploring the feasibility of cytoplasm-to-pronucleus nanoinjection. Increasing the lance's voltage above the decomposition voltage would allow for electrophoresis of DNA and may cause pore formation in phospho-lipid membranes near the lance. The electric field generated by the lance could cause electroporation of the pronuclear membrane and electrophoresis of DNA into the pronucleus, making the injection process insensitive to the pronuclei's visibility, location or size. Preliminary studies demonstrate that the zygotes are able to survive nanoinjection voltage pulses which are theoretically sufficient to cause electroporation and electrophoresis. However, the in-vitro and gestational viability of cytoplasm-to-pronucleus nanoinjected embryos was highly variable in these preliminary studies. To date, no integrated or expressing embryos have been produced from cytoplasm-to-pronucleus nanoinjected embryos. However, the small number of embryos evaluated do not include any embryos at the higher voltages which have the greatest possibility of producing successful electroporation. If successful, cytoplasm-to-pronucleus nanoinjection will be a new and potentially robust method of gene transfer.

7.2 Recommendations

Research on pronuclear nanoinjection, compliant LEM design, and cytoplasm-to-pronucleus nanoinjection is ongoing. This dissertation represents the initial steps in what will hopefully become valuable and applied areas of research. Some recommendations for continuation or extension of nanoinjection and compliant mechanism research are organized below by topic.

7.2.1 Extensions and Refinements of Pronuclear or Low-Voltage Nanoinjection

To date, the transgenes transferred using pronuclear nanoinjection have been on the order of 3 kilobases in length. It is very likely that genetic constructs of other sizes can also be transported across cell membranes via nanoinjection. For example, siRNA could be nanoinjected into zygotes with the existing nanoinjector. Additionally, a modified lance, or lances, could inject siRNA into other cell types. Nanoinjection may also work for the transport of much larger DNA, such as yeast artificial chromosomes (YACs). Large constructs would likely experience little damage during nanoinjection because there is no fluid flow to shear these larger molecules. Low-voltage nanoinjection may find application injecting other charged molecules such as proteins or drugs into cells.

The nanoinjector protocol described in this dissertation has not yet been optimized. The DNA concentrations, injection duration, and on-chip injection media are known to work, but more efficient and consistent options may exist. More efficient and consistent gene transfer may be achieved by increasing the concentration or volume of DNA solution placed around the lance before each injection. Likewise, the DNA concentrations and volumes used in these studies may have been excessive, and reducing either may reduce the amount of DNA to be prepped for each nanoinjection. More control over the number of transgene copies accumulated on the lance may be possible through a compromise between electrophoretic attraction of DNA to the lance and lance oxidation. For example, a protocol may be devised whereby short voltage pulses above the decomposition voltage allow for 50–100 attraction and release cycles before the lance becomes too oxidized to use. Additionally, the time to release DNA in the pronucleus is not yet optimized, and is likely excessive given the short time (milliseconds) required to fully charge the lance. Finally, changes to the injection conditions, such as injection media may have an impact on nanoinjection efficiency. For example, an injection media which allows for super-coiling of DNA prior to injection could increase the size of DNA particles which can be nanoinjected.

7.2.2 Nanoinjector Design

The nanoinjector mechanism has proven to be a useful research prototype over the course of thousands of injections. A chip-based nanoinjection system could be improved by increased precision in the nanoinjector's motion through the exclusive use of compliant joints.

If nanoinjection is to be adopted by other researchers, the barriers to adopting this process should be minimized. One of the greatest barriers to adoption of the on-chip nanoinjector mechanism is the opaque silicon substrate used to fabricate the nanoinjector. Conventional microinjection systems use inverted microscopes, necessitating a clear view from below. One option would be to fabricate a nanoinjector on a transparent substrate. Fabricating polycrystalline silicon MEMS on a transparent substrate poses several technical challenges, and could require an exotic substrate (single crystal sapphire for example).

Another approach would be to develop a stand-alone lance, which is fitted to an existing microinjection system micromanipulator. Ideally, a stand-alone lance would also exploit the polycrystalline silicon MEMS fabrication technologies which have produced the the current nanoinjector's nano-featured lances. The sand-alone lance should also be compatible with existing inverted microscopes and micromanipulators. Figure 7.1 shows a one concept for what such a stand-alone lance may look like. Coupling the highly refined microinjection station optics and manipulator with a nanoinjector lance could lead to new applications for the nanoinjector, such as the selective nanoinjection of individual blastomeres within a developing embryo.

7.2.3 Compliant Mechanism Design and Modeling Techniques

The MinPE method has the potential to be expanded into a powerful, flexible analysis method for compliant mechanisms. Through the application of appropriate non-linear constraints, complex phenomena, such as contact boundary conditions, could be incorporated into underactuated and underconstrained pseudo-rigid-body models.

7.2.4 Cytoplasm-to-Pronucleus Nanoinjection via Localized Electroporation

Cytoplasm-to-pronucleus nanoinjection via localized electroporation has the greatest potential for simplifying the generation of transgenic animals. However, the wide variability in the

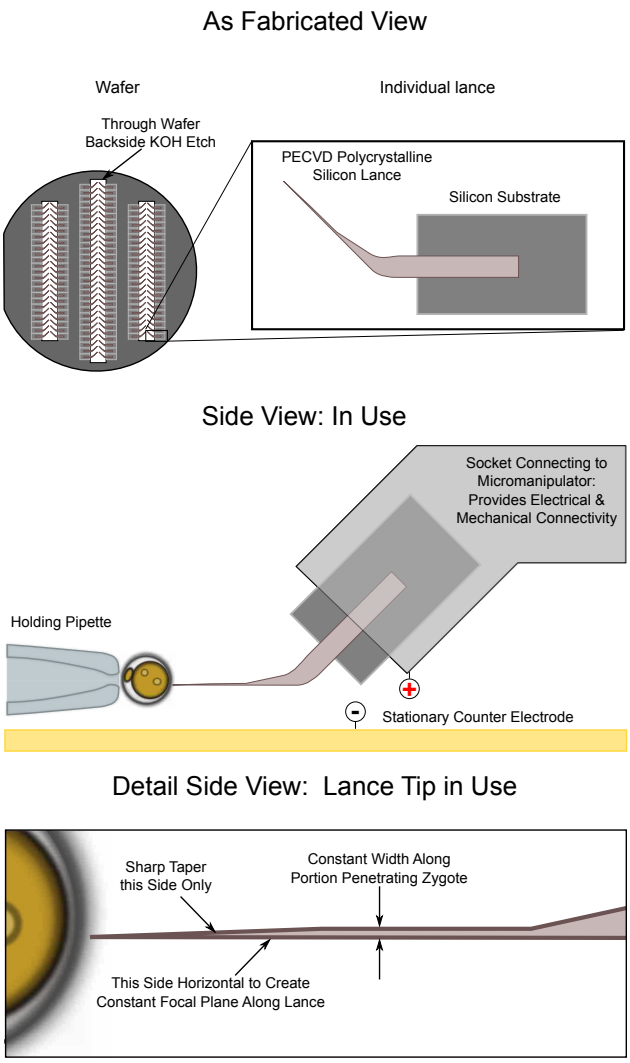

Figure 7.1: Illustration of a concept for a stand-alone nanoinjection lance.

preliminary data presented thus far suggests that the process is still not under control. Research on cytoplasm-to-pronucleus nanoinjection should continue because of its potential to facilitate genetic modification of scientifically important animals which are currently difficult to transfect. For example, many large mammals, such as goats, pigs, and cattle, have opaque cytoplasms, making their pronuclei difficult to visualize and microinject. Additionally, the zygotes of other animals, such as rats, are more delicate than those of mice, again making them more difficult to microinject.

Individual experiential replicates using non-optimized protocols have demonstrated two-cell development rates greater than 50%, with some experimental groups having even higher viability rates. With further refinements of injection media, voltage pulse magnitude, duration, and

number of pulses, the viability of embryos surviving localized electroporation may be higher. Additionally, the lance could be modified to concentrate or restrict the electric field to a much smaller region. This could be accomplished by insulating all but the very tip of the nanoinjector lance.

Maintaining acceptable embryo viability, however, is only a first step in developing a cytoplasm-to-pronucleus nanoinjection via localized electroporation into a practical method of transgenesis. The method will only work if electropores open in the pronuclear membranes, and if the transgene can move through those pores. Experiments may be conducted to verify that electroporation of the pronuclear membranes is occurring. For example, a dyed solution could be injected into the pronucleus, then cytoplasm to pronuclear nanoinjection performed on the zygote. Leakage of the dye into the pronucleus would indicate successful electroporation. A more direct approach would be to attempt cytoplasm-to-pronucleus nanoinjection of a reporter transgene into a large numbers of eggs in study similar to that reported in Chapter 3.

7.2.5 Automation

Looking beyond the current prototypes and protocols, nanoinjection may enable partial or complete automation of transgene delivery into zygotes. A fully automated nanoinjection system would need to perform both the zygote manipulations (pick, orient, and place) and the nanoinjection process (accumulate DNA, penetration into the zygote, release DNA). Computer vision systems and computer controlled micromanipulators are currently available which can position a zygote using a holding pipette, and which could drive the lance to a location within the zygote. Systems can be envisioned which would use either an on-chip nanoinjector or a standalone lance nanoinjector.

If it is demonstrated to efficiently transfect zygotes, cytoplasm-to-pronucleus nanoinjection would be the first choice for completely automated nanoinjection. Cytoplasm-to-pronucleus nanoinjection would be insensitive to the position of the lance relative to the pronuclei within the zygote. The automation system would only have to pick up the zygote, and perform the injection with the lance penetrating a certain depth into the zygote.

Pronuclear nanoinjection would be more challenging to automate because it requires alignment of the lance with the zygote's pronucleus. Optimally, the system would orient the zygote such that the lance and the holding pipette are colinear, as in Figure 7.2(a). However, develop-

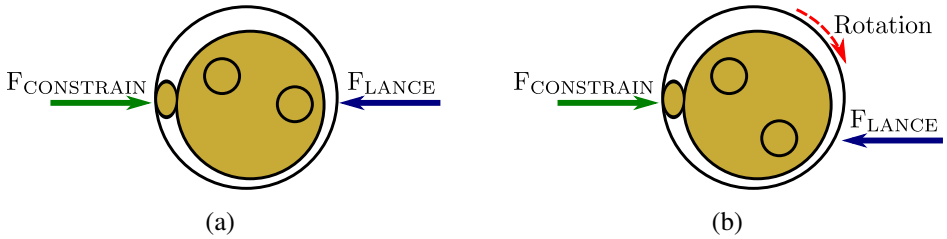

Figure 7.2: Effects of zygote orientation on cell rotation during injection. (a) Colinear forces applied by the lance and the holding pipette (or other constraint) do not cause rotation. (b) Non-colinear forces result in rotation and tearing of the cell membranes.

ing a pipette based placement system that can achieve such precise orientation of the pronucleus in three-dimensional space may prove quite challenging. Other cell positioning tools may be required to automate this orientation process, or more robust restraints may be needed to prevent the rotation illustrated in Figure 7.2(b). There is a possibility that the forces generated by nanoinjection are small enough, and that a holding pipette's resistance to zygote rotation is great enough, to allow for off-center nanoinjection, as illustrated in Figure 7.2(b). In that case, a stand-alone lance and a standard holding pipette may provide the initial tools for automated pronuclear nanoinjection.

REFERENCES

[1] Q. T. Aten, "Design and testing of a pumpless microelectromechanical system nanoinjector," Master's thesis, Brigham Young University, 2008.

[2] L. Howell, *Compliant Mechanisms*. New York: Wiley, 2001.

[3] J. S. Dai and J. Jones, "Mobility in metamorphic mechanisms of foldable/erectable kinds," *Journal of Mechanical Design*, vol. 121, no. 3, p. 375, September 1999.

[4] J. Carter, A. Cowen, B. Hardy, R. Mahadevan, M. Stonefield, and S. Wilcenski, *PolyMUMPs Design Handbook Revision 11*, MEMSCAP Inc., 2005. [Online]. Available: http://www.memscap.com/en_mumps.html

[5] J. W. Gordon, G. A. Scangos, D. J. Plotkin, J. A. Barbosa, and F. H. Ruddle, "Genetic transformation of mouse embryos by microinjection of purified DNA," *Proceedings of the National Academy of Science*, vol. 77, no. 12, pp. 7380–7384, December 1980.

[6] R. Brinster, H. Chen, M. Trumbauer, A. Senear, R. Warren, and R. Palmiter, "Somatic expression of herpes thymidine kinase in mice following injection of a fusion gene into eggs," *Cell*, vol. 27, no. 1 Part 2, pp. 223–231, November 1981.

[7] G. Rubin and A. Spradling, "Genetic transformation of drosophila with transposable element vectors," *Science*, vol. 218, no. 4570, pp. 348–353, October 1982.

[8] K. Desai, N. Xiao, W. Wang, L. Gangi, J. Greene, J. Powell, R. Dickson, P. Furth, K. Hunter, R. Kucherlapati *et al.*, "Initiating oncogenic event determines gene-expression patterns of human breast cancer models," *Proceedings of the National Academy of Sciences*, vol. 99, no. 10, pp. 6967–6972, May 2002.

[9] C. Kavanaugh, K. Desai, A. Calvo, P. Brown, C. Couldrey, R. Lubet, and J. Green, "Preclinical applications of transgenic mouse mammary cancer models," *Transgenic Research*, vol. 11, no. 6, pp. 617–633, December 2002.

[10] K. Schwertfeger, W. Xian, A. Kaplan, S. Burnett, D. Cohen, and J. Rosen, "A critical role for the inflammatory response in a mouse model of preneoplastic progression," *Cancer Research*, vol. 66, no. 11, pp. 5676–5685, June 2006.

[11] D. Langenau, M. Keefe, N. Storer, C. Jette, A. Smith, C. Ceol, C. Bourque, A. Look, and L. Zon, "Co-injection strategies to modify radiation sensitivity and tumor initiation in transgenic zebrafish," *Oncogene*, vol. 27, no. 30, p. 4242, July 2008.

[12] H. Song, K. Shahverdi, D. Huso, Y. Wang, J. Fox, R. Hobbs, B. Gimi, K. Gabrielson, M. Pomper, B. Tsui *et al.*, "An immunotolerant HER-2/neu transgenic mouse model of

metastatic breast cancer," *Clinical Cancer Research*, vol. 14, no. 19, pp. 6116–6124, October 2008.

[13] L. J. McCawley, J. Wright, B. J. LaFleur, H. C. Crawford, and L. M. M. Matrisian, "Keratinocyte expression of MMP3 enhances differentiation and prevents tumor establishment," *American Journal of Pathology*, vol. 173, no. 5, pp. 1528–1533, November 2008.

[14] R. Tomasini, K. Tsuchihara, M. Wilhelm, M. Fujitani, A. Rufini, C. C. Cheung, F. Khan, A. Itie-Youten, A. Wakeham, M.-s. Tsao, J. L. Iovanna, J. Squire, I. Jurisica, D. Kaplan, G. Melino, A. Jurisicova, and T. W. Mak, "TAp73 knockout shows genomic instability with infertility and tumor suppressor functions," *Genes & Development*, vol. 22, no. 19, pp. 2677–2691, October 2008.

[15] K. Sasai, J. Parant, M. Brandt, J. Carter, H. Adams, S. Stass, A. Killary, H. Katayama, and S. Sen, "Targeted disruption of aurora A causes abnormal mitotic spindle assembly, chromosome misalignment and embryonic lethality," *Oncogene*, vol. 27, no. 29, pp. 4122–4127, July 2008.

[16] S. Burnett, E. Kershen, J. Zhang, L. Zeng, S. Straley, A. Kaplan, and D. Cohen, "Conditional macrophage ablation in transgenic mice expressing a Fas-based suicide gene," *Journal of Leukocyte Biology*, vol. 75, no. 4, pp. 612–623, 2004.

[17] A. Philipovskiy, C. Cowan, C. Wulff-Strobel, S. Burnett, E. Kerschen, D. Cohen, A. Kaplan, and S. Straley, "Antibody against V antigen prevents Yop-dependent growth of Yersinia pestis," *Infection and Immunity*, vol. 73, no. 3, pp. 1532–1542, March 2005.

[18] Y. Carrier, J. Yuan, V. K. Kuchroo, and H. L. Weiner, "Th3 cells in peripheral tolerance. I. induction of Foxp3-positive regulatory T cells by Th3 cells derived from TGF-β T cell-transgenic mice," *Journal of Immunology*, vol. 178, pp. 179–185, 2007.

[19] K. Hochweller, J. Striegler, G. J. Hämmerling, and N. Garbi, "A novel CD11c. DTR transgenic mouse for depletion of dendritic cells reveals their requirement for homeostatic proliferation of natural killer cells," *Eur. J. Immunol*, vol. 38, no. 10, pp. 2776–2783, October 2008.

[20] R. S. Schmid, Y. Yokota, and E. S. Anton, "Generation and characterization of brain lipid-binding protein promoter-based transgenic mouse models for the study of radial glia," *Glia*, vol. 53, no. 4, pp. 345–351, March 2006.

[21] L. M. Billings, S. Oddo, K. N. Green, J. L. McGaugh, and F. M. LaFerla, "Intraneuronal aβ causes the onset of early Alzheimer's disease-related cognitive deficits in transgenic mice," *Neuron*, vol. 45, no. 5, pp. 675–688, March 2005.

[22] C. Liu, *Foundations of MEMS*. Pearson Education, 2006.

[23] N. Hubbard and L. Howell, "Design and characterization of a dual-stage, thermally actuated nanopositioner," *Journal of Micromechanics and Microengineering*, vol. 15, no. 8, pp. 1482–1493, 2005.

[24] R. K. Messenger, Q. T. Aten, T. W. McLain, and L. L. Howell, "Piezoresistive feedback control of a mems thermal actuator," *Journal of microelectromechanical systems*, vol. 18, no. 6, pp. 1267–1278, December 2009.

[25] K. A. Jensen, C. P. Lusk, and L. L. Howell, "An XYZ micromanipulator with three translational degrees of freedom," *Robotica*, vol. 24, no. 3, pp. 305–314, May 2006.

[26] C. Mastrangelo, M. Burns, and D. Burke, "Microfabricated devices for genetic diagnostics," *Proceedings of the IEEE*, vol. 86, no. 8, pp. 1769–1787, August 1998.

[27] S. Parng, T. Shia, H. Yang, and C. Kuo, "DNA extraction with parallel electrodes on microfluidic system," in *NSTI Nanotech 2006 Technical Proceedings*, vol. 2, 2006, pp. 625–628.

[28] O. Bruckman, G. Jullien, M. Ahmadi *et al.*, "A MEMS DNA replicator and sample manipulator," *Circuits and Systems*, vol. 2, pp. 2000–2008, 2000.

[29] X. Chen, D. Cui, C. Liu, and H. Li, "Fabrication of DNA purification microchip integrated with mesoporous matrix based on MEMS technology," *Microsystem Technologies*, vol. 14, no. 1, pp. 51–57, August 2008.

[30] E. W. Jager, O. Inganas, and I. Lundstrom, "Microrobots for micrometer-size objects in aqueous meida: Potential tools for single-cell manipulation," *Science*, vol. 288, pp. 2335–38, 2000.

[31] H. Chan and W. Li, "A thermally actuated polymer micro robotic gripper for manipulation of biological cells," *Robotics and Automation, 2003. Proceedings. ICRA'03. IEEE International Conference on*, vol. 1, pp. 288–293, September 2003.

[32] N. Chronis and L. Lee, "Electrothermally activated SU-8 microgripper for single cell manipulation in solution," *Microelectromechanical Systems, Journal of*, vol. 14, no. 4, pp. 857–863, 2005.

[33] F. Beyeler, A. Neild, S. Oberti, D. Bell, Y. Sun, J. Dual, and B. Nelson, "Monolithically fabricated microgripper with integrated force sensor for manipulating microobjects and biological cells aligned in an ultrasonic field," *Microelectromechanical Systems, Journal of*, vol. 16, no. 1, pp. 7–15, 2007.

[34] K. Kim, X. Liu, Y. Zhang, and Y. Sun, "Nanonewton force-controlled manipulation of biological cells using a monolithic MEMS microgripper with two-axis force feedback," *Journal of Micromechanics and Microengineering*, vol. 18, no. 5, p. 55013, April 2008.

[35] H. Matsuoka, T. Komazaki, Y. Mukai, M. Shibusawa, H. Akane, A. Chaki, N. Uetake, and M. Saito, "High throughput easy microinjection with a single-cell manipulation supporting robot," *Journal of Biotechnology*, vol. 116, no. 2, pp. 185–194, March 2005.

[36] X. Liu, K. Kim, Y. Zhang, and Y. Sun, "Nanonewton force sensing and control in microrobotic cell manipulation," *The International Journal of Robotics Research*, vol. 28, no. 8, pp. 1065–1076, August 2009.

[37] W. Chang, C. Keller, and D. Sretavan, "Precision mems nano-cutting device for cellular microsurgery," *ASME Intl. Mechanical Engineering Congress (IMECE2004-61670)*, vol. 1, pp. 1–6, 2004.

[38] S. Zappe, M. Fish, M. Scott, and O. Solgaard, "Automated MEMS-based drosophila embryo injection system for high-throughput RNAi screens," *Lab on a Chip*, vol. 6, pp. 1012–1019, 2006.

[39] W. Wang, X. Liu, D. Gelinas, B. Ciruna, and Y. Sun, "A fully automated robotic system for microinjection of zebrafish embryos," *PLoS ONE*, vol. 2, no. 9, p. e862, September 2007.

[40] S.-W. Han, C. Nakamura, N. Kotobuki, I. Obataya, H. Ohgushi, T. Nagamune, and J. Miyake, "High-efficiency DNA injection into a single human mesenchymal stem cell using a nanoneedle and atomic force microscopy," *Nanomedicine: Nanotechnology, Biology, and Medicine*, vol. 4, no. 3, pp. 215—225, September 2008.

[41] Q. T. Aten, B. D. Jensen, and S. H. Burnett, "Testing of a pumpless MEMS microinjection needle employing electrostatic attraction and repulsion of DNA," in *2008 Proceedings of the ASME International Design Engineering Technical Conferences and Computers and Information in Engineering Conference, DETC2008*, 2008.

[42] T. E. McKnight, A. V. Melechko, G. D. Griffin, M. A. Guillorn, V. I. Merkulov, F. Serna, D. K. Hensley, M. J. Doktycz, D. H. Lowndes, and M. L. Simpson, "Intracellular integration of synthetic nanostructures with viable cells for controlled biochemical manipulation," *Nanotechnology*, vol. 14, pp. 551–556, April 2003.

[43] D. G. J. Mann, T. E. McKnight, J. T. McPherson, P. R. Hoyt, A. V. Melechko, M. L. Simpson, and G. S. Sayler, "Inducible RNA interference-mediated gene silencing using nanostructured gene delivery arrays," *ASCNano*, vol. 2, no. 1, pp. 69–76, January 2007.

[44] A. Pillarisetti, M. Pekarev, A. D. Brooks, and J. P. Desai, "Evaluating the role of force feedback for biomanipulation tasks," *Proc Symposium on Haptic Interfaces for Virtual Environment and Teleoperator Systems*, vol. 1, pp. 11–18, 2006.

[45] T. Hamada, H. Sasaki, R. Seki, and Y. Sakaki, "Mechanism of chromosomal integration of transgenes in microinjected mouse eggs: sequence analysis of genome-transgene and transgene-transgene junctions at two loci," *Gene*, vol. 128, no. 2, pp. 197–202, June 1993.

[46] H. Würtele, K. C. E. Little, and P. Chartran, "Illegitimate DNA integration in mammalian cells," *Gene Therapy*, vol. 10, no. 21, pp. 1791–1799, October 2003.

[47] K. M. Pawlik, C.-W. Sun, N. P. Higgins, and T. M. Townes, "End joining of genomic DNA and transgene DNA in fertilized mouse eggs," *Gene*, vol. 165, no. 2, pp. 173–181, 1995.

[48] G. Dellaire and P. Chartrand, "Direct evidence that transgene integration is random in murine cells, implying that naturally occurring double-strand breaks may be distributed similarly within the genome," *Radiation Research*, vol. 149, no. 4, pp. 325–329, April 1998.

[49] K. Chida, R. Sueyoshi, and T. Kuroki, "Efficient and stable gene transfer following microinjection into nuclei of synchronized animal cells progressing from G1/S boundary to

early S phase," *Biochemical and Biophysical Research Communications*, vol. 249, no. 2, pp. 849–852, August 1998.

[50] A. W. Chan, G. Kukolj, A. M. Skalka, and R. D. Bremel, "Timing of DNA integration, transgenic mosaicism, and pronuclear microinjection," *Molecular Reproduction and Development*, vol. 52, no. 4, pp. 406–413, April 1999.

[51] A. Nagy, M. Gertsenstein, K. Vintersten, and R. Behringer, *Manipulating the Mouse Embryo: A Laboratory Manual*, 3rd ed. Cold Spring Harbor Laboraatory Press, 2003.

[52] R. L. Brinster, H. Y. Chen, M. E. Trumbauer, M. K. Yagle, and R. D. Palmiter, "Factors affecting the efficiency of introducing foreign DNA into mice by microinjecting eggs," *Proceedings of the National Academy of Sciences of the United States of America*, vol. 82, no. 13, pp. 4438–4442, July 1985.

[53] M. A. Matzke, M. F. Mette, and A. J. M. Matzke, "Transgene silencing by the host genome defense: implications for the evolution of epigenetic control mechanisms in plants and vertebrates," *Plant Molecular Biology*, vol. 43, no. 2-3, pp. 401–415, June 2000.

[54] J. B. Buck, "A versatile microinjection and micropipetting syringe," *Review of Scientific Instruments*, vol. 20, no. 9, pp. 676–677, September 1949.

[55] R. Moricard and C. Chi, "Study of mitogenetic function of follicular fluid by intrafollicular microinjection of hormones in the rabbit," *Journal de Physiologie*, vol. 43, no. 4, pp. 819–820, 1951.

[56] J. Brachet, T. Kuusi, and S. Gothie, "Comparative study of the inductive power of nucleic acids and of cellular nucleoproteins when they are implanted or given by microinjection," *Archives de Biologie*, vol. 63, no. 4, pp. 429–440, 1952.

[57] R. J. Wall, "Pronuclear microinjection," *Cloning and Stem Cells*, vol. 3, no. 4, pp. 209–220, December 2001.

[58] Y. Zhang and L. Yu, "Single-cell microinjection technology in cell biology," *Bioessays*, vol. 30, no. 6, pp. 606–10, June 2008.

[59] P. Wong, U. Ulmanella, and C. Ho, "Fabrication process of microsurgical tools for single-cell trapping and intracytoplasmic injection," *Microelectromechanical Systems, Journal of*, vol. 13, no. 6, pp. 940–946, December 2004.

[60] T. A. Steward, E. F. Wagner, and M. B., "Human beta-globin gene sequences injected into mouse eggs, retained in adults, and transmitted to progeny," *Science*, vol. 217, no. 4564, pp. 1046–1048, 1982.

[61] G. Stuart, J. McMurray, and M. Westerfield, "Replication, integration and stable germ-line transmission of foreign sequences injected into early zebrafish embryos," *Development*, vol. 103, no. 2, pp. 403–412, 1988.

[62] R. J. Wall, V. G. Pursel, R. E. Hammer, and R. L. Brinster, "Development of porcine ova that were centrifuged to permit visualization of pronuclei and nuclei," *Biology of Reproduction*, vol. 23, no. 3, pp. 645–651, April 1985.

[63] H. Baldassarre, B. Wang, N. Kafidi, M. Gauthier, N. Neveu, J. Lapointe, L. Sneek, M. Leduc, F. Duguay, J. F. Zhou, A. Lazaris, and C. N. Karatzas, "Production of transgenic goats by pronuclear microinjection of in vitro produced zygotes derived from oocytes recovered by laparoscopy," *Theriogenology*, vol. 59, no. 3-4, pp. 831–839, February 2003.

[64] T. Takada, K. lida, T. Awaji, K. Itoh, R. Takahashi, A. Shibui, K. Yoshida, S. Sugano, and G. Tsujimoto, "Selective production of transgenic mice using green fluorescent protein as a marker," *Nature Biotechnology*, vol. 15, no. 5, pp. 458–461, May 1997.

[65] M. Kato, K. Yamanouchi, M. Ikawa, M. Okabe, K. Naito, and H. Tojo, "Efficient selection of transgenic mouse embryos using EGFP as a marker gene," *Molecular Reproduction and Development*, vol. 54, no. 1, pp. 43–48, September 1999.

[66] Y. Yamauchi, B. Doe, A. Ajduk, and M. Ward, "Genomic DNA damage in mouse transgenesis," *Biology of Reproduction*, vol. 77, no. 3, pp. 803–812, November 2007.

[67] A. C. F. Perry, T. Wakayama, H. Kishikawa, T. Kasai, M. Okabe, Y. Toyoda, and R. Yanagimachi, "Mammalian transgenesis by intracytoplasmic sperm injection," *Science*, vol. 284, no. 5417, pp. 1180–1183, May 1999.

[68] M. Lavitrano, M. L. Bacci, M. Forni, D. Lazzereschi, C. D. Stefano, D. Fioretti, P. Giancotti, G. Marfe, L. Pucci, L. Renzi, H. Wang, A. Stoppacciaro, G. Stassi, M. Sargiacomo, P. Sinibaldi, V. Turchi, R. Giovannoni, G. D. Casa, E. Seren, and G. Rossi, "Efficient production by sperm-mediated gene transfer of human decay accelerating factor (hDAF) transgenic pigs for xenotransplantation," *Proceedings of the National Academy of Sciences*, vol. 99, no. 22, pp. 14 230–14 235, October 2002.

[69] L.-M. Houdebine, "The methods to generate transgenic animals and to control transgene expression," *Journal of Biotechnology*, vol. 98, no. 2-3, pp. 145–160, September 2002.

[70] M. Hirabayashi and S. Hochi, *Rat Genomics*, ser. Methods in Molecular Biology. Humana Press, 2010, vol. 597, ch. 9: Generation of Transgenic Rats by Ooplasmic Injection of Sperm Cells Exposed to Exogenous DNA, pp. 127–136.

[71] M. Hirabayashi, M. Kato, K. Amemiya, and S. Hochi, "Direct comparison between ICSI-mediated DNA transfer and pronuclear DNA microinjection for producing transgenic rats," *Experimental Animals*, vol. 57, no. 2, pp. 145–148, April 2008.

[72] E. Neumann, M. Schaefer-Ridder, Y. Wang, and P. H. Hofschneider, "Gene transfer into mouse lyoma cells by electroporation in high electric fields," *The EMBO Journal*, vol. 1, no. 7, p. 841, July 1982.

[73] M. Teifel, L. Heine, S. Milbredt, and P. Friedl, "Optimization of transfection of human endothelial cells," *Endothelium*, vol. 5, no. 1, pp. 21–35, February 1997.

[74] T. Inoue, K. Correia, and R. Krumlauf, *Cell Biology: A Laboratory Handbook*, thrid ed. Elsevier Academic, 2006, vol. 4, ch. 6: Electroporation of Living Embryoes, pp. 35–42.

[75] C. A. Schmotzer, M. E. Dunlap-Brown, S. P. Butler, W. H. Velander, and F. C. Gwazdauskas, "Development of murine embryos following electroporation," *Journal of Assisted Reproduction and Genetics*, vol. 20, no. 4, pp. 148–152, April 2003.

[76] J. Grabarek, B. Plusa, D. Glover, and M. Zernicka-Goetz, "Efficient delivery of dsRNA into zona-enclosed mouse oocytes and preimplantation embryos by electroporation," *Genesis*, vol. 32, no. 4, pp. 269–276, 2002.

[77] M. Waksmundzka and P. Debey, "Electric field-mediated BrUTP uptake by mouse oocytes, eggs, and embryos," *Molecular Reproduction and Development*, vol. 58, no. 2, pp. 173–179, 2001.

[78] A. B. Aeurbach, "Alternative methods to pronuclear microinjections for random transgene integration in mouse," *Transgenics*, vol. 4, no. 3, pp. 169–187, 2005.

[79] A.-K. Hadjantonakis, S. Macmaster, and A. Nagy, "Embryonic stem cells and mice expressing different GFP variants for multiple non-invasive reporter usage within a single animal," *BMC Biotechnology*, vol. 2, no. 1, pp. 11–19, June 2002.

[80] K. Vintersten, C. Monetti, M. Gertsenstein, P. Zhang, L. Laszlo, S. Biechele, and A. Nagy, "Mouse in red: Red fluorescent protein expression in mouse ES cells, embryos, and adult animals," *Genesis*, vol. 40, no. 4, pp. 241–246, December 2004.

[81] J. Z. Long, C. S. Lackan, and A.-K. Hadjantonakis, "Genetic and spectrally distinct in vivo imaging: embryonic stem cells and mice with widespread expression of a monomeric red fluorescent protein," *BMC Biotechnology*, vol. 5, no. 20, pp. 20–31, July 2005.

[82] S. Johnston, P. Anziano, K. Shark, J. Sanford, and R. Butow, "Mitochondrial transformation in yeast by bombardment with microprojectiles," *Science*, vol. 240, no. 4858, pp. 1538–1541, June 1988.

[83] D. Cai, J. Mataraza, Z. Qin, Z. Huang, J. Huang, T. Chiles, D. Carnahan, K. Kempa, and Z. Ren, "Highly efficient molecular delivery into mammalian cells using carbon nanotube spearing," *Nature Methods*, vol. 2, no. 6, pp. 449–454, June 2005.

[84] C. Hara, K. Tateyama, N. Akamatsu, H. Imabayashi, K. Karaki, N. Nomura, H. Okano, and A. Miyawaki, "A practical device for pinpoint delivery of molecules into multiple neurons in culture," *Brain Cell Biology*, vol. 35, no. 4–6, pp. 229–237, December 2006.

[85] X. Chen, A. Kis, A. Zettl, and C. R. Bertozzi, "A cell nanoinjector based on carbon nanotubes," *Proceedings of the National Academy of Sciences*, vol. 104, no. 20, pp. 8218–8222, May 2007.

[86] R. A. David and B. D. Jensen, "Modeling DNA motion under electrostatic repulsion within a living cell," in *Proceedings of ASME 2009 International Design Engineering Technical Conferences & Computers and Information in Engineering Conference*. ASME, August 2009.

[87] R. A. David, "Modeling and testing of DNA motion for nanoinjection," Ph.D. dissertation, Brigham Young University, 2011.

[88] A. Delgadoa, F. Gonzalez-Caballeroa, R. Hunterb, L. Koopalc, and J. Lyklema, "Measurement and interpretation of electrokinetic phenomena," *Journal of Colloid and Interface Science*, vol. 309, no. 2, pp. 194–224, May 2007.

[89] R. A. David, J. L. Black, B. D. Jensen, and S. H. Burnett, "Modeling and experimental validation of DNA motion during electroporesis," in *Proceedings of ASME 2010 International Design Engineering Technical Conferences & Computers and Information in Engineering Conference*, 2010.

[90] A. S. Goldstein, J. Huang, C. Guo, I. P. Garraway, and O. N. Witte, "Identification of a cell of origin for human prostate cancer," *Science*, vol. 329, no. 5991, pp. 568–571, July 2010.

[91] S. O. Ryan, A. M. Vlad, K. Islam, J. Gariépy, and O. J. Finn, "Tumor-associated MUC1 glycopeptide epitopes are not subject to self-tolerance and improve responses to MUC1 peptide epitopes in MUC1 transgenic mice," *Biological Chemistry*, vol. 390, no. 7, pp. 611–618, July 2009.

[92] D. A. Gimbel, H. B. Nygaard, E. E. Coffey, E. C. Gunther, J. Laurén, Z. A. Gimbel, and S. M. Strittmatter, "Memory impairment in transgenic alzheimer mice requires cellular prion protein," *The Journal of Neuroscience*, vol. 30, no. 18, pp. 6374 – 6367, May 2010.

[93] J. F. Aitken, K. M. Loomes, D. W. Scott, S. Reddy, A. R. Phillips, G. Prijic, C. Fernando, S. Zhang, R. Broadhurst, P. L'Huillier, and G. J. Cooper, "Tetracycline treatment retards the onset and slows the progression of diabetes in human amylin/islet amyloid polypeptide transgenic mice," *Diabetes*, vol. 59, no. 1, pp. 161–171, January 2010.

[94] X. Zheng, H. K. Surks, and X. Zhang, "A versatile cell contractility mapping transducer utilizing moiré-based technique," *Journal of Microelectromechanical Systems*, vol. 19, no. 4, pp. 764–773, August 2010.

[95] F. Caselli, P. Bisegna, and F. Maceri, "EIT-inspired microfluidic cytometer for single-cell dielectric spectroscopy," *Journal of Microelectromechanical Systems*, vol. 19, no. 5, pp. 1029–1040, October 2010.

[96] N. Inomata, T. Mizunuma, Y. Yamanishi, and F. Arai, "Omnidirectional actuation of magnetically driven microtool for cutting of oocyte in a chip," *Journal of Microelectromechanical Systems*, vol. 20, no. 2, pp. 383–388, April 2011.

[97] J. Subirana and M. Soler-Lopez, "Cations as hydrogen bond donors: A view of electrostatic interactions in DNA," *Annual Review of Biophysics and Biomolecular Structure*, vol. 32, no. 1, pp. 27–45, 2003.

[98] Q. T. Aten, B. D. Jensen, S. H. Burnett, and L. L. Howell, "Electrostatic accumulation and release of DNA using a micromachined lance," *Journal of Microelectromechanical Systems*, In Review 2011.

[99] D. Gan, J. Dai, and Q. Liao, "Constraint analysis on mobility change of a novel metamorphic parallel mechanism," *Mechanism and Machine Theory*, vol. 45, no. 12, p. 1864–1876, December 2010.

[100] L. Zhang and J. S. Dai, "Reconfiguration of spatial metamorphic mechanisms," *Journal of Mechanisms and Robotics*, vol. 1, no. 1, pp. 011 012.1–011 012.8, 2009.

[101] L. Zhang, J. S. Dai, and T.-L. Yang, "Reconfiguration techniques and geometric constraints of metamorphic mechanisms," in *2009 Proceedings of the ASME International Design Engineering Technical Conferences and Computers and Information in Engineering Conference, DETC2009*, vol. 7, 2009, pp. 559–575.

[102] S. Park, Y.-S. Kim, W. B. Kim, and S. Jon, "Carbon nanosyringe array as a platform for intracellular delivery," *Nano Letters*, vol. 9, no. 4, pp. 1325–1329, 2009.

[103] A. K. Shaleka, J. T. Robinsona, E. S. Karpa, J. S. Leea, D.-R. Ahnb, M.-H. Yoona, A. Suttona, M. J. amd Rona S. Gertnera, T. S. Gujrala, G. MacBeatha, E. G. Yanga, and H. Parka, "Vertical silicon nanowires as a universal platform for delivering biomolecules into living cells," *Proceedings of the National Academy of Sciences*, vol. 5, no. 5, pp. 1870–1875, February 2010.

[104] C. M. Cuerrier, R. Lebel, and M. Grandbois, "Single cell transfection using plasmid decorated AFM probes," *Biochemical and Biophysical Research Communications*, vol. 355, no. 3, pp. 632–636, April 2007.

[105] R. Yeh, E. J. Kruglick, and K. S. Pister, "Surface-micromachined components for articulated microrobots," *Journal of Microelectromechanical Systems*, vol. 5, no. 1, pp. 10–17, March 1996.

[106] A. Friedberger and R. S. Muller, "Improved surface-micromachined hinges for fold-out structures," *Journal of Microelectromechanical Systems*, vol. 7, no. 3, pp. 315–319, September 1998.

[107] B. L. Boyce, J. M. Grazier, T. E. Buchheit, and M. J. Shaw, "Strength distributions in polycrystalline silicon MEMS," *Journal of Microelectromechanical Systems*, vol. 16, no. 2, pp. 179–190, April 2007.

[108] S. Oak, G. F. Edmiston, G. Sivakumar, and T. Dallas, "Rotating out-of-plane micromirror," *Journal of Microelectromechanical Systems*, vol. 19, no. 3, pp. 632 – 639, June 2010.

[109] L. D. Brown, T. T. Cai, and A. DasGupta, "Interval estimation for a binomial proportion," *Statistical Science*, vol. 16, no. 2, pp. 101–133, 2001.

[110] J. W. Gordon and F. H. Ruddle, "Integration and stable germ line transmission of genes injected into mouse pronuclei," *Science*, vol. 214, no. 4526, pp. 1244–1246, December 1981.

[111] O. Kirak, E.-M. Frickel, G. M. Grotenbreg, H. Suh, R. Jaenisch, and H. L. Ploegh, "Transnuclear mice with predefined t cell receptor specificities against toxoplasma gondii obtained via scnt," *Science*, vol. 328, no. 5975, pp. 243–248, April 2010.

[112] A. Gossler, T. Doetschman, R. Korn, E. Serfling, and R. Kemler, "Transgenesis by means of blastocyst-derived embryonic stem cell lines," *Proceedings of the National Academy of Sciences*, vol. 83, no. 23, pp. 9065–9069, December 1986.

[113] C. Lois, E. J. Hong, S. Pease, E. J. Brown, and D. Baltimore, "Germline transmission and tissue-specific expression of transgenes delivered by lentiviral vectors," *Science*, vol. 295, no. 5556, pp. 868–872, February 2002.

[114] R. A. David, B. D. Jensen, J. L. Black, S. H. Burnett, and L. L. Howell, "Modeling and experimental validation of DNA motion in uniform and non-uniform DC electric fields," *Journal of Nanotechnology in Engineering and Medicine*, vol. 1, p. 04007, 2010.

[115] R. Audubert and S. d. Mende, *The principles of electrophoresis*. Macmillan, 1960.

[116] B. Everitt, *The Analysis of Contingency Tables*. Chapman & Hall, 1992.

[117] G. J. G. Upton, "Fisher's exact test," *Journal of the Royal Statistical Society. Series A*, vol. 155, no. 3, pp. 395–402, 1992.

[118] M. H. Dado, "Variable parametric pseudo-rigid-body model for large-deflection beams with end loads," *International Journal of Non-Linear Mechanics*, vol. 36, no. 7, pp. 1123–1133, October 2001.

[119] X. Pei, J. Yu, G. Zonga, and S. Bia, "An effective pseudo-rigid-body method for beam-based compliant mechanisms," *Precision Engineering*, vol. 34, no. 3, pp. 634–639, July In Press.

[120] P. S. Sreetharan and R. J. Wood, "Passive aerodynamic drag balancing in a flapping-wing robotic insect," *Journal of Mechanical Design*, vol. 132, no. 5, pp. 0 510 061–01 100 611, May 2010.

[121] G. A. Kragten and G. A. Kragten1, "A platform for grasp performance assessment in compliant or underactuated hands," *Journal of Mechanical Design*, vol. 132, no. 2, pp. 0 245 021–0 245 026, February 2010.

[122] Y. Tian, B. Shirinzadeh, and D. Zhang, "Design and dynamics of a 3-dof flexure-based parallel mechanism for micro/nano manipulation," *Microelectronic Engineering*, vol. 87, no. 2, pp. 230–241, February 2010.

[123] T.-L. Wu, J.-H. Chen, and S.-H. Chang, "A six-DOF prismatic-spherical-spherical parallel compliant nanopositioner," *Ultrasonics, Ferroelectrics and Frequency Control, IEEE Transactions on*, vol. 55, no. 12, pp. 2544–2551, December 2008.

[124] H.-J. Su and J. M. McCarthy, "A polynomial homotopy formulation of the inverse static analysis of planar compliant mechanisms," *Journal of Mechanical Design, Transactions of the ASME*, vol. 128, no. 4, pp. 776 – 786, July 2006.

[125] S. Desrochers, D. Pasini, and J. Angeles, "Optimum design of a compliant uniaxial accelerometer," *Journal of Mechanical Design*, vol. 132, no. 4, pp. 0 410 111–0 410 118, April 2010.

[126] D. L. Blanding, *Exact Constraint: Machine Design Using Kimematic Principles*. New York, NY: ASME Press, 1999.

[127] H.-J. Su, "A pseudorigid-body 3r model for determining large deflection of cantilever beams subject to tip loads," *Journal of Mechanisms and Robotics*, vol. 1, no. 2, pp. 1–9, May 2009.

[128] N. D. Masters and L. L. Howell, "A three degree-of-freedom model for self-retracting fully compliant bistable micromechanisms," *Journal of Mechanical Design, Transactions of the ASME*, vol. 127, no. 4, pp. 739–744, August 2005.

[129] Y. S. Oh and S. Kota, "Synthesis of multistable equilibrium compliant mechanisms using combinations of bistable mechanisms," *Journal of Mechanical Design*, vol. 131, no. 2, p. 021002, February 2009.

[130] G. Chen, D. L. Wilcox, and L. L. Howell, "Fully compliant double tensural tristable micromechanisms (DTTM)," *Journal of Micromechanics and Microengineering*, vol. 19, no. 2, p. 025011 (8pp), February 2009.

[131] N. F. Wang and K. Tai, "Design of 2-DOF compliant mechanisms to form grip-and-move manipulators for 2D workspace," *Journal of Mechanical Design*, vol. 123, no. 3, pp. 0 310 071–0 310 079, March 2010.

[132] P. M. Pardalos, D. Shalloway, and G. Xue, "Optimization methods for computing global minima of nonconvex potential energy functions," *Journal of Global Optimization*, vol. 4, no. 2, pp. 117–133, March 1994.

[133] C. Lavor and N. Maculan, "A function to test methods applied to global minimization of potential energy of molecules," *Numerical Algorithms*, vol. 35, no. 2-4, p. 287–300, April 2004.

[134] N. P. Moloi and M. M. Ali, "An iterative global optimization algorithm for potential energy minimization," *Computational Optimization and Applications*, vol. 30, no. 2, pp. 119–132, February 2005.

[135] B. L. Weight, C. A. Mattson, S. P. Magleby, and L. L. Howell, "Configuration selection, modeling, and preliminary testing in support of constant force electrical connectors," *Journal of Electronic Packaging, Trans. ASME*, vol. 129, no. 3, pp. 236–246, 2007.

[136] W. D. van Dorsser, R. Barents, B. M. Wisse, M. Schenk, and J. L. Herder, "Energy-free adjustment of gravity equilibrators by adjusting the spring stiffness," *Proceedings of the Institution of Mechanical Engineers, Part C: Journal of Mechanical Engineering Science*, vol. 222, no. 9, pp. 1839–1846, 2008.

[137] R. Saravanan, S. Ramabalan, and P. D. Babu, "Optimum static balancing of an industrial robot mechanism," *Engineering Applications of Artificial Intelligence*, vol. 21, no. 6, pp. 824–834, September 2008.

[138] J. O. Jacobsen, B. G. Winder, L. L. Howell, and S. P. Magleby, "Lamina emergent mechanisms and their basic elements," *Journal of Mechanisms and Robotics*, vol. 2, no. 1, p. 011003, February 2010.

[139] J. O. Jacobsen, G. Chen, L. L. Howell, and S. P. Magleby, "Lamina emergent torsional (LET) joint," *Mechanism and Machine Theory*, vol. 44, no. 11, pp. 2098 – 2109, November 2009.

[140] G. Chen, Q. T. Aten, S. Zirbel, B. D. Jensen, and L. L. Howell, "A tristable mechanism configuration employing orthogonal compliant mechanisms," *Journal of Mechanisms and Robotics*, vol. 2, no. 1, pp. 1–6, February 2010.

[141] B. B. Cherry, L. L. Howell, and B. D. Jensen, "Evaluating three-dimensional effects on the behavior of compliant bistable micromechanisms," *Journal of Micromechanics Microengineering*, vol. 18, no. 095001, p. 095001, July 2008.

[142] A. Reddy, H. Kahn, and A. H. Heuer, "A MEMS-based evaluation of the mechanical properties of metallic thin films," *Journal of Microelectromechanical Systems*, vol. 16, no. 3, pp. 650–658, June 2007.

[143] H. Cho, J.-L. Ding, A. Bandyopadhyay, and S. Bose, "Finite element analysis of piezoelectric thin film membrane structures," *Ultrasonics, Ferroelectrics and Frequency Control, IEEE Transactions on*, vol. 54, no. 10, pp. 2036–2044, October 2007.

[144] K.-S. Chen, K.-S. Ou, and L.-M. Li, "Development and accuracy assessment of simplified electromechanical coupling solvers for MEMS applications," *Journal of Micromechanics Microengineering*, vol. 14, no. 2, pp. 159–169, 2004.

[145] R. Ansola, J. C. Estrella Veguería, and J. A. Tárrago, "A simple evolutionary topology optimization procedure for compliant mechanism design," *Finite Elements in Analysis and Design*, vol. 44, no. 1-2, pp. 53–62, December 2007.

[146] W. M. Rubioa, S. Nishiwakib, and E. C. N. Silvac, "Design of compliant mechanisms considering thermal effect compensation and topology optimization," *Finite Elements in Analysis and Design*, vol. 46, no. 12, pp. 1049–1060, December 2010.

[147] D. G. Smith, Q. T. Aten, B. D. Jensen, and L. L. Howell, "Piezoresistive encoders for ratcheting actuation systems," *Sensors and Actuators: A. Physical*, vol. 165, no. 2, pp. 173–180, February 2010.

[148] D. Biniona and X. Chen, "Coupled electrothermal mechanical analysis for MEMS via model order reduction," *Finite Elements in Analysis and Design*, vol. 46, no. 12, pp. 1068–1076, December 2010.

[149] Q. T. Aten, S. A. Zirbel, B. D. Jensen, and L. L. Howell, "A numerical method for position analysis of compliant mechanisms with more degrees of freedom than inputs," in *ASME 2010 International Design Engineering Technical Conferences & Computers and Information in Engineering Conference*, 2010, pp. 2010–28 474.

[150] G. Zhu, L. Saydy, M. Hosseini, J.-F. Chianetta, and Y.-A. Peter, "A robustness approach for handling modeling errors in parallel-plate electrostatic MEMS control," *Journal of Microelectromechanical Systems*, vol. 17, no. 6, pp. 1302–1314, December 2008.

[151] A. M. Elshurafa and E. I. El-Masry, "Finite-element modeling of low-stress suspension structures and applications in RF MEMS parallel-plate variable capacitors," *Microwave Theory and Techniques, IEEE Transactions on*, vol. 54, no. 5, pp. 211–2219, May 2006.

[152] K.-J. Bathe, *Finite Element Procedures*. New Jersey: Prentice Hall, 1996.

[153] T. Tsong, "Electroporation of cell membranes," *Biophysical Journal*, vol. 60, no. 2, pp. 297–306, August 1991.

[154] H. Nakamura, *Electroporation and Sonoporation in Developmental Biology*, ser. 4431094261. Springer Verlag, 2009.

[155] M. Murakami, M. Fahrudin, M. Varisanga, and T. Suzuki, "Fluorescence expression by bovine embryos after pronuclear microinjection with the EGFP gene," *Journal of Veterinary Medical Science*, vol. 61, no. 7, pp. 843–847, July 1999.

[156] R. A. David, B. D. Jesen, J. L. Black, S. H. Burnett, and L. L. Howell, "Effects of dissimilar electrode materials and electrode position on DNA motion during electrophoresis," *Journal of Nanotechnology in Engineering and Medicine*, Accepted for Publication 2011.

[157] R. Helling, H. Goodman, and H. Boyer, "Analysis of endonuclease REco RI fragments of DNA from lambdoid bacteriophages and other viruses by agarose-gel electrophoresis," *Journal of Virology*, vol. 14, no. 5, pp. 1235–1244, November 1974.

[158] T. Maniatis, A. Jeffrey, and H. Van deSande, "Chain length determination of small double- and single-stranded DNA molecules by polyacrylamide gel electrophoresis," *Biochemistry*, vol. 14, no. 17, pp. 3787–3794, 1975.

[159] M. L. Soares, S. Haraguchi, M.E. Torres-Padilla, T. Kalmar, L. Carpenter, G. Bell, A. Morrison, C. J. Ring, N. J. Clarke, D. M. Glover, and M. Zernicka-Goetz, "Functional studies of signaling pathways in peri-implantation development of the mouse embryo by RNAi," *BMC Developmental Biology*, vol. 5, no. 1, p. 28, 2005.

[160] T. Matsuda and C. L. Cepko, "Electroporation and RNA interference in the rodent retina in vivo and in vitro," *Proceedings of the National Academy of Sciences of the United States of America*, vol. 101, no. 1, pp. 16–22, January 2004.

APPENDIX A. PRONUCLEAR NANOINJECTION: MATERIALS AND METHODS, AND DETAILED EXPERIMENTAL RESULTS

This chapter provides detailed information on the materials and methods employed in the pronuclear nanoinjection experiments described in Chapter 3. This chapter also gives expanded data on viability, integration and expression results from the nanoinjector experiments.

A.1 Materials and Methods

A.1.1 Polycrystalline Silicon Multi-User MEMS Processes (polyMUMPs)

The nanoinjector devices were fabricated using MEMSCAPs (www.memscap.com) Polycrystalline Silicon Multi-User MEMS Processes (polyMUMPs). This micromachining process begins with a single crystal silicon wafer, referred to as the substrate. The device (top) side of the substrate is coated with an insulating layer of silicon nitride. A stationary layer of polycrystalline silicon (POLY0) can be deposited over the silicon nitride.

The stationary and movable structural elements are fabricated from two layers of polycrystalline silicon, as shown in Figure A.1. The first and second polycrystalline silicon layers (POLY1 and POLY2) are 2 μm and 1.5 μm thick, respectively. A 500 nm thick gold layer can be placed over POLY2 to improve electrical conductivity, and reduce contact resistance. Selective regions of POLY1 and POLY2 geometry can be free to move with respect to each other, can be bonded to each other, or be bonded to the substrates surface as shown in Figure A.1. A complete description of polyMUMPs fabrication, design limitations, and design rules can be found in [4].

A.1.2 Nanoinjector Release and Packaging Protocol

When shipped from MEMSCAP, the nanoinjector is encased in layers of phosphosilicate glass (PSG) and photoreactive polymer (photoresist). These layers must be removed, through a

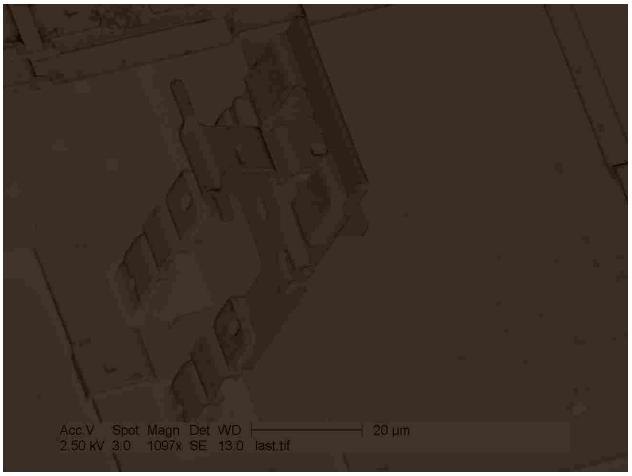

Figure A.1: This image shows the two polycrystalline layers (POLY1 and POLY2) of the polyMUMPs process in an out-of-plane link in the nanoinjector. Note how the first and second layers can be bonded together or can be free to move with respect to one another.

process called release, to allow the nanoinjector to move. The release process consists of chemical baths and rinses in the following order: acetone for 25 minutes to remove the photoresist, isopropyl alcohol for 2 minutes, deionized water for 2 minutes, 48% hydrofluoric acid for 2.5 minutes to remove the PSG, and deionized water for 10 minutes.

The nanoinjector is adhered to the inside of a shallow 35 mm cell-culture Petri dish (or the lid of a standard depth 35 mm cell-culture Petri dish) with double sided adhesive film. The packaged nanoinjector is stored in deionized water prior to use to reduce adhesion with the substrate.

A.1.3 Transgene Preparation

The plasmid pCAG-GFP (Addgene plasmid 11150) [160] was digested using HindIII, ApaL1, and Spe1 and the resulting 3018 bp transgene was isolated using low melting temperature agarose gel electrophoresis and purified with Qiagen QIAEX II kit. For RFP studies, the EGFP was removed from the pCAG-GFP plasmid and replaced with RFPmonomer from pDSRedmonomerN1 (ClonTech plasmid 632465). The same restriction endonucleases for digestion of the pCAG-GFP plasmid were used for the CAG-RFP transgene with a resulting product of 2976 bp. Transgene extracted from agarose was quantified by spectrophotometry and prepared in a PBS solution at 10-15 ng/l for nanoinjection. For microinjection, the transgene was diluted to a con-

centration of 3 ng/μl in low (0.1M) EDTA TE (pH 7.4) on days 1 and 2, and was diluted to a concentration of 2 ng/l on days 3 and 4.

A.1.4 Nanoinjection in-vitro Studies at Brigham Young University

CD1 outbred mice were purchased from Charles River Laboratories (Boston, MA) and maintained in the BYU College of Life Sciences Specific Pathogen Free Facility in accordance with guidelines of the Animal Welfare Act and under approval of the resident IACUC. CD1 females were treated with 5 units pregnant mare serum gonadotropin (PMS) (EMD Chemicals Cat #367222) at 3 hrs prior to the dark cycle, then two days later treated with 5 units human chorionic gonadotropin (hCG) (EMD Chemicals, cat #869031) at 5 hours prior to the dark cycle and set with a fertile CD1 male for breeding. Donor embryos were obtained the following morning (18 hours after hCG injection) from females with a vaginal plug by dissection of cumulus mass from the oviducts. Zygotes were obtained after 2 minutes of suspension of the mass in PBS with 10 mg/ml Polyvinylpyrrolidone and 330 units/ml hyaluronidase (Worthington Biochemicals, Lakewood, NJ). Zygotes were rinsed in M2 medium (Millipore,Billerica, MA), then rinsed in PBS, then maintained in a drop of KSOM medium (Millipore) under silicone oil (Sigma Cat #85414) in an incubator at 37$\circ$ C and 5% CO2.

Nanoinjection was performed in PBS at room temperature. Each batch of zygotes remained on the MEMS chip for no more than 30 minutes. DNA in a holding pipette was dispensed over the nanoinjection lance using a syringe pump and attraction of DNA proceeded at 1.5 (+) volts for 30 seconds up to 5 minutes. Upon injection, DNA was released for 10 seconds at 1.5 (-) volts, then the lance was withdrawn from the zygote. Injected zygotes were returned to KSOM medium under oil and incubated at 37$\circ$ C and 5% CO2. Embryos were observed by microscopy for survival and two-cell stage development (see Table A.1).

A.1.5 Side-by-side Nanoinjection and Microinjection in-vivo Study at the University of Utah Transgenic and Gene Targeting Mouse Core

Embryos were harvested at 0.5 days post-coitus from crosses of male and female C57Bl/6J x CBA/J F1 mice. Female F1 mice were superovulated by IP injection of 5 IU of PMS (pregnant

mare serum gonadotropin) (NHPP, Torrance, CA) at 2 pm followed by IP injection of 5 IU of hCG (human chorionic gonadotropin) (Sigma cat #CG-10) 47 hours later, at which time females were mated to F1 males.

Zygotes were dissected from the oviducts of females with a vaginal plug 18 hours after hCG injection into M2 medium (Sigma cat #M7167). Cumulus masses containing embryos were placed into a 500 μl bath of M2 medium containing 40 μl of 10 mg/ml stock of hyaluronidase (Sigma cat #H3884) for 3 to 4 minutes to remove cumulus cells from the embryos. Zygotes were washed through 100 μl drops of M2 medium and stored in 50 μl drops of M16 medium (Sigma cat #M7292) under mineral oil (Sigma cat #M8410) in a 5% CO2 37$\circ$ incubator until ready to use. Zygotes with obvious pronuclei were chosen for injection. 10-20 zygotes at a time were removed from the incubator drop for injection at room temperature using either nanoinjection or microinjection as described below.

For Nanoinjection: Zygotes were transferred to PBS on the MEMS chip. DNA in a holding pipette was dispensed over the nanoinjection lance using a syringe pump and attraction of DNA proceeded at 1.5 (+) volts for 30 seconds up to 90 seconds. Upon injection, DNA was released for 10 seconds at 1.5 (-) volts, then the lance was withdrawn from the zygote.

For Microinjection controls: Zygotes were transferred to M2 under oil on a slide. DNA was microinjected using an Eppendorf Femtojet or an Eppendorf CellTram microinjection system until there was obvious slight swelling of the pronucleus. The injected volume was approximately 2 picoliters/embryo.

Nanoinjected and microinjected zygotes were incubated overnight in a 50 μl drop of M16 medium under oil in a 5% CO2 37$\circ$ incubator. Embryos that developed to two-cell stage were rinsed through three 100 μl drops of M2 medium and surgically implanted into the oviducts of 0.5 day pseudo-pregnant females. Approximately twenty two-cell embryos were implanted per mouse. Timed pseudo-pregnant females were obtained by mating C57Bl/6J x CBA/J F1 females to vasectomized C57Bl/6J x CBA/J F1 males and checking for vaginal plugs.

A.1.6 Genotypic and Phenotypic Testing

Tail biopsies were obtained for genotyping, and blood samples were taken for phenotyping. Genomic DNA was extracted from tail biopsy through overnight proteinase K digestion and iso-

propanol precipitation. DNA was then assayed for the transgene by PCR using the forward primer 5'-TGCCCGAAGGCTACGTCC-3' and reverse primer 5'-GCACGCTGCCGTCCTCG-3' which were designed based on the EGFP sequence and which yield a 267 bp product (see Figure A.2).

To ensure DNA quality, each DNA sample was also subjected to PCR using β-actin primers: the forward primer 5'-GTGGGCCGCTCTAGGCACCA-3' and reverse primer 5'-CGGTTGGCCT TAGGGTTCAGGG-3' yield a 244 bp product (see Figure A.2).

Blood samples from mice were diluted in PBS with 100 units/ml heparin prior to flow cytometry. Peritoneal exudates were obtained by injecting 5 ml of Hanks balanced salt solution (2-3 ml for smaller pups) into the peritoneal cavity. Thigh muscle, brain, and gut tissue samples were homogenized in 2 ml of Hanks, and passed through a 70 μm filter. All samples were stored on ice prior to flow cytometry. Flow cytometry analysis was performed with a BD Biosciences FACSCanto cytometer. Flow data was analyzed using Diva software (BD Biosciences) and Summit software (Dako-Cytomation). Example flow cytometry results are shown in Figure A.4.

A.1.7 EGFP PCR Product Sequencing

EGFP PCR products from two representative mice were purified using Amicon Ultra centrifugal filters according to the company protocol. The forward or reverse primers for GFP transgene given above were added and samples submitted to BYU DNA Sequencing Center for Big Dye amplification and sequencing reactions. Figure A.3 shows the consensus between the EGFP sequence and the sequences of the PCR products.

A.1.8 Statistical Analysis

The viability, birth, integration, and expression data were analyzed using statistical methods for binomial distributions. The estimates of the binomial proportion and the $(1-\alpha)$ confidence intervals for the binomial proportion were calculated using the Agresti–Coull interval given in [109]. These results are presented in Table A.2.

Given a confidence level of $(1-\alpha)$ and X successful events (births, expressing pups, etc) out of n attempts (injections performed, pups observed, etc) the Agresti–Coull interval midpoints

and bounds are calculated by

$$CI = \tilde{p} \pm (\tilde{p}\tilde{q})^{1/2}\tilde{n}^{-1/2} \tag{A.1}$$

where κ is found from the standard normal distribution $\Phi(z)$ by

$$\kappa = \Phi(1-\alpha) \tag{A.2}$$

The remaining variables used to calculate CI are

$$\tilde{X} = X + \kappa^2 \tag{A.3}$$

$$\tilde{n} = n + \kappa^2 \tag{A.4}$$

$$\tilde{p} = \tilde{X}/\tilde{n} \tag{A.5}$$

$$\tilde{q} = (1-\tilde{p}) \tag{A.6}$$

The differences between success rates for comparable groups, such as two-cell development rates for untreated and nanoinjected zygotes, were tested for statistical significance using the two-tailed Fishers exact test for 2×2 contingency tables [116], [117]. Odds ratios were computed to facilitate qualitative comparison between nanoinjection and the microinjection positive control [116]. Fishers test and the odds ratio were calculated using the JMP statistical software package (S.A.S Institute). Implementations of Fishers exact test and odds ratios are widely available, and the derivations are not presented here.

A.2 Expanded Nanoinjection Data

The following tables and images provide more detail on the results from the nanoinjection experiments presented graphically in Chapter 3. Table A.1 reports the proportion of untreated and pronuclear nanoinjected zygotes progressing to the two-cell stage during in-vitro only testing. Tables A.2 and A.3 give the detailed results of generating transgenic mouse pups via nanoinjection with microinjection as a positive control. Figure A.2 shows representative PCR results for the presence of EGFP and β-actin. Figure A.3 shows gene sequencing results on EGFP PCR

products obtained from nanoinjected and microinjected transgenic mouse pups. Figure A.4 shows representative EGFP expression in mouse blood obtained by flow cytometry.

Table A.1: Rates of 24-hour viability to two-cell stage for untreated and nanoinjected zygotes from in-vitro only studies.

	2-cell Stage / Zygotes Cultured
Nanoinjection	559/713 $(78.3 \pm 3.0\%)$
Untreated	299/363 $(82.0 \pm 3.9\%)$

Table A.2: Mouse pup data consisting of development to two-cell embryos, births, integration, and expression. Values given in parenthesis are the Agresti–Coull binomial confidence interval midpoint and bounds [109]. Statistical significance was determined with Fishers exact test for two tails [116], [117].

(**A**) Rates of 24-hour viability to two-cell stage, births, integration, and expression. Rates are based on the number of embryos or pups progressing from the previous step.

	2-cell Stage / Total Injected†	**Births / Transferred†***	**Integration / Pups**	**Expression / Pups**
Nanoinjection	288/371 $(77.3 \pm 4.2\%)$	151/288 $(52.4 \pm 5.7\%)$	23/140 $(17.3 \pm 6.2\%)$	13/140 $(10.4 \pm 5.0\%)$
Microinjection	188/360 $(52.2 \pm 5.1\%)$	81/339 $(24.2 \pm 4.5\%)$	10/81 $(14.1 \pm 7.4\%)$	6/81 $(9.3 \pm 6.2\%)$
Microinjection	163/282 $(57.7 \pm 5.7\%)$			
Untreated	26/31 $(80.1 \pm 13.3\%)$			

† Results are statistically significant between nanoinjected and microinjected groups with $(p < 0.001)$. * Eggs from the two microinjection technicians were grouped for transfer, and 12 microinjected 2-cell embryos were lost during the transfer procedure. During 2010 26.5% (1127/5250) of transferred embryos were born during other pronuclear microinjection studies at the same facility.

(B) Rates births, integration, and expression for nanoinjection and microinjection. All rates are based on the number of injections performed.

	Births / Total Embryos Injected*†	**Integration / Total Embryos Injected*†**	**Expression / Total Embryos Injected*+**
Nanoinjection	151/371 $(40.8 \pm 5.0\%)$	23/371 $(6.7 \pm 2.5\%)$	13/371 $(4.0 \pm 2.0\%)$
Microinjection	81/642 $(13.1 \pm 2.6\%)$	10/642 $(1.9 \pm 0.8\%)$	6/642 $(1.3 \pm 0.9\%)$

*12 microinjected 2-cell embryos lost during the transfer procedure were not included in *thisdataset*.†Results are statistically significant between nanoinjected and microinjected groups with $(p < 0.001)$. + Results are statistically significant between nanoinjected and microinjected groups with $(p < 0.01)$.

Table A.3: Viability and expression data from (A) nanoinjected and (B) microinjected zygotes separated by the day the nanoinjections and microinjections were performed. Note that integrated and expressing pups were produced by nanoinjection during each of the four experimental replicates.

(**A**) Viability and expression data for nanoinjected zygotes.

	Day 1	**Day 2**	**Day 3**	**Day 4**
Nanoinjected Zygotes	99	111	91	70
2-cell Embryos	87	75	74	52
Transferred Embryos	87	75	74	52
Total Pups Born	45	36	37	33*
Integrated Pups	2	13	4	4
Expressing Pups	1	7	1	4

* 11 of these 33 pups were abandoned by their mother shortly after birth. Integration and expression data were taken from the remaining 22 pups.

(**B**) Viability and expression data for microinjected zygotes .

	Day 1	**Day 2**	**Day 3**	**Day 4**
Microinjected Zygotes	205	167	132	138
2-cell Embryos	100	88	86	77
Transferred Embryos	88	88	86	77
Total Pups Born	19	26	20	16
Integrated Pups	1	6	2	1
Expressing Pups	1	3	2	0

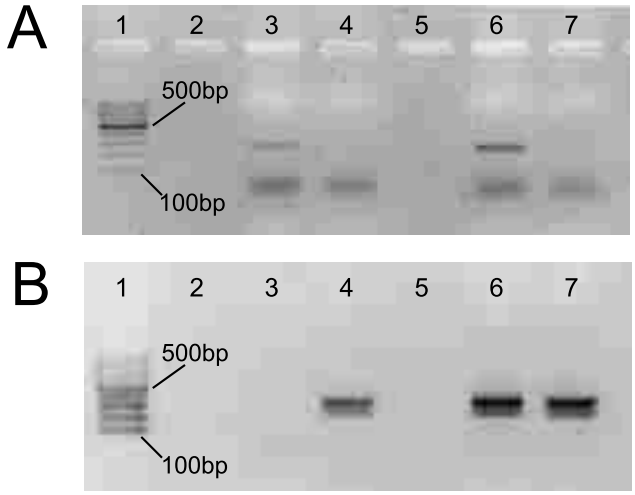

Figure A.2: Integration testing: gels containing PCR samples for genotyping mice. Transgene integration was determined by PCR of DNA samples from pups produced by nanoinjected and microinjected zygotes. (A) PCR of samples to detect GFP and (B) PCR of samples to detect β-actin to serve as a DNA control. Lanes on the images shown include (1) ladder, (2) blank, (3) EGFP plasmid as a GFP positive control and β-actin negative control, (4) wild type C57Bl/6J x CBA/J F1 as a GFP negative control and β-actin positive control, (5) blank, (6) GFP integration positive mouse, and (7) GFP integration negative mouse.

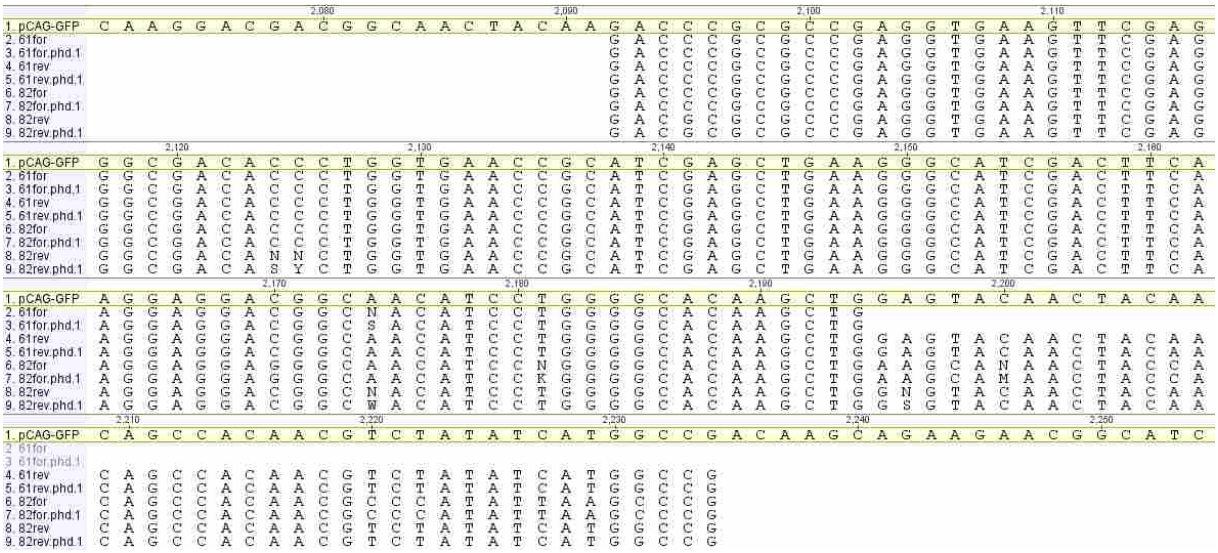

Figure A.3: Sequencing results verify PCR data obtained for integration testing. DNA sequencing was performed on positive samples from GFP amplification to verify that the resultant band was an amplification of the intended target sequence. Consensus occurred between the EGFP sequence (line 1) and the PCR products from a microinjected mouse (mouse 61, lines 2-5) and a nanoinjected mouse (mouse 82, lines 6-9)

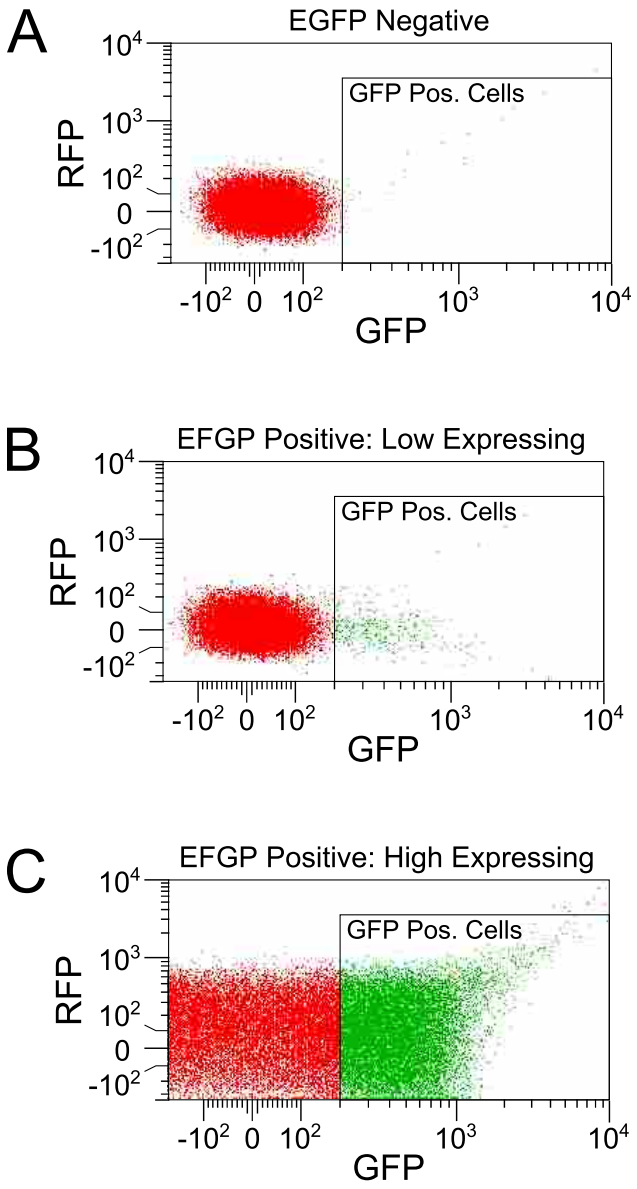

Figure A.4: Expression testing: Representative plots of flow cytometry data used to determine GFP expression in mouse pups. Blood samples were collected from mouse pups born from nanoinjected and microinjected zygotes. Each green point on a plot represents a GFP positive cell. (A) An example of flow cytometry results from a GFP negative mouse. (B) An example of data from a GFP positive mouse exhibiting low transgene expression. (C) An example of data from a GFP positive mouse exhibiting high transgene expression. A mouse was considered expression positive whether cells exhibited low or high GFP expression.

APPENDIX B. ANSYS SCRIPTS FOR SOLID AND SHELL ELEMENT ANALYSES

B.1 ANSYS Script for Shell Element Modeling of the Lamina Emergent Torsional Joint Presented in Chapter 5

The following ANSYS code performs a geometrically non-linear finite element analysis using ANSYS' geometry creation features, quadratic shell elements, loads incremented by substep, and a geometrically non-linear solution algorithm.

```
FINISH
/CLEAR,START
/FILNAME,PR1_shell_7,1

! using MEMS units sytem
! Force = uN
! Length = um
! Sress = MPa

/prep7
! define constants
pi = acos(-1)
t = 1.5
Lt = 100
Lb = 40
wt = 2.5
wb = 5
block_w = 15
block_h = 15
arm_gap = 10
arm_L = 100
hyp = lb-wt+block_h+arm_gap+arm_L-lb/2
theta = 30/180*pi
deltay = -hyp*(1-cos(theta))
deltaz = sin(theta)*hyp
STEPS = 10

! DEFINE SOME MATERIAL PROPERTIES
E = 165000
nu = .22
```

```
! define the geometry
k,1,0+block_w/2,0,0
k,2,lt+wb+block_w/2,0,0
k,3,lt+wb+block_w/2,lb,0
k,4,0+block_w/2,lb,0
k,5,0+block_w/2,wt,0
k,6,lt+block_w/2,wt,0
k,7,lt+block_w/2,lb-wt,0
k,8,0+block_w/2,lb-wt,0

l,1,2
l,2,3
l,3,4
l,5,6
l,6,7
l,7,8
l,1,5
l,4,8
al,all

l,3,7
l,2,6

! divide the area so it can be mapped meshed
ASBL,1,9
ASBL,3,10

! define the center connecting block
BLC4,0+block_w/2,lb-wt,-block_w/2,block_h
BLC4,0+block_w/2,wt,-block_w/2,-block_h
AGLUE,1,5
AGLUE,2,3

k,17,0,0,0
k,18,0,lb,0
l,1,17
l,4,18
ASBL,6,11
ASBL,5,12
/pnum,area,1
aplot

! define the element type and mesh options
et,1,shell93
keyopt,1,5,1
keyopt,1,8,2
```

```
r,1,t,t,t,t
mp,ex,1,E
mp,prxy,1,nu
mshape,0,2d
mshkey,1

et,2,beam4
r,2,block_w/2*t,block_w/2*t**3/12,(block_w/2)**3*t/12,t,block_w/2,0,,
mp,ex,2,E
mp,prxy,1,nu

! MESH THE AREAS
type,1
real,1
mat,1

lsel,s,line,,7,10
lesize,all,,,7
allsel,all

lsel,s,line,,1
lsel,a,line,,3,4,1
lsel,a,line,,6
lesize,all,,,140
allsel,all
amesh,1,2,1

lesize,2,,,56
amesh,4

mshkey,0
esize,block_w/25
amesh,3
amesh,6
amesh,7
amesh,8

! define the loading member

type,2
mat,2/CWD,'C:\Quentin\Project2a'
real,2
k,98,0,lb-wt+block_h+arm_gap,0
k,99,0,lb-wt+block_h+arm_gap+arm_L,0
l,98,99

lesize,14,,,1
```

```
lmesh,14
lsel,s,line,,14
nsll,s,1
*get,nodei,node,0,num,min
*get,nodej,node,0,num,max
allsel,all

lsel,s,line,,13
nsll,s,1
*get,curr_node,node,0,num,min
*get,num_node,node,0,count
E,nodei,curr_node

*do,nn,1,num_node-1,1
     *get,curr_node,node,curr_node,nxth
     E,nodei,curr_node
*enddo

allsel,all
/pnum,area,1
/pnum,line,1

/solu
! APPLY THE BOUNDARY CONDITIONS

dl,15,7,ux,0
dl,15,7,uy,0
dl,15,7,uz,0
dl,15,7,rotx,0
dl,15,7,roty,0
dl,15,7,rotz,0
dl,22,7,ux,0
dl,22,7,roty,0
dl,22,7,rotz,0
dl,21,3,ux,0
dl,21,3,roty,0
dl,21,3,rotz,0
dl,18,6,ux,0
dl,18,6,roty,0
dl,18,6,rotz,0
dl,23,8,ux,0
dl,23,8,roty,0
dl,23,8,rotz,0
dk,99,ux,0
dk,99,roty,0
dk,99,rotz,0
```

```
! apply the displacement load
dk,99,uy,deltay
dk,99,uz,deltaz

time,1.0
nsubst,steps,2*steps,steps
kbc,0
outres,all,1

nlgeom,on
allsel,all
solve

/post1
ksel,s,kp,,99
nslk,s
fsum
allsel,all

ksel,s,kp,,2
nslk,s
PRNSOL,ROT,COMP
allsel,all

PLESOL, S,EQV, 0,1.0
esla,s
nsla,s,1
allsel,all

/eof
```